

Spectroscopy of individual chlorosomes from *Chlorobaculum tepidum*

Von der Universität Bayreuth
zur Erlangung des Grades eines
Doktors der Naturwissenschaften (Dr. rer. nat.)
genehmigte Abhandlung

von

Lisa Maria Günther

aus Bayreuth

1. Gutachter: Prof Dr. Jürgen Köhler
2. Gutachter: Prof. Dr. Markus Lippitz

Tag der Einreichung: 26.03.2020

Tag des Kolloquiums: 06.05.2020

Abstract

Green sulfur bacteria survive under the lowest light conditions. They have perfectly adapted to this environment by evolving a unique light-harvesting apparatus, the chlorosome. This highly efficient antenna structure allows these bacteria to grow photosynthetically by absorbing only a few photons per bacteriochlorophyll molecule per day. The chlorosome is considered as a sack that accommodates hundreds of thousands bacteriochlorophyll (BChl) *c*, *d* or *e* molecules depending on the bacterial species and growth conditions. The BChls build supramolecular assemblies solely by self-assembly. This is in contrast to other photosynthetic light-harvesting antenna systems, for which a protein scaffold imposes the proper positioning of the chromophores. The electronically excited states of these molecular assemblies can be described as Frenkel excitons whose photophysical properties depend crucially on the mutual arrangement of the pigments.

The high light-harvesting efficiency of the chlorosomes and the self-assembly of the BChls into secondary structures within the chlorosome has promoted enormous interest in the structure-function relations of these molecular assemblies, as they can serve as blueprints for artificial light-harvesting systems. However, details about their structural organization of the supramolecular BChl arrangement in the chlorosomes are the subject of an ongoing debate, and conclusive structural information at atomic resolution is not available yet. Several models for their secondary structures, including tubular and lamellar aggregates, have been proposed to date. This variety reflects the sample heterogeneity inherent to this natural system.

The photophysical properties and their relation to the supramolecular organization of the chlorosome become accessible by optical spectroscopy. Therefore, in this thesis, spectroscopic techniques were used to study the structure-function relationship of the secondary structures in chlorosomes. However, the great heterogeneity of the samples leads to inhomogeneous broadening of the spectra, and subtle spectral features that might be characteristic for specific structural properties get obscured by ensemble averaging. In order to minimize the inherent sample heterogeneity polarization-resolved fluorescence-excitation spectroscopy was performed on individual chlorosomes from the photosynthetic green sulfur bacterium *Chlorobaculum (Cba.) tepidum*. This approach makes it possible to reveal the properties of the exciton states without ensemble averaging.

Furthermore, this technique was combined with mutagenesis. Hence, chlorosomes from the wild type and two mutants of *Cba. tepidum* were studied, in particular the *bchR*

single mutant and the *bchQR* double mutant. In these mutants, the various options for methylation of the bacteriochlorophyll molecules, which are a primary source of the structural and spectral heterogeneity of wild type chlorosome samples, are reduced via the deactivation of distinct genes.

The spectra of all studied chlorosomes show a strong intensity modulation as a function of the polarization of the incident radiation, which clearly indicates that collective excitations dominate the spectrum. A global analysis of the spectra revealed that the broad ensemble absorption band around 740nm consists of several spectral contributions. The observed photophysical properties of individual chlorosomes are consistent with cylindrical supramolecular structures.

Here, the information obtained from polarization-resolved fluorescence-excitation spectroscopy, cryo-electron microscopy, and theoretical modeling is combined with results previously obtained from nuclear magnetic resonance spectroscopy and cryo-electron microscopy. It is demonstrated that only the combination of these techniques yields an unambiguous description of the molecular packing of bacteriochlorophylls in chlorosomes. The results of these techniques show that in contrast to some suggestions in the literature, for the chlorosomes from the wild type as well as for those from mutants, the dominant secondary structural element features tubular symmetry. Moreover, the secondary structures of all three species follow a very similar construction principle, which is rolling up the lattice structure reported in [1] under an angle δ onto a cylinder.

The experimental results are compared with predictions from computer simulations of the cylindrical model structure. Studying variations of the structural parameters yields an explanation about the inhomogeneously broadened absorption bands. Moreover, the simulations provide a quantitative estimate of the curvature variation of these aggregates that might explain the ongoing debates concerning the chlorosome structure. From the correlation of spectral parameters, speculations about the degree of variation of the structural elements are made, and the composition of individual chlorosomes is deduced. Finally, a combination of all the results gives a conclusive picture of the interior of the chlorosomes.

Zusammenfassung

Grüne Schwefelbakterien wachsen zum Teil in extrem lichtarmen Lebensräumen. Sie haben sich perfekt an diese Umgebung angepasst, indem sie einen einzigartigen Apparat zum Sammeln von Licht entwickelt haben, das Chlorosom. Diese hocheffiziente Antennenstruktur ermöglicht diesen Bakterien eine photosynthetische Lebensweise, obwohl ihnen nur wenige Photonen pro Bakteriochlorophyllmolekül und Tag zur Verfügung stehen. Das Chlorosom ist eine sack-ähnliche Struktur und beinhaltet je nach Bakterienart und Wachstumsbedingungen hunderttausende von Bakteriochlorophyll (BChl) *c*-, *d*- oder *e*-Molekülen. Die BChl bilden innerhalb des Chlorosoms supramolekulare Strukturen durch Selbstaggregation. Diese Eigenschaft unterscheidet sie von anderen Lichtsammelkomplexen, die ein Proteingerüst zur richtigen Positionierung der Chromophore nutzen. Die elektronisch angeregten Zustände der molekularen Aggregate in Chlorosomen lassen sich als Frenkel-Exzitonen beschreiben, deren photophysikalische Eigenschaften entscheidend von der gegenseitigen Anordnung der Pigmente abhängen.

Die hohe Lichtsammeleffizienz der Chlorosome und die Selbstorganisation der BChl zu sekundären Strukturen innerhalb des Chlorosoms hat ein enormes Interesse an der Struktur-Funktion-Beziehung dieser molekularen Aggregate erregt, da sie als Blaupausen für künstliche Lichtsammelsysteme dienen können. Es gibt jedoch eine laufende Diskussion über die Einzelheiten der strukturellen Organisation der supramolekularen BChl-Anordnung in den Chlorosomen und bisher sind keine schlüssigen Strukturinformationen in atomarer Auflösung verfügbar. In mehreren Arbeiten wurden verschiedene Modelle für die sekundäre Struktur vorgeschlagen, unter anderem Modellstrukturen von Aggregaten mit einer Anordnung der BChl in Röhren und Lamellen. Die Vielfalt der Modelle spiegelt die diesem natürlichen System innewohnende Heterogenität der Proben wider.

Die photophysikalischen Eigenschaften und ihr Zusammenhang mit der supramolekularen Organisation des Chlorosoms werden durch optische Spektroskopie zugänglich. Daher wurden in dieser Arbeit spektroskopische Techniken benutzt, um die Struktur-Funktion-Beziehung der sekundären Strukturen in den Chlorosomen zu untersuchen. Die große Heterogenität der Proben führt jedoch zu einer inhomogenen Verbreiterung der Spektren, und feine spektrale Merkmale, die für bestimmte Struktureigenschaften charakteristisch sein könnten, werden durch die Ensemble-Mittelung überdeckt. Zur Minimierung der inhärenten Probenheterogenität, wurde an einzelnen Chlorosomen des photosynthetischen grünen Schwefelbakteriums *Chlorobaculum (Cba.) tepidum* polarisation-

sauaufgelöste Fluoreszenzanregungsspektroskopie durchgeführt. Dieser Ansatz ermöglicht es, die Eigenschaften der Exzitonzustände ohne Ensemble-Mittelung zu untersuchen.

Durch Kombination dieser Technik mit Mutagenese konnten Chlorosome des Wildtyps und von zwei Mutanten von *Cba. tepidum* untersucht werden, nämlich Chlorosome des *bchR*-einfach-Mutanten und des *bchQR*-doppel-Mutanten. Bei diesen Mutanten werden die verschiedenen Möglichkeiten für die Methylierung der Bakteriochlorophyllmoleküle durch die Deaktivierung verschiedener Gene reduziert. Die verschiedenen Seitenketten der BChl stellen die Hauptquelle für die strukturelle und spektrale Heterogenität der Wildtyp-Proben dar.

Die Spektren aller untersuchten Chlorosome zeigen eine starke Intensitätsmodulation in Abhängigkeit von der Polarisierung der einfallenden Strahlung auf. Dies weist eindeutig darauf hin, dass kollektive Anregungen das Spektrum dominieren. Eine globale Analyse der Spektren ergab, dass die breite Ensemble-Absorptionsbande bei 740 nm aus mehreren spektralen Beiträgen besteht. Die beobachteten photophysikalischen Eigenschaften der einzelnen Chlorosome können mit zylindrischen supramolekularen Strukturen erklärt werden.

In dieser Arbeit werden Informationen aus der polarisationsaufgelösten Fluoreszenzanregungsspektroskopie, Kryoelektronenmikroskopie und theoretischen Modellierung mit Ergebnissen kombiniert, die zuvor aus der NMR-Resonanzspektroskopie und auch Kryoelektronenmikroskopie gewonnen wurden. Es wird gezeigt, dass nur eine Kombination dieser Techniken eine eindeutige Beschreibung der molekularen Anordnung von Bakteriochlorophyllen in Chlorosomen liefert. Die Ergebnisse dieser Techniken zeigen, dass im Gegensatz zu einigen Modellen in der Literatur, sowohl für die Chlorosome des Wildtyps als auch für die der Mutanten, das dominierende sekundäre Strukturelement eine zylindrische Symmetrie aufweist. Darüber hinaus folgen die sekundären Strukturen aller drei Spezies einem sehr ähnlichen Konstruktionsprinzip, das darin besteht, die in [1] veröffentlichte Gitterstruktur unter einem Winkel δ auf einen Zylinder aufzurollen.

Die experimentellen Ergebnisse werden mit Vorhersagen aus Computersimulationen von zylindrischen Modellstruktur verglichen. Die Untersuchung von Variationen der Strukturparameter liefert eine Erklärung für die inhomogen verbreiterten Absorptionsbanden. Darüber hinaus liefern die Simulationen eine quantitative Schätzung der Variation der Krümmung dieser Aggregate. Damit könnten die laufenden Diskussionen über die Struktur von Chlorosomen erklärt werden. Aus der Korrelation spektraler Parameter werden Spekulationen über den Grad der Variation der Strukturelemente angestellt und die Zusammensetzung einzelner Chlorosome daraus abgeleitet. Die Kombination aller Ergebnisse ergibt schließlich ein schlüssiges Bild des Inneren der Chlorosome.

List of Publications

- [2] Günther, L. M.; Jendryn, M.; Bloemsma, E. A.; Tank, M.; Oostergetel, G. T.; Bryant, D. A.; Knoester, J.; Köhler, J. *The Journal of Physical Chemistry B* **2016**, 120, 5367-5376.*
- Contribution: I performed all described polarization-resolved fluorescence-excitation measurements and analyzed the experimental data on the basis of an algorithm provided by E. A. Bloemsma. I used an algorithm provided by E. A. Bloemsma as a starting point and adapted the code for the simulations. Furthermore, I interpreted the data and wrote the paper together with J. Köhler.
- [3] Günther, L. M.[†]; Löhner, A.[†]; Reiher, C.; Kunsel, T.; Jansen, T. L. C.; Tank, M.; Bryant, D. A.; Knoester, J.; Köhler, J. *The Journal of Physical Chemistry B* **2018**, 122, 6712-6723.
- Contribution: I performed the described polarization-resolved fluorescence-excitation measurements on the chlorosomes of the *bchQR* mutant. Together with A. Löhner, I analyzed the experimental data on the basis of an algorithm provided by E. A. Bloemsma. Furthermore, I interpreted the data and wrote the paper together with A. Löhner and J. Köhler.

*The data in this publication was partially collected in my master thesis [4].

[†]L.M.G. and A.L. contributed equally.

Contents

1	Introduction	1
2	Light-harvesting in green sulfur bacteria	5
2.1	The structure of green sulfur bacteria	6
2.2	Photosynthesis, light-harvesting and the antenna complex: the chlorosome	7
3	Secondary structures in chlorosomes	11
3.1	Research on chlorosomes and previous model structures	11
3.2	Contrasting models of cylinders and lamella structures in chlorosomes . .	14
3.3	Mutants of <i>Cba. tepidum</i> created by gene inactivation	15
3.4	Cylindrical model structures for aggregates in chlorosomes	17
4	Photophysics of molecular aggregates	23
4.1	The dimer model	23
4.2	Molecular aggregates	26
4.2.1	Linear aggregate	26
4.2.2	Homogeneous ring	27
4.3	Light-matter interaction in cylindrical aggregates	27
5	Materials and methods	31
5.1	Preparation of chlorosomes	31
5.2	Preparation of single-particle samples	31
5.3	Single-particle spectroscopy	32
5.4	Model simulations	34
6	Polarization-resolved fluorescence-excitation spectroscopy of individual chlorosomes	35
6.1	Spectra of chlorosomes from the wild type, the <i>bchR</i> mutant and the <i>bchQR</i> mutant	37
6.2	Analysing polarization-resolved spectra with a global fit routine	39
6.3	Polarization properties of the spectra of individual chlorosomes from the wild type	44
6.4	Orientation of the transition dipole moments of BChls in cylindrical structures	46

6.5	Reconstruction of LD spectra from the polarization-resolved spectra	52
6.6	Discussion of WT-group2	57
7	Structure and structural variations of light-harvesting aggregates in chlorosomes	59
7.1	Modelstructure of the secondary structures in chlorosomes	59
7.2	Theoretical modeling of the spectra of model structures	63
7.3	Spectral variations explained as variations of the model structure	66
7.3.1	Simulations of variations of the radius r , rolling angle δ and lattice parameter a	66
7.3.2	Correlation between the energetic separation of spectral components and the radius of cylindrical structures	67
7.4	Discussion	71
8	Summary	77
	Appendices	79
A	Additional experimental data	81
A.1	Decomposition of the polarization-resolved fluorescence-excitation spectra	81
A.1.1	Spectra of the wild type	81
A.1.2	Spectra of the <i>bchR</i> mutant	82
A.1.3	Spectra of the <i>bchQR</i> mutant	82
A.2	Distribution of the relative phase angles $\Delta\Phi_{ij}$	83
A.2.1	Distribution of $\Delta\Phi_{ij}$ of the wild type	83
A.2.2	Distribution of $\Delta\Phi_{ij}$ of the <i>bchR</i> mutant	83
A.2.3	Distribution of $\Delta\Phi_{ij}$ of the <i>bchQR</i> mutant	84
A.2.4	Distribution of $\Delta\Phi_{ij}$ of WT-group1	84
A.2.5	Distribution of $\Delta\Phi_{ij}$ of WT-group2	85
A.2.6	Mean values and standard deviations of the distributions of the relative phase angles	85
A.3	Stacking distances of <i>bchR</i> mutant chlorosomes from cryo-electron microscopy	86
A.4	Correlations between the energetic separations of the spectral components	87
B	Effect of misalignment of structures for polarization-resolved fluorescence-excitation and LD spectra	89
B.1	Polarization-resolved spectra	89
B.2	LD spectra	93

List of Figures

2.1	Schematic illustration of the structure of prokaryotic cells of green sulfur bacteria based on an electron microscopy image	6
2.2	Schematic model of the chlorosome and the photosynthetic energy pathway	8
2.3	Molecular structure of BChl <i>c</i> and <i>d</i>	9
2.4	Absorption spectra of BChl monomers <i>a</i> , <i>c</i> and <i>d</i>	10
3.1	Electron microscopy images of chlorosomes	12
3.2	Cryo-EM image of a chlorosome showing lamellar structures	13
3.3	Various models of the internal structural elements in chlorosomes	14
3.4	Absorption spectra of an ensemble sample of chlorosomes from the wild type, the <i>bchR</i> mutant, the <i>bchQR</i> mutant, and the <i>bchQRU</i> mutant . . .	16
3.5	Schematic representation of four stacking models for the arrangement of BChl molecules	18
3.6	Model structures of the secondary elements in chlorosomes from the wild type and the <i>bchQRU</i> mutant	19
3.7	Schematic representation of stacking models for the arrangement of BChls in chlorosomes of the WT and the <i>bchQR</i> mutant	21
4.1	Two-state quantum system	23
4.2	Energy diagram of dimeric H- and J-aggregates	25
4.3	Schematic representation of a ground and an excited energy level of <i>N</i> molecules with interaction <i>V</i>	26
4.4	Geometry of a cylindrical aggregate	28
5.1	Schematic illustration of the single-particle spectroscopy setup	32
6.1	Polarization-resolved fluorescence-excitation spectra of individual chlorosomes from the WT, the <i>bchR</i> mutant and the <i>bchQR</i> mutant	37
6.2	Polarization-resolved fluorescence-excitation spectrum of an individual chlorosome from the <i>bchR</i> mutant	38
6.3	Polarization-resolved fluorescence-excitation spectrum decomposed into four Gaussians	40
6.4	Distributions of the spectral peak positions and FWHM of fitted Gaussians contributions	42

6.5	Distributions of the relative phase angles $\Delta\Phi_{12}$ and $\Delta\Phi_{34}$	43
6.6	Correlation between the relative phase angles $\Delta\Phi_{12}$ and $\Delta\Phi_{13}$	45
6.7	Distributions of the energetic separation ΔE_{12} and ΔE_{34}	46
6.8	Distributions of the relative phase angles $\Delta\Phi_{12}$ and $\Delta\Phi_{34}$ of the chlorosomes from WT-group1.	47
6.9	Molecular aggregate with cylindrical symmetry and the orientation of the corresponding transition dipole moments	48
6.10	Distributions of the ratio of the oscillator strength O_1/O_2 and O_3/O_4	49
6.11	Distributions of the angles β that are enclosed between the transition dipole moments of the monomers and the symmetry axis of the cylinder	51
6.12	Ensemble LD spectrum and individual LD spectra of chlorosomes from the WT, the <i>bchR</i> mutant and the <i>bchQR</i> mutant	53
6.13	Fluorescence-excitation spectra, LD spectra and their gaussian contributions of individual chlorosomes	55
6.14	Distributions of the relative phase angles Φ_{12} and Φ_{34} of the chlorosomes from WT-group1 and WT-group2	57
6.15	Distributions of the spectral peak positions and of the widths (FWHM) of the fitted Gaussians in the spectra of chlorosomes from WT-group1 and WT-group2	58
7.1	Lattice structure of the bacteriochlorophyll monomer arrangement	61
7.2	Model structure for secondary elements in the chlorosomes of the WT, the <i>bchR</i> mutant and the <i>bchQR</i> mutant	62
7.3	Simulation of the polarization-resolved fluorescence-excitation spectrum from two cylindrical aggregates	64
7.4	Simulation of the polarization-resolved fluorescence-excitation spectrum from two cylindrical aggregates	65
7.5	Simulated spectra from cylinder structures based on the model structure	66
7.6	Correlation between the energetic separations of the low- and the high-energy doublet ΔE_{12} and ΔE_{34}	68
7.7	Energetic separation $\Delta E_{\parallel,\perp}$ as a function of the cylinder radius	70
7.8	Speculation about the variation of the overall supramolecular arrangement of the BChl molecules between individual chlorosomes	71
7.9	Intensity of single chlorosomes from WT-group1 as a function of the energetic splitting	72
A.1	Polarization-resolved fluorescence-excitation spectra and decomposed spectrum of individual chlorosomes from the WT	81

A.2	Polarization-resolved fluorescence-excitation spectra and decomposed spectrum of individual chlorosomes from the <i>bchR</i> mutant	82
A.3	Polarization-resolved fluorescence-excitation spectra and decomposed spectrum of individual chlorosomes from the <i>bchQR</i> mutant	82
A.4	Distributions of the relative phase angles $\Delta\Phi_{ij}$ of chlorosomes from the WT	83
A.5	Distributions of the relative phase angles $\Delta\Phi_{ij}$ of chlorosomes from the <i>bchR</i> mutant	83
A.6	Distributions of the relative phase angles $\Delta\Phi_{ij}$ of chlorosomes from the <i>bchQR</i> mutant	84
A.7	Distributions of the relative phase angles $\Delta\Phi_{ij}$ of chlorosomes from WT-group1	84
A.8	Distributions of the relative phase angles $\Delta\Phi_{ij}$ of chlorosomes from WT-group2	85
A.9	Cryo-electron micrograph of an individual chlorosome from the <i>bchR</i> mutant and average of 16 cryo-EM images	86
A.10	Correlation between the energetic splittings ΔE_{ij} and ΔE_{kl} of individual chlorosomes from the <i>bchR</i> mutant	87
A.11	Examples of spectra from individual chlorosomes marked in red in A.10a .	88
B.1	Schematic illustration of mutually perpendicular oriented cylinder structures, where both symmetry axes are oriented perpendicular to the optical axis	89
B.2	Schematic illustration of mutually perpendicular oriented cylinder structures, where one symmetry axis is oriented perpendicular to the optical axis	90
B.3	Variation of the angle β as a function of n and as a function of the ratio of the oscillator strengths	92
B.4	Schematic illustration of a cylinder with its transition dipole moments μ_{\parallel} and μ_{\perp}	93
B.5	LD spectra of a simulated cylindrical arrangement of BChl molecules . . .	94
B.6	Ensemble LD spectra with a variation of the orientation of the chlorosomes with respect to the perfect orientation	95

List of Tables

3.1	Side groups of BChl <i>c</i> and BChl <i>d</i> and of the BChls as synthesized by the mutants <i>bchR</i> , <i>bchQR</i> , and <i>bchQRU</i>	15
3.2	Parameters of the 2D lattice structure of the arrangement of BChls obtained by NMR and molecular modeling	20
3.3	Summary of the values of the model parameters for the WT, the <i>bchQR</i> mutant and the <i>bchQRU</i> mutant	20
6.1	Mean values (standard deviations) of the spectral positions E_i and linewidths W_i (FWHM) of the Gaussian contributions	41
6.2	Mean values (standard deviations) of the relative phase angles $\Delta\Phi_{12}$ and $\Delta\Phi_{34}$	44
6.3	Mean values (standard deviations) of the energetic separations and relative phase angles	47
6.4	Mean values (standard deviations) of the ratios of the oscillator strengths O_1/O_2 and O_3/O_4	50
6.5	Mean values (standard deviations) of the distributions of the molecular dipole angles β_{12} and β_{34}	50
7.1	Summary of the values of the model parameters of the WT, the <i>bchR</i> and the <i>bchQR</i> mutant	62
7.2	Parameters used to simulate the spectra presented in 7.3 and 7.4	65
7.3	Model parameters used to simulate variations of the spectra	67
7.4	Relation between the radius of the underlying cylinder structure and the energetic separation $\Delta E_{\parallel,\perp}$	69
A.1	Mean values (standard deviations) of the relative phase angles $\Delta\Phi_{ij}$	85

Abbreviations

ADP	adenosine diphosphate
APD	avalanche photo diode
ATP	adenosine triphosphate
BChl <i>a</i>	bacteriochlorophyll <i>a</i>
BChl <i>c</i>	bacteriochlorophyll <i>c</i>
BChl <i>d</i>	bacteriochlorophyll <i>d</i>
<i>Cba. tepidum</i>	<i>Chlorobaculum tepidum</i>
<i>Cb. tepidum</i>	<i>Chlorobium tepidum</i> (former name of <i>Cba. tepidum</i>)
CCD	charge-coupled device
CsmA	chlorosome envelope protein A
cryo-EM	cryoelectron microscopy
DFT	density functional theory
DNA	deoxyribonucleic acid
DTT	dithiothreitol
FMO	Fenna-Matthews-Olson Complex
FWHM	Full width at half maximum
LD	linear dichroism
LH	light-harvesting (complex)
NAD(P)H	nicotinamid adenin dinucleotid (phosphate)
NMR	nuclear magnetic resonance
OD	optical density
PMSF	phenylmethylsulfonyl fluoride
WT	wild type (of <i>Cba. tepidum</i>)

1 Introduction

The law of conservation of energy is one basic principle in physics [5, 6]. It states that energy can neither be created nor destroyed.

Wir gehen aus von der Annahme, dass es unmöglich sei, durch irgend eine Combination von Naturkörpern bewegende Kraft fortdauernd aus dem nichts zu erschaffen. HERMANN VON HELMHOLTZ, 1847

We will set out with the assumption that it is impossible, by any combination whatever of natural bodies, to produce force continually from nothing. A. HENFREY & T. HUXLEY, 1853

Energy is needed in everyday life of every human. We need energy for many applications, such as heating, driving machines (locomotion), and lighting. Although energy can neither be produced nor consumed, we still refer to energy production and consumption. We talk about energy production when we mean the conversion of energy from different sources into forms that are useful for humans. On the other hand, we refer to energy consumption when this energy is used by humans and converted into useless forms (like heat released to the environment). As the population grows, so does the worldwide consumption of energy [7]. Until now, energy production has been mainly based on fossil fuels (70%). Both the dwindling reserves of fossil fuels and their contribution to the destruction of the environment and climate are increasing the need for environmentally friendly alternatives for energy production. By far, the most important energy source available to us is the sun. Its energy can be used directly in form of solar energy or indirectly in form of bioenergy (biomass), hydropower, and wind energy. Together with geothermal and marine energy, they form the category of renewable energies. Solar energy is already being harnessed utilizing photovoltaics, solar thermal energy, solar chemical energy, and solar updraft towers. However, the efficiency of such power plants is often still very low. Silicon-based solar cells have, for example, the energy efficiency of up to 19%, whereas organic solar cells, which in contrast to silicon-based ones, are cheap and environmentally friendly to manufacture, only have an energy efficiency of 15% [8]. While we have been working on the development and improvement of such techniques for less than 200 years,

biological organisms have been using solar energy in the direct form for billions of years, namely with photosynthesis. It might, therefore, be an opportunity to use nature as a model for efficient and environmentally friendly harvesting of solar energy.

The idea of observing nature in order to transfer its phenomena to technical innovations is well known through Leonardo da Vinci. However, even before the famous polymath, people were fascinated by mimicking nature. For example, the possibility of rising into the air like a bird inspired them to draw and then to build first flying machines. Inventiveness and perseverance made it possible, that today not only people can travel long distances quickly by air, but also that large quantities of goods are transported between continents. This mimicry of nature in the field of technology is called Bionics. Nature provides the ideas for bionic inventions. Nevertheless, in order to apply these phenomena to modern technologies, it is necessary to study nature. This means, in the case of solar energy, studying photosynthesis.

Photosynthesis is a type of metabolism. The metabolism of living organisms is based on the conversion of energy. It represents the sum of chemical and physical processes that convert food or fuel into energy or life-sustaining building blocks. Different types of metabolism can be found depending on the type of living being. In biological evolution, bacteria developed different sizes, shapes, and metabolism. In this way, they were able to adapt to almost every habitat. Bacteria are found in environments with moderate temperatures like the human body (mesophiles) but also in extreme habitats like hydrothermal vents (extremophiles). Species of extremophile bacteria are able to thrive in extreme conditions. They can survive very high or very low temperatures, high pressure, acids, radiation, and dryness [9]. The ability to adapt to extreme conditions makes these bacteria interesting for biomimetics. There are organisms whose highly efficient photosynthesis apparatuses enable them to live photoautotrophically, i.e., exclusively with light as their energy source, even at the lowest light fluxes. Green sulfur bacteria, for example, only need a light intensity of 1% of full moonlight, which corresponds to 10^9 photons/(s cm²), to grow phototrophically [10]. These organisms must exhibit a molecular structure that absorbs, transfers, and converts photons into chemical energy in a highly efficient way, to achieve such efficiency of the photosynthesis process. The light-harvesting antennae of the mentioned green bacteria are called chlorosomes. In the chlorosome, these bacteria form supramolecular structures of chromophores via self-assembly. The self-assembly represents an outstanding feature, which is in contrast to other light-harvesting antennas that require protein scaffolds for the arrangement of the chromophores. The electronic structure in all light-harvesting antennae systems is determined by the spatial arrangement of the individual molecular building blocks. This yields a strong structure-function-relationship. Therefore, optical spectroscopy offers access to the construction of these systems. Natural systems often show a heterogeneity regarding their composition and structure. Their experimental spectra are broadened by these biological variations, and

spectral features might be lost by ensemble-averaging. Hence, spectroscopy on single objects such as individual antenna systems yields an essential contribution to elucidating the design and function of these structures [11]. For the reasons stated above, the chlorosome represents a supramolecular approach towards artificial light-harvesting studying the structure and function of such efficient light harvesting-apparatuses, in order to create photosynthetic materials based on porphyrins and chlorophylls that convert solar energy into electricity or biofuel [12]. The subject of this thesis is, therefore, the study of the secondary structures in chlorosomes.

This thesis presents a study of fluorescence-excitation spectroscopy on individual chlorosomes from the green sulfur bacterium *Cba. tepidum*. In combination with several other techniques such as mutagenesis, cryo-electron microscopy, and theoretical modeling, this leads to the elucidation of the structure in individual chlorosomes. Furthermore, the variations of the structures in chlorosomes were studied with the presented techniques. Most of the results presented in this thesis have already been published in the publications [2] and [3]. The thesis is organized as follows:

First, the photosynthesis of green sulfur bacteria is introduced, and the composition and structure of chlorosomes are described in detail, including their supramolecular arrangement of the chromophores (see chapter 2). Chapter 3 gives an overview of the research on chlorosomes so far, including the most relevant results. Special attention is given to contrasting models of the pigment arrangement in chlorosomes in the literature. Speculations are made about the cause of these apparent contradictions. In the second half of this chapter, a model structure is presented in more detail, which was developed using measurements on the chlorosomes of mutants of *Cba. tepidum*. Since this work is based on measurements on the wild type and mutants of this species, this model serves as a starting point for the interpretation of the experiments in this work. In order to be able to draw conclusions from the spectroscopic experiments on the structure of the examined chlorosomes, the photophysical properties of molecular aggregate structures are considered in chapter 4. Materials and methods used for the experiments on the chlorosomes are presented in chapter 5. The experiments on individual chlorosomes from the green sulfur bacterium *Cba. tepidum* are presented and evaluated in chapter 6. In chapter 7, the data is discussed and interpreted in terms of a model structure. In chapter 8, a summary of the results of the experiments and the resulting information on the structure of the aggregates in chlorosomes is given. The appendix contains additional diagrams of the data, as well as supporting information on the results.

2 Light-harvesting in green sulfur bacteria

One type of metabolism used by plants, algae, archaea, and some species of bacteria is photosynthesis. It is a unique, physiologic process in which the energy of absorbed light is transformed into chemically stored energy. Photosynthetic species use this process to convert low-energy substances into high-energy biomolecules. Depending on the species, photosynthesis evolves in numerous different ways. The term photosynthesis summarizes a variety of biochemical processes that convert light energy into chemical energy. The first step in a photosynthesis reaction is the absorption of light. Photosynthetic organisms use different types of light-harvesting antenna to collect light. Among them are photosystems I and II in green plants and cyanobacteria, the LH2-complex, and the LH1-complex in purple photosynthetic bacteria and phycobilisomes in cyanobacteria and algae [13–15], and chlorosomes found in green sulfur bacteria and some green non-sulfur bacteria. The chlorosomes are an early invention of antenna systems in photosynthesis and highly efficient [16, 17]. The photosynthesis of various species differs by the reductants, processes, and structures that occur in the cell for photosynthesis. All these processes have in common the extraction of electrons by oxidation of the reductant. In this process, an electron is brought to a higher energy level by using light energy. The electron is used to form the energy-rich compounds ATP and NAD(P)H from ADP and NAD(P)⁺. These compounds extract carbon from carbon sources (carbon dioxide (CO₂) or organic compounds) and synthesize high-energy organic substances. The photosynthesis process can be divided into oxygenic and anoxygenic photosynthesis. As the name suggests, anoxygenic photosynthesis does not produce oxygen as a by-product of the process. This type of photosynthesis is carried out by obligate anaerobes, such as green sulfur bacteria [13, 18–20].

Since in this work, the antenna complexes of the green sulfur bacteria *Chlorobaculum tepidum* (*Cba. tepidum*) were studied, this chapter only describes the photosynthesis of green sulfur bacteria*. The focus will be on the structure of such bacteria and their photosynthetic process towards their antenna complexes, the chlorosomes.

*For a detailed description of plant photosynthesis see references [13, 18, 19] and references [19, 20] for the photosynthesis of algae, archaea, and bacteria

2.1 The structure of green sulfur bacteria

Bacteria (and other living organisms) that perform photosynthesis are called phototrophs. Phototrophs produce complex organic compounds (e.g., proteins) from simple substances present in their surroundings with light as an energy source. The class of phototrophic bacteria includes green sulfur bacteria, non-sulfur bacteria, cyanobacteria, and purple bacteria. The green sulfur bacteria represent a photoautotrophic and anaerobic family of bacteria. The green sulfur and non-sulfur bacteria have their unique light-harvesting complexes in common, the so-called chlorosomes. However, they belong to different phyla[†]: *chlorobi* or *chloroflexi*. An example of a photoautotrophic green non-sulfur bacterium is *Chloroflexus aurantiacus* [21–23]. On the other hand, the bacterium *Chlorobaculum tepidum* (formerly known as *Chlorobium tepidum*), belongs to the known representatives of the green sulfur bacteria [10, 24–26]. In figure 2.1, a sketch illustrates the schematic structure of a green-sulfur-like bacterium next to an electron microscopy image, which was taken from reference [24]. The electron micrograph shows a thin section of cells from *Cba. tepidum*. Typically the dimensions of an individual cell of *Cba. tepidum* are 0.6–0.8 μm x 1.3–2.6 μm .

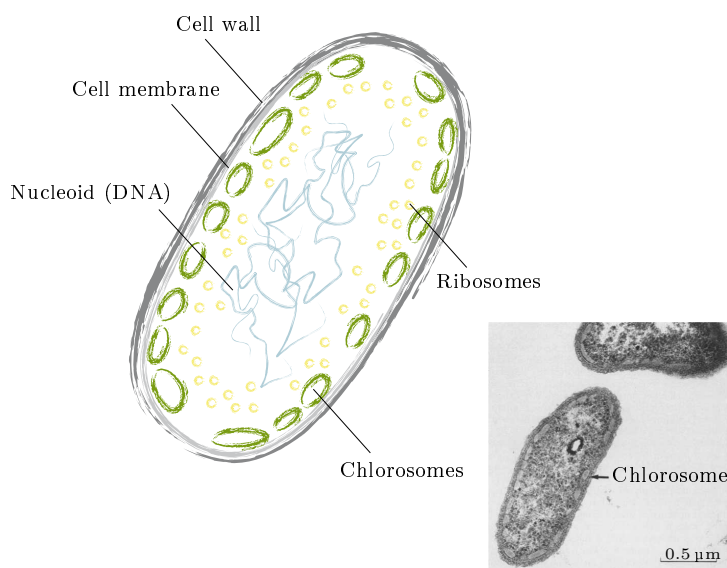


Figure 2.1: Schematic illustration of the structure of prokaryotic cells of green sulfur bacteria based on an electron microscopy image [24].

Prokaryotic cells show a simpler structure than the eukaryotic cells of multicellular organisms. The intracellular components (e.g., proteins and DNA) are not organized in cellular compartments but located in the cytoplasm enclosed by the cell membrane. The cell wall surrounds the membrane and provides structural support and protection

[†]A phylum (plural: phyla) is a level of taxonomic rank. The terms phylum and division are accepted as equivalent.

for the cell. The cell membrane, a phospholipid bilayer, encloses the cell interior and separates it from the extracellular environment. Proteins, embedded in the membrane, control the uptake and release of substances. The cytoplasm consists mainly of water and contains the intracellular components, organic molecules, salts, and enzymes. As there are no compartments in prokaryotes, the area in the cytoplasm containing the single DNA is denoted the nucleoid. The ribosomes are the macromolecular complexes in cells for the production of proteins. The chlorosomes represent a special type of vesicle in these bacteria, namely the antenna complex of the bacterium. They are located at the cell membrane [24]. Their structure and function are described in detail in the next section.

2.2 Photosynthesis, light-harvesting and the antenna complex: the chlorosome

Photosynthesis in green sulfur bacteria

The light absorption and energy transfer process of green sulfur bacteria in the context of the photosynthesis structures in the cell is shown in figure 2.2. The antenna system, in this case, the chlorosome, absorbs a photon. Chlorosomes can be described as a large ellipsoid bag stuffed with self-aggregated chromophores [27, 28]. The structure of the chlorosome is described in detail below. The resulting excitation energy is then transported in the direction of a reaction center via FMO complexes, which are located between the chlorosome and the cell membrane. The FMO complex (named after the scientists who discovered it, Fenna, Matthews and Olson [29, 30]), a chlorophyll-containing protein structure, ensures a directed energy transport towards the reaction center via an energy cascade [31]. In figure 2.2, it is depicted that the Fe-S type reaction centers are embedded in the cell membrane. This is where redox reactions take place in which the reductant (H_2S) is decomposed. In this reaction, elemental sulfur H_3O^+ -ions and electrons are generated.

The structure of the chlorosome

One of the key aspects of photosynthesis in terms of efficiency is the absorption of light. For efficient light-harvesting, the cell needs a large absorption area, and a broad radiation spectrum must be covered. Individual pigments can only collect a little amount of light because they are small and usually have only narrow absorption bands. Therefore the pigments in antenna systems are often organized in light-harvesting complexes, such as the chlorosome. The chlorosome is a large ellipsoidal vesicle with dimensions of 100–200 nm (length), 40–60 nm (width) and 10–40 nm (height) [16, 32–35]. The envelope, the cytoplasmic boundary of the chlorosome, consists of a lipid monolayer. It

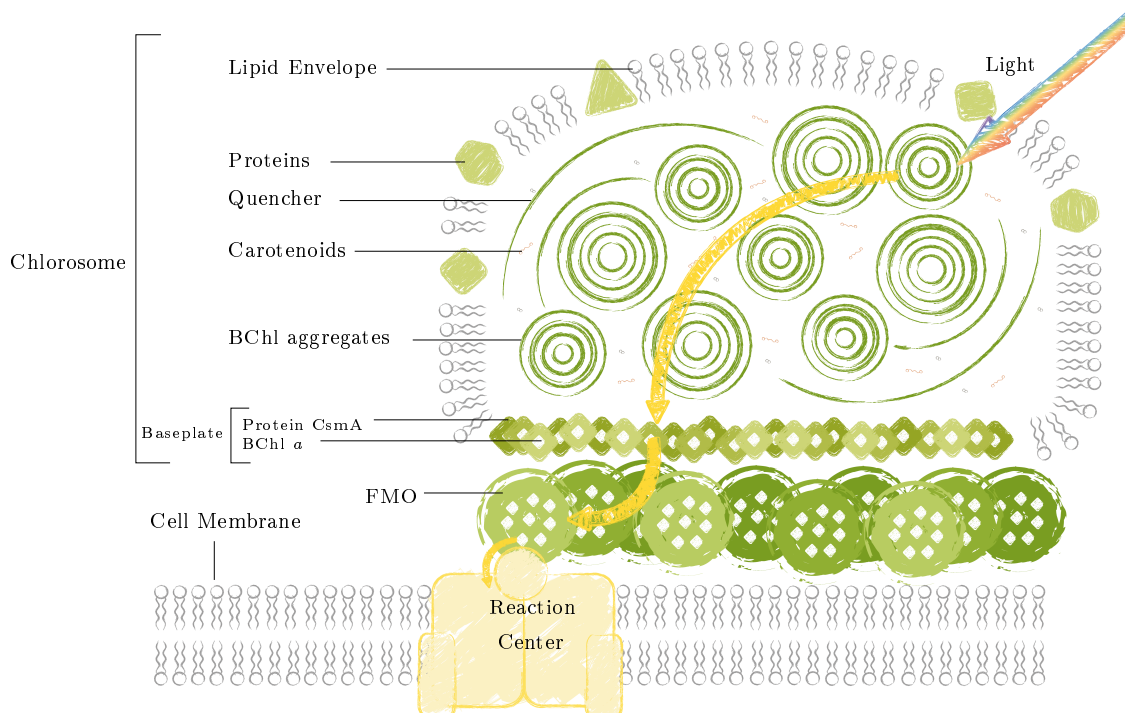


Figure 2.2: This schematic model shows the structure of the photosynthesis apparatus of green sulfur bacteria. The chlorosome is displayed as a cut through its longitudinal axis. The individual components of the chlorosome, such as the lipid envelope, proteins, chromophores, and the baseplate, are labeled. The light absorption and energy transfer is represented by the arrows. This figure is adapted from reference [16].

contains the chlorosome proteins, which are unique to the chlorosomes. The chlorosome's envelope contains 200 000–250 000 self-aggregated chromophores, which corresponds to a concentration in the order of 1–3 M. Despite the high concentration of chromophores, it is remarkable that the proper positioning of the chromophores avoids the expected quenching. In contrast to other antenna systems, this arrangement is achieved without a supporting protein structure, purely by self-aggregation. The secondary structures are stabilized by van der Waals forces and hydrogen-bonding interactions. In addition to the secondary structures of bacteriochlorophylls, the interior of the chlorosome also contains carotenoids and quinones. The carotenoids make up 10% of the pigments contained in the chlorosome. In addition to their function as absorbers, they serve as a photoprotector in the light-harvesting complexes and are possibly involved in the arrangement of the BChls. Quinones regulate the energy transfer from the BChl molecules to the baseplate. They quench excitations in the presence of oxygen to slow down the rate of photosynthesis to protect the light-harvesting aggregates. The region of the envelope facing the cell membrane is called the baseplate. The baseplate is a paracrystalline structure of bacteriochlorophyll *a* and the protein CsmA. As a single BChl *a* molecule is bound per

CsmA protein, the chromophore density of BChl *a* in the baseplate is not as high as the concentration of chromophores inside the chlorosome [16, 31, 36].

Structural and spectral properties of bacteriochlorophyll

There are different types of photosynthetic pigments in phototrophic bacteria: BChl *a*, *b*, *c*, *d*, *e*, *f*, and *g*. They differ in their structure and their attached side chains. Bacteriochlorophylls *a*, *b*, and *g* are bacteriochlorins. Their molecules feature a bacteriochlorin macrocycle ring with two reduced pyrrole rings. Bacteriochlorophylls *c* and *d*, as well as BChl *e*, and BChl *f* are chlorins. Chlorin molecules are composed of a macrocycle ring with one reduced pyrrole ring. The most commonly occurring BChls in chlorosomes, which form the secondary light-collecting structures, are BChl *c* and *d* [17]. Since the structure of the monomers is important in the formation of aggregates in chlorosomes, the molecular structure of BChl *c* and *d* is shown in figure 2.3. The molecular structure consists of a derivatized porphyrin ring and a Mg^{2+} ion in its center. Another 5th ring is attached to the porphyrin of the bacteriochlorophyll backbone. Depending on the type of BChl, various side chains (R_1 , R_2 , R_3) are attached to the backbone. The table in figure 2.3 lists the side groups with which BChl *c* or BChl *d* is created.

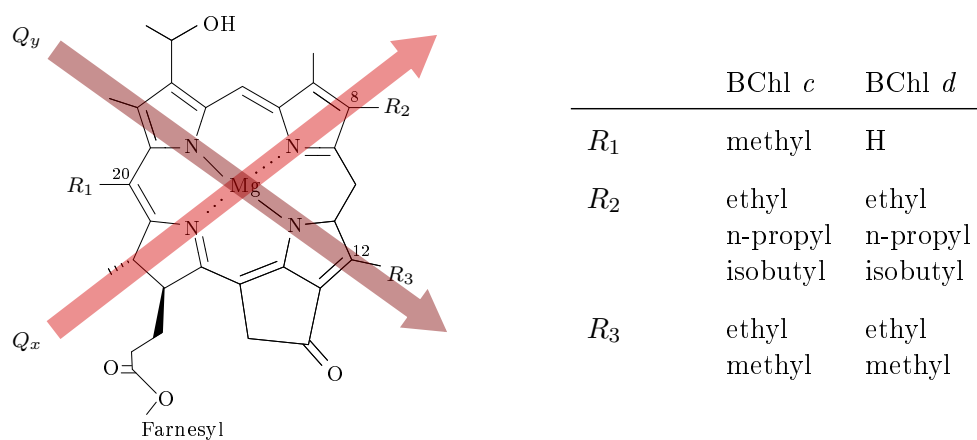


Figure 2.3: Molecular structure of BChl *c* and *d* (adapted from [1]). The possible side groups for R_1 , R_2 and R_3 are listed in the table [37].

In figure 2.4 the absorption spectra of monomeric BChl *a*, BChl *c* and BChl *d* are shown. The absorption of bacteriochlorophylls shows two absorption bands, one in the blue/UV regime and one in the red or near-infrared region, as shown in figure 2.4. These absorption bands are the result of transitions of electrons in the conjugated π -systems. The two higher-energy transitions are commonly called Soret bands, whereas the lower-energy transitions are called Q_x - and Q_y -band. The electronic transitions have different

orientations with respect to the molecular structure. The transition with the highest energy is polarized along the y-axis of the molecule and is called Q_y -band. Analogously, the transition polarized along the x-axis of the molecule is referred to as the Q_x -transition. The direction of the transition dipole moments is represented by the red arrows in figure 2.3 [38].

The structure of the BChl monomer, more precisely the side chains R_1 , R_2 and R_3 determine the absorption properties of the monomer. The absorption peak of the Q_y -peak of BChl *a* (770 nm) is strongly shifted to the red with respect to the Q_y -peak of BChl *c* (666 nm) and BChl *d* (655 nm). The absorption spectra of bacteriochlorophyll monomers can already give a small insight into the absorption properties of chlorosomes. With an absorption band in the visible range from 350–550 nm, carotenoids extend the absorption band of the chlorosomes [36].

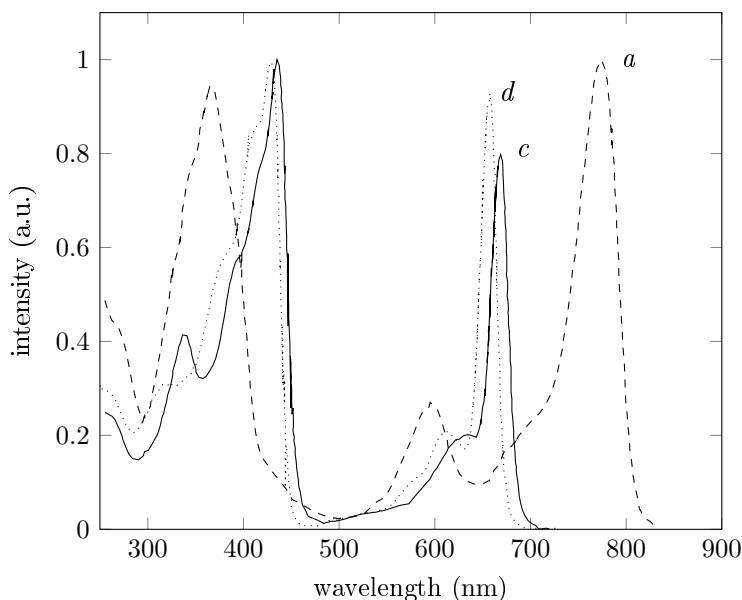


Figure 2.4: Absorption spectra of BChl monomers. *a*, *c* and *d* label the spectra from BChl *a* (dashed line), BChl *c* (solid line) and BChl *d* (dotted line). The absorptivity of a BChl molecules is in the order of $10^5 \text{ M}^{-1} \text{ cm}^{-1}$. The data is extracted from reference [36].

However, the properties of the monomers differ considerably from those of the aggregated chromophores in chlorosomes. Since the function (absorption properties and energy transport) of BChl aggregates is strongly linked to their structure (arrangement of molecules), the next chapter will describe in detail the state of knowledge about the secondary structures in chlorosomes and present published model structures.

3 Secondary structures in chlorosomes

3.1 Research on chlorosomes and previous model structures

The molecular organization of the light-harvesting structures in chlorosomes determines the efficiency of energy transfer in the antenna complex [39]. The supramolecular arrangement of BChl to secondary structures is crucial for their ability to collect light, as it dictates the character of the electronically excited states. Therefore the structure of chromophore aggregates in chlorosomes is the focus of many research projects and still a subject of debate. In order to get an impression of the field of research on the internal structure of chlorosomes, an overview of previous research results in this field will be given below. The overview is limited to the chlorosomes of green bacteria and does not claim to be complete, as there are countless publications in this field.

In 1964 chlorosomes, at that time called chlorobium vesicles, were extracted from cells of *Chlorobium* strain for the first time [32]. The intravesicular structures of chlorosomes from *Chlorobium thiosulfatophilum* were characterized by electron microscopy in 1979 (see figure 3.1a). With this technique, structures with diameters of 9–10 nm were observed in the chlorobium vesicles. They were described as “commonly but not always circular” [40]. A model of the supramolecular architecture of these structures in chlorosomes from *Chloroflexus aurantiacus* using freeze-fracture electron microscopy was presented in 1978 by Staehelin et al. (see figure 3.1b). In their description the chlorosome was in the form of an elongated sac, containing rod-shaped elements with diameters of approximately 5.2 nm, which are made up of periodically repeating globular subunits. Furthermore, they report that the rod elements extend the full length of the chlorosome [41].

An important finding in the investigation of the supramolecular structures in the chlorosomes was the selfassembly of the BChls. The BChls form aggregates within the chlorosomes without a protein framework [27, 28]. Based on this, the arrangement of the pigments with respect to each other was investigated in detail, as it determines the supramolecular structure of the aggregates. Spectroscopic methods such as absorption, emission, and linear dichroism spectroscopy were used to obtain information about the mutual orientation of the transition dipole moments of the pigment molecules [42]. Since the transition dipole moments have a fixed position within the chromophores, molecular modeling was used to create initial models of the aggregate structures from chlorosomes of *Chloroflexus aurantiacus* and *Cba. tepidum* built up from individual molecules [43].

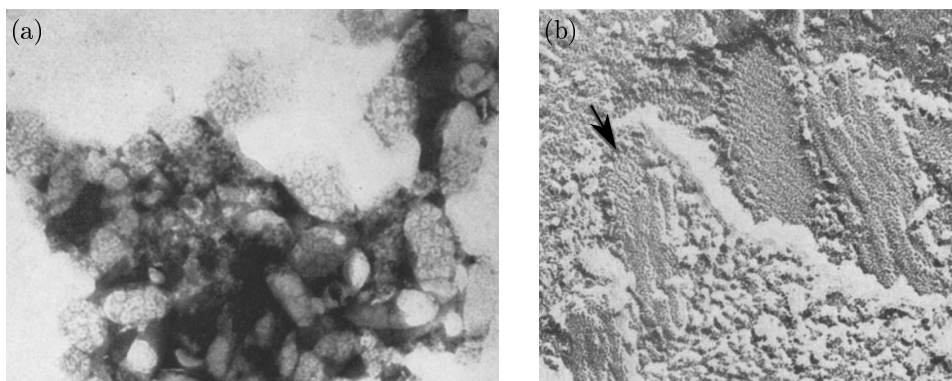


Figure 3.1: (a) Electron microscopy image of the vesicle fraction of *Chlorobium thiosulfatophilum* [40]. (b) Freeze-fractured electron microscopy image of chlorosomes illustrating the closely packed, parallel rod elements and the crystalline baseplate (arrow) [41].

In the following years, further experimental techniques such as NMR spectroscopy were used to refine the presented models [44]. The improvement of cryo-electron microscopy to higher resolutions and using x-ray scattering brought up a lamellar model structure of semicrystalline lateral arrays for the arrangement of BChls in chlorosomes [45] (see figure 3.2). It is worth noting that up to this point, only ensembles of chlorosomes were studied in the spectroscopical experiments. Therefore, only statements about the inter-chlorosome heterogeneity of an ensemble were made, since differences between individual chlorosomes cannot be investigated with these techniques. Single-particle techniques diminish the inter-chlorosome heterogeneity as only one chlorosome at a time is studied. This leaves only the intra-chlorosome heterogeneity, which means that the structures within a chlorosome can also differ from each other.

In 2006, fluorescence spectra of individual chlorosomes were measured to investigate the excited states of chlorosomes [47]. With this technique, the extent of inhomogeneity within a single chlorosome was estimated, and it was shown that the spectra of the chlorosomes of *Cba. tepidum* are already inhomogeneously broadened at the single-chlorosome level. As the single-molecule techniques add a large value in the studies of chlorosomes, recent studies investigated the exciton states of the aggregates in individual chlorosomes by polarization-resolved fluorescence-excitation spectroscopy [48, 49]. The measurements on chlorosomes from the wild type of *Cba. tepidum* revealed a strong modulation of the fluorescence-excitation spectrum as a function of the polarization of the excitation light. This feature of the spectra indicates a high degree of organization of the chromophores into secondary structures in chlorosomes. Furthermore, the polarization features are consistent with a helical arrangement of BChl molecules in cylinders and/or spirals. This

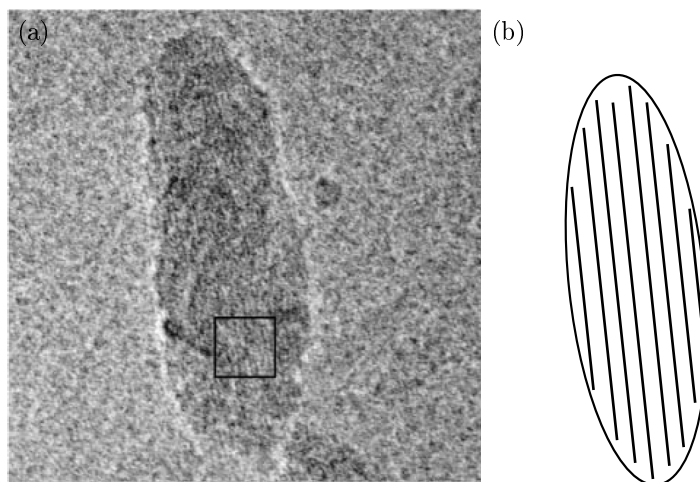


Figure 3.2: (a) Electron cryomicroscopy (cryo-EM) image of a chlorosome [45]. (b) Schematic representation of lamellar structures in a chlorosome with a parallel orientation of the lamellae with respect to the long axis of the chlorosome [46].

was shown by comparing simulated spectra of various models of the supramolecular organization of BChls in chlorosomes to the experimental ones. In this way, spectroscopic experiments contribute to the elucidation of the secondary structures in chlorosomes.

Ganapathy et al. published in 2009 and 2012 the most detailed structural model of chlorosomes to date [1, 50]. These studies use a combination of several experimental and theoretical techniques to investigate the chlorosomes of the wild type and mutant species of *Cba. tepidum*. A lattice arrangement of the BChls was obtained by NMR spectroscopy and molecular modeling. In combination with the information from cryo-electron microscopy, the lattice was used to develop a cylindrical model of the secondary structures in chlorosomes. The tubular model structure was obtained by wrapping the 2D lattice onto a cylindrical surface. This model represents a milestone in the research on chlorosomes. It serves, therefore, as a starting point for model development in this work. This model is described in detail in section 3.4.

Time-resolved studies of the excitation energy transfer in chlorosomes also contribute to the development of structural models of chlorosomes [51, 52]. In order to determine model structures from time-resolved femtosecond transient absorption spectroscopy, simulations of various models generated by molecular mechanics calculations were conducted. Statements about the structural arrangement of the chromophores can only be drawn from a comparison of experiment and theoretical modeling, as is the case for all spectroscopic methods.

The findings in research on chlorosomes so far show that the secondary structures in chlorosomes of various species are differently developed. Various experimental tech-

niques revealed intra- and inter-chlorosome heterogeneity, which was observed as variations in the spectra of individual chlorosomes. These heterogeneities are associated with structural variations of the supramolecular arrangements. These variations also prevent structural determination with atomic resolution using X-ray crystallography.

It is clear that the heterogeneity of the chlorosome samples has to be diminished, and single-chlorosome techniques have to be used to study the structure of chlorosomes by spectroscopy. Although the mentioned studies deal with the challenges resulting from the heterogeneity of the samples, still different models for the secondary structures of chlorosomes are debated in the literature. In the following, these different models will, therefore, be compared, and possible reasons for this contradiction will be discussed.

3.2 Contrasting models of cylinders and lamella structures in chlorosomes

As we are looking at a natural system, with a significant degree of heterogeneity, it is not surprising that several studies have found different models for the structure of BChl arrangement in chlorosomes. First microscopic images of the interior of chlorosomes showed cylindrical structures [40].

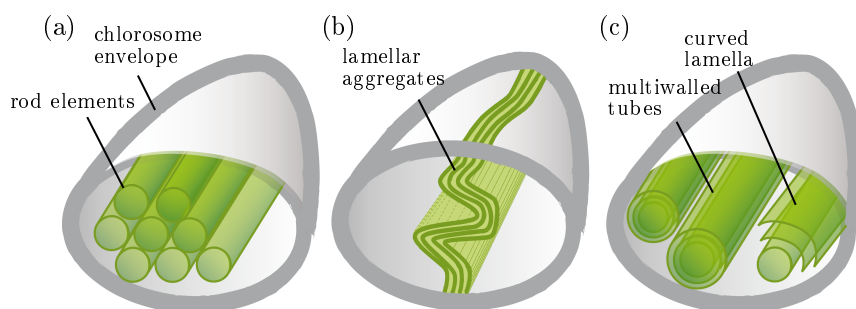


Figure 3.3: Models of the internal structural elements in chlorosomes. (a) Cylindrical structures [53], (b) lamella structures [45], (c) mixture of differently curved structural elements [52].

The model of BChls arranged in cylindrical structures, as depicted in figure 3.3a, was confirmed, refined, and extended by further experimental and theoretical methods [44, 53–56]. Nevertheless, from the results of similar methods, a lamella model was concluded [45, 46, 57] (see figure 3.3b). In particular, it was claimed that data from higher resolution cryo-EM and X-ray diffraction is only compatible with a lamellar organization of the BChls and rule out the cylindrical model. As illustrated in figure 3.3b the results from these studies suggest a model of curved lamellar structures. Based on further cryo-EM observations, as well as spectroscopic experiments, also a model of curved elements with cylindrical symmetry was proposed [1, 50, 58, 59] (see figure 3.3c). A possible way out of

this debate of contrasting models might be a combination of these structures within one chlorosome, which was presented by Linnanto et al. [52]. Since all these models are the result of well designed and carefully conducted studies, it is not helpful to question one model or the other. It is, therefore, necessary to consider explanations that may clarify this conflict.

Most studies on the secondary structures in chlorosomes from *Cba. tepidum* were performed on ensemble samples of chlorosomes from the wild type stem of *Cba. tepidum*. Such studies do not take into account the differences between chlorosomes and can, therefore, only provide information about an average from the structures in an ensemble of chlorosomes. The elimination of this inter-chlorosome heterogeneity has already contributed to the elucidation of the secondary structures in chlorosomes [47, 58–60]. Nevertheless, it is very likely that different growth conditions, such as lighting intensity, nutrient content, and other environmental factors, can lead to different formations of the aggregates. Therefore, intra-chlorosome heterogeneity remains a problem in elucidating these structures.

3.3 Mutants of *Cba. tepidum* created by gene inactivation

Since the individual aggregates in the chlorosome are composed of individual BChls, it can be assumed that the structure of the BChls contributes to the heterogeneity of structures in chlorosomes. As seen in figure 2.3, various side groups can be attached to the molecular structure of BChl.

Table 3.1: Possible side groups of BChl *c* and BChl *d* as synthesized in wild type of *Cba. tepidum* as well as the side groups of bacteriochlorophyll synthesized by the mutants *bchR*, *bchQR* and *bchQRU* [37].

	BChl <i>c</i>	BChl <i>d</i>	<i>bchR</i>	<i>bchQR</i>	<i>bchQRU</i>
R_1	methyl	H	methyl	methyl	H
R_2	ethyl n-propyl isobutyl	ethyl n-propyl isobutyl	ethyl n-propyl isobutyl	ethyl	ethyl
R_3	ethyl methyl	ethyl methyl	methyl	methyl	methyl

In table 3.1 on the left side, the possible side groups of BChl from table 2.3 are listed again. The chlorosomes of the wild type of *Cba. tepidum* contain mostly BChl *c* with a variation of the listed side groups. It is easy to understand that a mixture of these BChls may lead to different structures of the secondary elements in chlorosomes. In 2003 Bryant et al. created mutants of *Cba. tepidum*. By gene deactivation they reduced

the methylation of the side groups R_1 , R_2 and R_3 . On the right hand side of table 3.1 the remaining side groups for the BChl of the $bchR$ mutant, the $bchQR$ mutant and the $bchQRU$ mutant are shown. The terms $bchQ$, $bchR$, and $bchU$ denote the deactivated genes [37]. The mutants show a similar photosynthetic growth rate as the WT, with a slightly reduced light-harvesting efficiency.

Comparing the absorption spectrum of BChl c in figure 2.4 and the absorption spectrum of the wild type chlorosomes, which contain almost exclusively BChl c , in figure 3.4 a shift of the Q_y -peak absorption peak of the spectrum from the chlorosome to larger wavelength (peak position 740 nm [4]) with respect to the monomer spectrum (peak position 666 nm [36]) can be observed. The shift of the peak position in the spectrum is a result of the self-aggregation of the BChls in chlorosomes and the resulting interaction of the monomers.

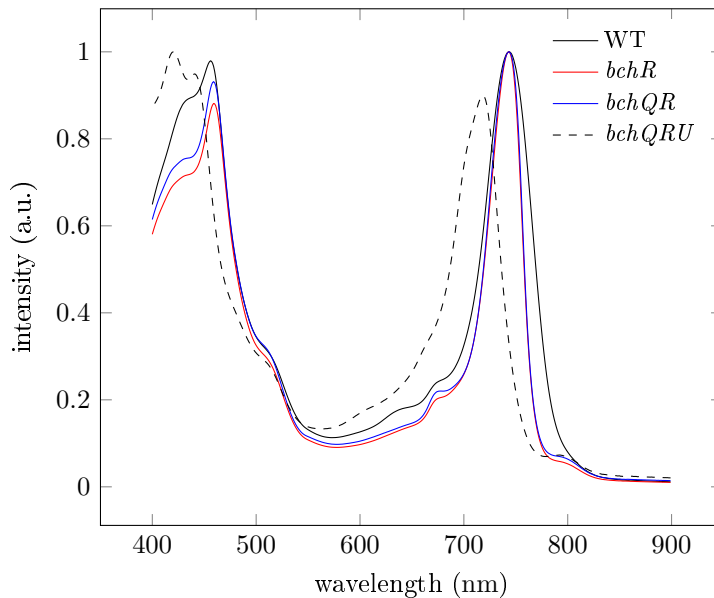


Figure 3.4: Absorption spectra of an ensemble sample of chlorosomes from the wild type, the $bchR$ mutant, the $bchQR$ mutant, and the $bchQRU$ mutant. (data from [4])

The mutations $bchR$ and $bchQ$ do not change the peak position of the absorption spectrum of the chlorosomes from these species ($\text{peak}_{bchR} = 740$ nm, $\text{peak}_{bchQR} = 743$ nm) compared to the spectrum of the wild type chlorosomes ($\text{peak}_{WT} = 743$ nm), as can be seen in figure 3.4. In contrast the mutation $bchU$ converts the BChl c to BChl d . The peaks of the absorption spectrum of the BChl d monomer (655 nm) as well as the one of the $bchQRU$ mutant chlorosomes containing BChl d (716 nm) are blue shifted with respect to the BChl c and the WT spectra, respectively. On the blue wing the spectra exhibit the absorption peak of the Q_x transition dipole moment masked by the strong absorption peak of the Q_y transition dipole moment. On the red wing the absorption of BChl a from the baseplate of the chlorosomes occurs in the shoulder of the

Q_y -peak. The spectra also show a reduction of the width of the Q_y -peak in the spectra of the chlorosomes of the *bchR* mutant and the *bchQR* mutant (both FWHM = 39 nm) compared to one of the wild type chlorosomes (FWHM = 55 nm). The decrease of the absorption bandwidth yields an explanation for the reduced light-harvesting performance of the mutants compared to the WT.

3.4 Cylindrical model structures for aggregates in chlorosomes

Ganapathy et al. obtained a cylindrical model structure by reducing intra-molecular heterogeneity in the chlorosomes via mutagenesis and combining information from NMR, cryo-EM, and molecular modeling [1, 50]. In their study, they investigated the arrangement of BChl *d* molecules with respect to each other in the chlorosomes of the *bchQRU* mutant obtained by magic-angle spinning (MAS), solid-state NMR spectroscopy. They observe a *syn*- and an *anti*-conformation of the BChls. The *syn* (see figure 3.5a) and *anti* (see figure 3.5b) refers to the orientation of the OH ligation of the BChls with respect to their farnesyl side chain. From the experimental data, they developed new possible structural models on a molecular basis: a stacking model based on antiparallel monomer stacking (figure 3.5d) and an alternating *syn-anti* monomer stacking model (figure 3.5f). Density functional theory (DFT) calculations for the new models and the previously published parallel-stack model (figure 3.5c) [55] and piggy-back dimer model (figure 3.5e) [61] showed that only the *syn-anti* model and the parallel-stack model could explain the experimental data.

In cryo-EM images of end-on views of chlorosomes from the *bchQRU* mutant coaxial cylinders were observed. In side views, the concentric structures produced a spacing of (2.10 ± 0.12) nm, which corresponds to an increment of the cylinder radius by 2.1 nm. Furthermore, a spacing of (0.83 ± 0.01) nm was observed in the direction of the long axis of the cylinders. The spacings are a clear indication for a helical arrangement with a repeat distance of 0.83 nm. The structural arrangement of the BChl *d* molecules was determined using molecular modeling. Supramolecular models based on the findings of the NMR spectroscopy could reproduce the spacings from the cryo-EM images and determined the structure presented in figure 3.6.

The obtained lattice structure is shown in figure 3.6a. It consists of a unit cell that accommodates two molecules, which are represented by their transition dipole moments depicted in the form of arrows. The unit cell features the lattice constants $a = 1.25$ nm and $b = 0.98$ nm inclined by an angle $\gamma = 122^\circ$. The colors (red and green) of the arrows represent a tilt of the molecules transition dipole moments by an angle $\alpha = \pm 4^\circ$ in or out of the lattice plane. This tilt of the dipole moments is a result of the *syn-anti* monomer

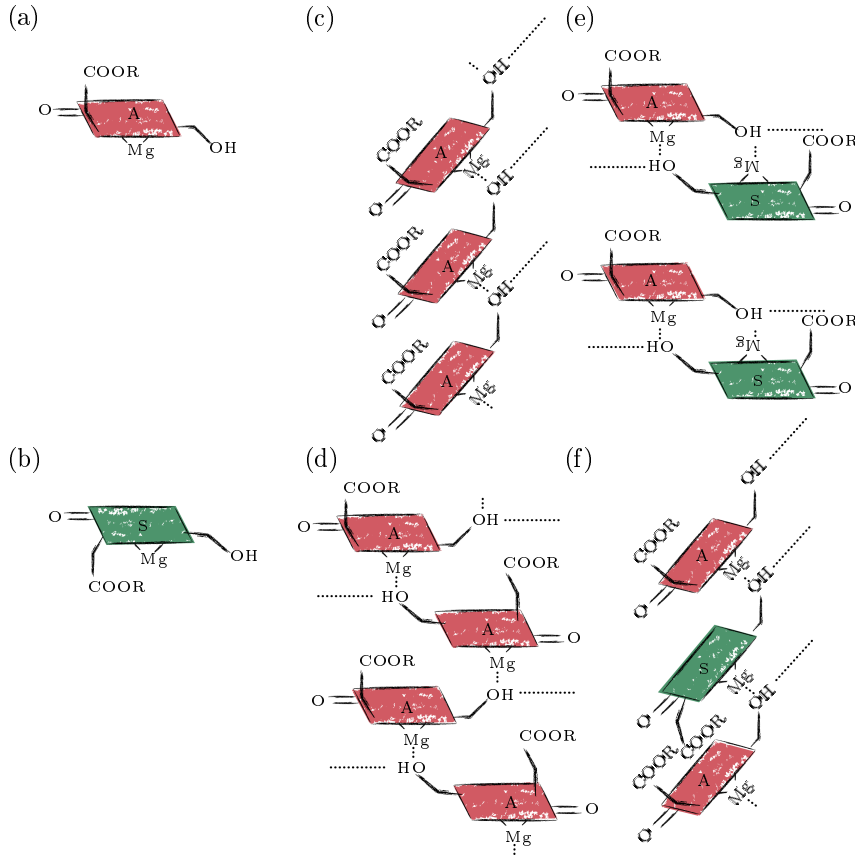


Figure 3.5: (a,b) *Syn-* and *anti-*conformation of the BChls. *S* denotes the *syn*-orientation (green) and *A* the *anti*-orientation (red) of the BChl molecules. (c-f) Schematic representation of four stacking models for the arrangement of BChl molecules. (c) Parallel-stack model, (d) antiparallel monomer stack model, (e) piggy-back dimer model, (f) *syn-anti* monomer stack model [1].

arrangement. The transition dipole moments enclose an angle of $\eta = 35^\circ$ with the *a*-axis of the lattice. An overview of the lattice parameters is given in table 3.2. A tubular model structure was obtained by wrapping the 2D lattice structure, which represents the near-order of the molecules, onto a cylindrical surface. The rolling direction for the structure of the *bchQRU* mutant chlorosomes is determined by the stacking distances measured in the cryo-EM experiments. The corresponding rolling vector is labeled C_{QRU} in figure 3.6a. The resulting cylinder structure is shown in figure 3.6b. With the help of the gridlines of the lattice structure, it can be seen that the molecule stacks form helices running along the surface of the cylinder.

The lattice structure obtained for the arrangement of the BChl *d* molecules in the chlorosomes from the *bchQRU* mutant was then used in combination with the analysis of cryo-EM images to develop a model for the secondary structures in chlorosomes of

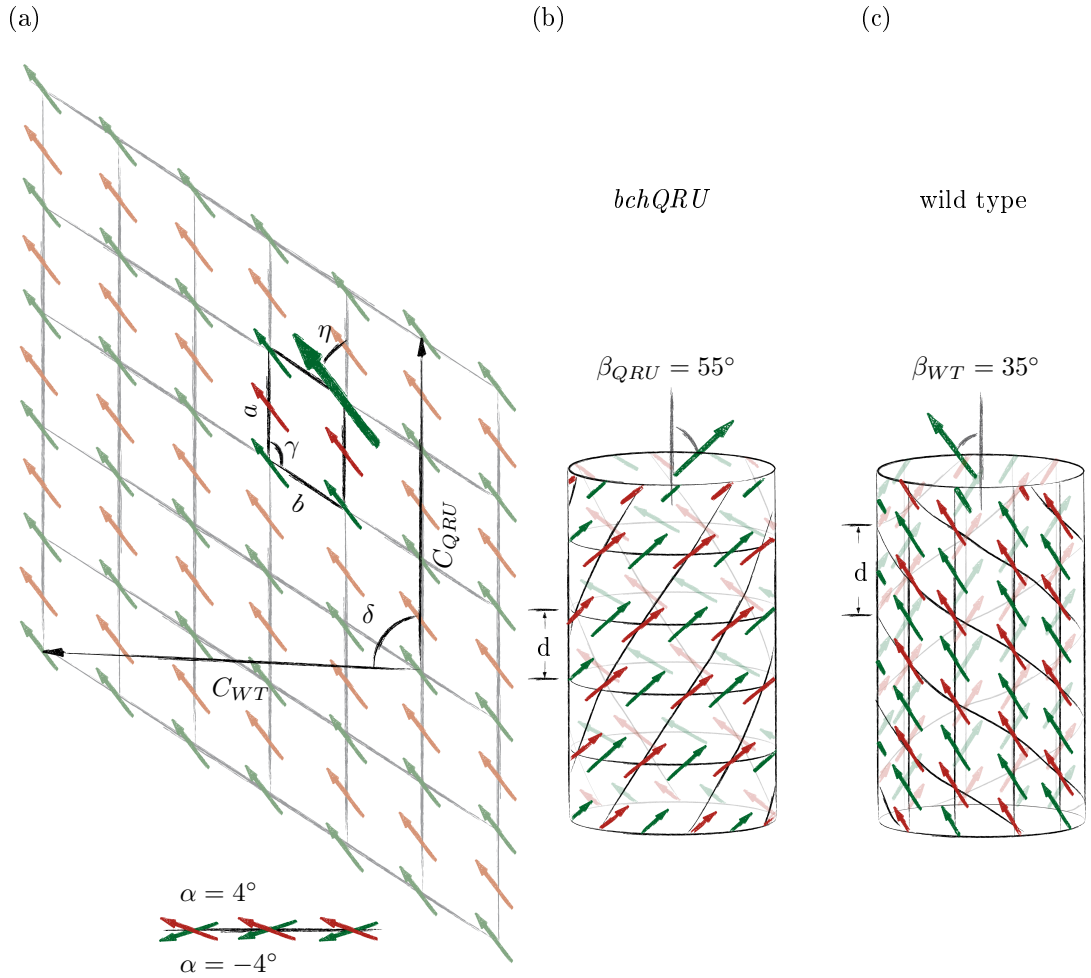


Figure 3.6: Model structures of the secondary elements in chlorosomes as presented in [1]. (a) The lattice structure, which features a unit cell with lattice parameters a and b inclined by an angle γ , was obtained from NMR and molecular modeling. The arrows indicate the transition dipole moments of the molecules. The transition dipole moments make an angle η with the a -axis and are tilted by the angle α in or out of the plane. The rolling vectors are referred to as C_{WT} and C_{QRU} . (b) Together with the information from cryo-EM the lattice structure from panel a was wrapped in a horizontal direction onto a cylindrical surface to create a supramolecular structure model for the chlorosomes of the *bchQRU* mutant. (c) The information from cryo-EM implicated a rolling vector, which inclines an angle δ with the a -axis for the structure of the secondary elements in the chlorosomes from the wild type [1].

the wild type. The cryo-EM images of chlorosomes from the wild type showed a unique organization of BChls in individual chlorosomes. Despite this structural heterogeneity, the Fourier transforms of the cryo-EM images showed a spacing of $d = (1.22 \pm 0.03)$ nm (see figure 3.6c).

It was thus concluded that the aggregates in chlorosomes from the WT could be described by a model of wrapping the lattice structure along the rolling vector C_{WT} , which

Table 3.2: Parameters of the 2D lattice structure of the arrangement of BChls obtained by NMR and molecular modeling [1, 50].

a	1.25 nm
b	0.98 nm
γ	122°
η	35°

encloses an angle of $\delta = 90^\circ$ with the a -axis. The projected model structure shows a layer line in the Fourier transform at 1.25 nm and therefore supports this model.

Using the presented structures, it is possible to determine the angle β that is enclosed by the transition dipole moment and the long axis of the cylinders. For the chlorosomes of the *bchQRU* mutant, this leads to an angle of $\beta_{QRU} = 55^\circ$, whereas an angle of $\beta_{WT} = 35^\circ$ is obtained for the chlorosomes of the wild type.

Table 3.3: Summary of the values of the model parameters for the WT, the *bchQR* mutant and the *bchQRU* mutant from references [1, 50].

	WT	<i>bchQR</i>	<i>bchQRU</i>
δ (°)	90	90	0
β (°)	35	35	55
d (nm)	1.22	0.69	0.83

In a similar study from 2012 [50], chlorosomes from the *bchQR* mutant were investigated in addition to the WT chlorosomes. The NMR measurements and DFT calculations showed that for the *bchQR* mutant chlorosomes, the BChls is arranged in domains of parallel all *syn* or all *anti* stacking. This arrangement results in a stacking distance d of 0.69 nm as this spacing always represents the distance between two *syn* or two *anti* homologues of BChl (see figure 3.7b). Despite establishing a different stacking model for BChls in the *bchQR* mutant chlorosomes the lattice structure presented in figure 3.6 remains the same except for the alignment of the dipole moments, which point alternating in and out of the lattice plane for the WT, whereas a domain-behavior was found for the *bchQR* mutant, as shown in figure 3.7.

A summary of the model parameters, i.e. the angle δ of the rolling vector with respect to the a -axis, the angle β of the BChl dipole moments with respect to the cylinder axis, and the stacking distances d of the molecules in the direction of the long axis of the cylinders, is given in table 3.3 for the model structures of the WT, the *bchQR* mutant, and the *bchQRU* mutant.

In conclusion, these studies presented a lattice structure for the near-order of BChls. A cylindrical model structure was developed by wrapping this grid along the rolling vector

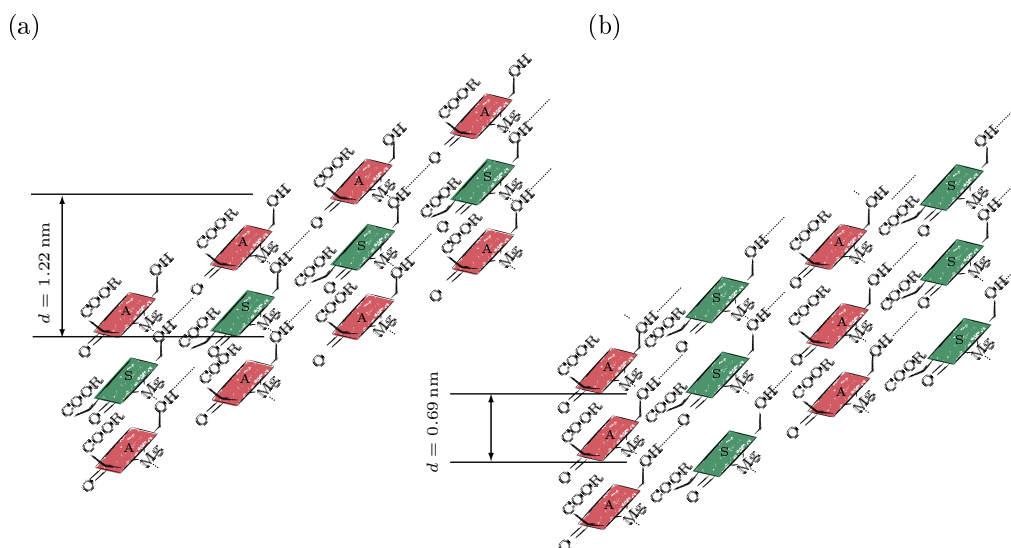


Figure 3.7: Schematic representation of stacking models for the arrangement of BChl molecules in chlorosomes of (a) the WT, and (b) the *bchQR* mutant. Periodicities of 0.69 nm and 1.22 nm, respectively, are indicated. The arrows indicate the direction of the long axis of the chlorosome. A and S stand for BChl molecules that are *syn*- and *anti*-coordinated, respectively [50].

C_{QRU} for the *bchQRU* mutant chlorosomes and along C_{WT} for the WT and the *bchQR* mutant chlorosomes. It has to be noted that the rolling direction of the *bchQRU* mutant model is perpendicular to the rolling direction of the WT model.

4 Photophysics of molecular aggregates

Spectroscopical methods are often used to study the electronic excitations of molecular aggregates, like light-harvesting antenna systems. The correct analysis of the experimental results requires an understanding of the photophysics of such systems. A theoretical description of the interaction between light and a complex system of molecules, such as the chlorosome, is based on limitations and simplifications. Therefore, it is necessary to have a look at a simple system like a dimer to develop the basic formalism for the excitation of complex molecular aggregates.

4.1 The dimer model

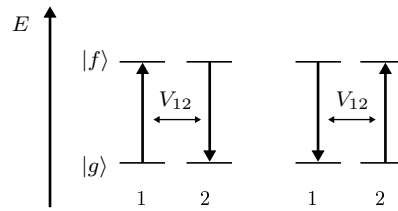


Figure 4.1: Schematic representation of a ground (groundstate $|g\rangle$) and an excited (excited state $|f\rangle$) energy level of two molecules with interaction V_{12} and resonant energy transfer.

The most simple representation of a molecular aggregate is the dimer model. The two molecules of a dimer are connected by covalent bonds (via atomic bonds) or non-covalent bonds, e.g., van der Waals-, dipole-, electrostatic-, and hydrophobic interactions. In figure 4.1 the individual molecules are labeled 1 and 2. With two two-level molecules there are four possible states of the system: both in groundstate $|g\rangle$, either molecule 1 ($|1\rangle$) or molecule 2 excited ($|2\rangle$), or both excited ($|12\rangle$). The states $|1\rangle$ and $|2\rangle$ are degenerated. As long as there is no interaction between the molecules, these are the eigenstates of the system. If there is an interaction between the molecules, the states are getting mixed. In figure 4.1, only the resonant energy transfer is shown. Due to the interaction V_{12} of the molecules, energy is transferred from either molecule 1 to molecule 2 or the other way around. This can be written as Hamiltonian:

$$H = V_{12} (|2\rangle\langle 1| + |1\rangle\langle 2|) \quad (4.1)$$

The energies of the dimer result as the diagonal elements of the Hamiltonian $H = H_0 + V_{12}$:

$$E_{\pm} = \frac{1}{2}(E_1 + E_2) \pm \frac{1}{2}\sqrt{(E_1 - E_2)^2 + 4|V_{12}|^2} \quad (4.2)$$

With $E_m = \frac{1}{2}(E_1 + E_2)$ and $\Delta = \frac{1}{2}(E_1 - E_2)$, E_{\pm} translates to:

$$E_{\pm} = E_m \pm \frac{1}{2}\sqrt{\Delta^2 + |V_{12}|^2} \quad (4.3)$$

The eigenstates, also called exciton states of the system are:

$$|+\rangle = \cos \frac{\Theta}{2}|1\rangle + \sin \frac{\Theta}{2}|2\rangle \quad (4.4)$$

$$|-\rangle = -\sin \frac{\Theta}{2}|1\rangle + \cos \frac{\Theta}{2}|2\rangle \quad (4.5)$$

with $\tan \Theta = \frac{|V_{12}|}{\Delta}$. In the point dipole approximation, where the expansion of the molecules can be neglected, the interaction can be written as:

$$V_{12} = \frac{\vec{\mu}_1 \cdot \vec{\mu}_2}{|\vec{r}_{12}|^3} - 3 \frac{(\vec{\mu}_1 \cdot \vec{r}_{12})(\vec{\mu}_2 \cdot \vec{r}_{12})}{|\vec{r}_{12}|^5} \quad (4.6)$$

The interaction V_{12} depends on the distance \vec{r}_{12} between the two molecules and the position of the molecules, or rather their transition dipole moments $\vec{\mu}$ to each other [62]. Exciton-exciton and exciton-phonon interactions are explicitly not considered in this description.

It should be noted that in this approach, the interaction between the molecules is always small. Within this approximation, the interaction can be further divided into strong and weak coupling depending on the ratio of interaction to disorder $|\frac{V_{12}}{\Delta}|$. Correctly, this interaction would rather be called weak and very weak coupling.

Weak coupling

The term weak coupling is used, if the transition energies of the monomers in the dimer differ strongly from each other or if the interaction between the monomers is small, i.e., $|\frac{V_{12}}{\Delta}| \ll 1$. In this situation, the monomers are almost uncoupled, and the excitations are strongly localized. Incoherent energy transfer takes place between the chromophores, which can be described within the framework of the Förster theory [63]. Such a dimer is also called an inhomogeneous dimer.

Strong coupling

In a homogeneous dimer, one finds almost identical transition energies of the molecules. The disorder becomes negligible in relation to the interaction. The system therefore has

a strong coupling ($|\frac{V_{12}}{\Delta}| \gg 1$).

The eigenstates of this dimer system arise to $|\pm\rangle = \frac{1}{\sqrt{2}}(|1\rangle \pm |2\rangle)$ with the energies $E_{\pm} = \omega_0 \pm V_{12}$, where ω_0 denotes the transition energy between the ground and the excited state. These eigenstates are coherent standing waves, which are delocalized over several molecules and are called Frenkel excitons [64–66]. The total dipole operator of this system results in $\hat{M} = \hat{\mu}_1 \pm \hat{\mu}_2$ and is dependent on the shear angle α of the transition dipole moments with respect to their connecting vector r_{12} . The optical response of the dimer depicted in figure 4.2a can be calculated from the matrix elements of the total dipole operator:

$$\langle \pm | \hat{M} | g \rangle = \frac{(\vec{\mu}_1 \pm \vec{\mu}_2)}{\sqrt{2}} = m^2 (1 \pm \cos \alpha) \quad (4.7)$$

Subsequently, the interaction V_{12} between pigments is also dependent on the arrangement of the transition dipole moments relative to each other. In the dimer arrangement

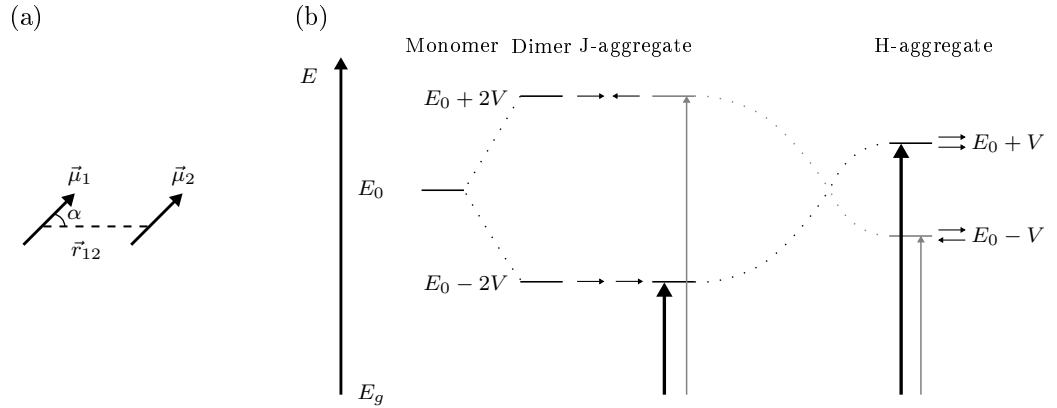


Figure 4.2: (a) Schematic illustration of the transition dipole moments μ_1 and μ_2 together with their connecting vector r_{12} . Both transition dipole moments have a shear angle α with the connecting vector. (b) Interaction of monomers with each other in the form of a dimer changes the transition energy of the resulting system. The transition energy of the dimer is either increased or decreased in relation to the transition energy of the monomers. The arrangement of the molecules is represented by the position of their transition dipoles illustrated by the arrows on the left and on the right sides of the energy levels. In the arrangement of H- or J-aggregates, only one transition is optically allowed. The optically allowed transition is indicated by the thick black arrow, respectively [67].

shown in figure 4.2a, V_{12} is dependent on the shear angle α between the transition dipole moments and calculates to:

$$V_{12} = \frac{\mu^2}{r_{12}^3} (1 - 3 \cos^2 \alpha) \quad (4.8)$$

Here μ^2 is the product of the dipole strength μ_1 and μ_2 . The interaction V_{12} consists of a distance dependent part $V = \frac{\mu^2}{r_{12}^3}$ and an orientational factor $(1 - 3 \cos^2 \alpha)$.

In figure 4.2b, the energies of the monomer and the dimer are shown. The increase or decrease of the energy of the allowed transition state relative to the transition energy of the monomers E_0 depends on the interaction V_{12} and thus the orientation of the monomers to each other. Therefore, different arrangements of the transition dipole moments to each other are considered. On the one hand, the vectors of the transitions are linear in one row while, in the other case, they are parallel. For these arrangements, only one of the resulting transitions is optically allowed and has the entire oscillator strength. This energy state is indicated by the level marked in black and the corresponding transition with the black arrow. In case of the optically allowed transition with a decrease of the transition energy, the aggregate is called J-aggregate, in case of an increase, it is called H-aggregate [68–71].

4.2 Molecular aggregates

One chlorosome contains several hundred thousand chromophores. Previous research (see section 3.1) has shown that these are arranged in aggregates, and many studies suggest a cylindrical arrangement. In order to describe the photophysics of such a system, the dimer system is extended to a linear aggregate chain and a ring in the following. Finally, the linear aggregate and the ring aggregate are combined to describe a cylindrical aggregate.

4.2.1 Linear aggregate

The dimer system is now extended to N molecules, resulting in a linear molecular aggregate. The energy levels of the N molecules are shown in figure 4.3. As only homogenous aggregates are considered, the transition energies of all molecules are equal to E_0 . Between all molecules, there is again an interaction of V . The interaction between molecule m and molecule n is denoted by V_{nm} . The electronic excitation of such a supramolecular molecule aggregate can be described by the model of Frenkel excitons [64, 65].

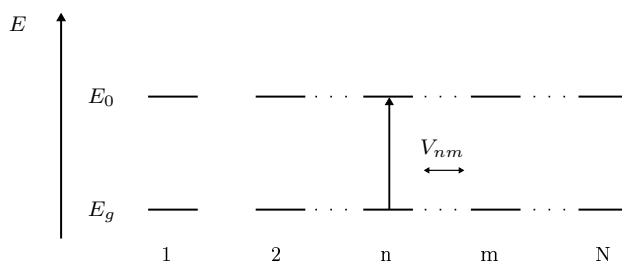


Figure 4.3: Schematic representation of a ground and an excited energy level of N molecules with interaction V

Therefore the electronically excited states are described by a Frenkel exciton Hamilto-

nian using the Heitler-London approximation and open boundary conditions.

$$H = \sum_n E_0 |n\rangle \langle n| + \frac{1}{2} \sum_{\substack{n,m \\ n \neq m}} V_{nm} |m\rangle \langle n| \quad (4.9)$$

The excitation transfer interaction V_{nm} between the molecules is now extended from the dimer model to the aggregate model.

$$V_{nm} = \frac{\vec{\mu}_n \cdot \vec{\mu}_m}{|\vec{r}_{nm}|^3} - 3 \frac{(\vec{\mu}_n \cdot \vec{r}_{nm})(\vec{\mu}_m \cdot \vec{r}_{nm})}{|\vec{r}_{nm}|^5} \quad (4.10)$$

\vec{r}_{nm} denotes the relative position vector with $\vec{r}_{nm} = \vec{r}_n - \vec{r}_m$. Considering only the nearest neighbor interaction, the one-exciton eigenstates of the Hamiltonian result in:

$$|k\rangle = \sqrt{\frac{2}{N+1}} \sum_n \sin\left(\frac{\pi kn}{N+1}\right) |n\rangle \quad (4.11)$$

with the eigenenergies

$$E_k = E_0 + 2V \cos\left(\frac{2\pi k}{N}\right) \quad (4.12)$$

The interaction between the monomers V_{nm} is now replaced with V as we assume only transfer interactions between neighboring chromophores. k denotes the number of the quantum state. The model clearly describes a collective excitation of all molecules as all states are delocalized on the linear aggregate chain. For $N = 2$, equations 4.11 and 4.12 reproduce the results for the homogenous dimer in section 4.1. The nondegenerate state with $k = 1$ holds nearly the entire oscillator strength of this system [72, 73].

4.2.2 Homogeneous ring

It is inevitable to move from open boundary conditions to periodic boundary conditions when looking at a ring-shaped aggregate instead of a linear one. The eigenstates calculate to:

$$|k\rangle = \frac{1}{\sqrt{N}} \sum_n \exp\left(i2\pi k \frac{n}{N}\right) |n\rangle \quad (4.13)$$

and eigenenergies correspond to 4.12. Only three of the eigenstates are dipole allowed, $k = 0$, and the degenerated one with $k = \pm 1$. In a homogeneous, undisturbed ring, the oscillator strength resides only in the two degenerated states $k = \pm 1$ [74].

4.3 Light-matter interaction in cylindrical aggregates

In section 3.4, models for cylindrical aggregates as secondary structures in chlorosomes were presented. The cylindrical aggregates were constructed from a two-dimensional

lattice, which is rolled onto a cylinder surface. A detailed theoretical analysis of such systems was developed by Didraga et al. [74–79] In these studies, the cylindrical aggregate is presented as a composition of a stack of rings rotated with respect to each other, as can be seen in figure 4.4.

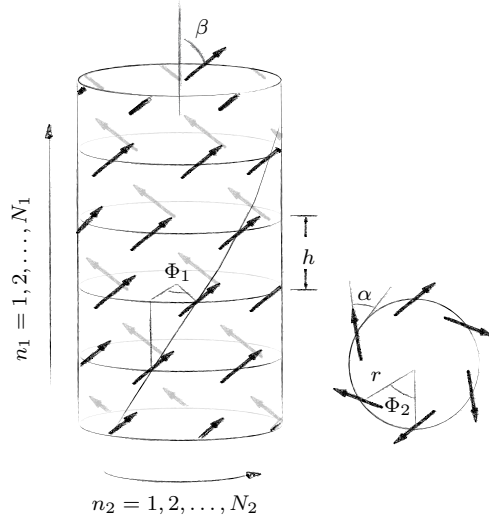


Figure 4.4: The cylindrical aggregate is composed of a stack of rings rotated with respect to each other. The position of the molecules generates helices proceeding around the cylinder. With the given parameters $(r, n_1, N_1, n_2, N_2, \Phi_1, \Phi_2, h, \alpha, \beta)$ the position of each molecule and the orientation of its transition dipole moments is fully defined [75].

The cylinder of radius r is composed of N_1 rings, where n_1 denotes the number of the ring. Φ_1 is the azimuthal angle between adjacent rings in the stack, n_2 the number of the monomer on an individual ring, and N_2 the total number of monomers on a ring. The cylinder consists of $N = N_1 \cdot N_2$ monomers. Φ_2 denotes the azimuthal angle between adjacent monomers within a ring, with $\Phi_2 = \frac{2\pi}{N_2}$. The distance between successive rings is given by h . \vec{r}_n denotes the position of the center of monomer n on the cylinder.

$$\vec{r}_n = \begin{pmatrix} r \cos(n_1 \Phi_1 + n_2 \Phi_2) \\ r \sin(n_1 \Phi_1 + n_2 \Phi_2) \\ n_1 h \end{pmatrix} \quad (4.14)$$

To describe the photophysics of cylindrical aggregates, in addition to the position of the monomers, the orientation of their transition dipole moments must be defined. The transition dipole moments of monomers incline an angle β with respect to the cylinder axis. The projection of the transition dipole moments in the plane of the rings makes an angle α with the local tangent of the ring. The orientation of the transition dipole

moment $\vec{\mu}(n)$ of monomer n is given by:

$$\vec{\mu}(n) = \begin{pmatrix} \mu \sin(\beta) \sin(n_1 \Phi_1 + n_2 \Phi_2 \pm \alpha) \\ \mu \sin(\beta) \cos(n_1 \Phi_1 + n_2 \Phi_2 \pm \alpha) \\ \mu \cos(\beta) \end{pmatrix} \quad (4.15)$$

The electronically excited states are described by the Hamiltonian in equation 4.9. As for the linear and for the ring aggregate, the interaction of the system only depends on the relative positions of the molecules n and m and is given in equation 4.10. The total exciton eigenstates $|\vec{k}\rangle = (k_1, k_2)$ result from the solution of the Hamiltonian to

$$|\vec{k}\rangle = |k_1, k_2\rangle = \sqrt{\frac{1}{(N_1 + 1) N_2}} \sum_n \sin\left(\frac{\pi k_1 n_1}{N_1 + 1}\right) \exp\left(i 2\pi k_2 \frac{n_2}{N_2}\right) |n\rangle \quad (4.16)$$

Only the bands with $k_2 = 0$ and $k_2 = \pm 1$ (degenerated) are dipole-allowed. It emerges from this that only these states contribute to linear absorption spectra. The absorption spectrum of an isotropic ensemble is then given by

$$A(\omega) = \sum_k O_k \delta(\omega - E_k) \quad (4.17)$$

The spectrum is composed of peaks at exciton eigenfrequencies E_k , which are weighted with the oscillator strength O_k . Further calculations of the oscillator strength yield that only the exciton bands with $k_2 = 0$ and $k_2 = \pm 1$ contain states with oscillator strength. The states in the $k_2 = 0$ band are polarized parallel to the axis of the cylinder, whereas the states in the $k_2 = \pm 1$ bands are polarized perpendicular to the cylinder axis. The oscillator strengths of these bands show an proportionality of $\cos^2 \beta$ for the $k_2 = 0$ band and a proportionality of $\sin^2 \beta$ for the $k_2 = \pm 1$.

A linear dichroism (LD) spectrum is the difference of the absorption spectra from linearly polarized light with mutually perpendicular polarization vectors. The calculations of the exciton states show that it is possible to take LD spectra of individual cylinders or oriented samples of cylinders.

$$LD(\omega) = A_{\parallel}(\omega) - A_{\perp}(\omega) \quad (4.18)$$

In principle, it is possible to measure the angle β with this technique. In systems consisting of several cylinders measuring β with this technique relies strongly on a good alignment of the cylinders. However, the measurement of polarization-resolved spectra can provide even more information about a system, like the chlorosomes, in which perfect orientation cannot be achieved.

5 Materials and methods

5.1 Preparation of chlorosomes

The chlorosome samples were prepared by the group of D. A. Bryant at Pennsylvania State University. As described in reference [80] cultures of *Chlorobaculum tepidum* strain ATCC 49652 were cultivated at 48 °C and harvested after 7 days. The cells were mechanically disrupted using a chilled French press. The chlorosomes were separated from the membranes on a continuous sucrose density gradient. The isolated chlorosomes were suspended in phosphate buffer (containing 1 mM PMSF and 2 mM DTT).

A *bchR* mutant and *bchQR* mutant species have been created as described in references [81, 37]. The chlorosomes from these species were extracted in the same way as the ones from the WT. The exact growth conditions of the wild type species and the mutant species, as well as the exact procedure that was used for the extraction of the chlorosomes, can be looked up in reference [80].

5.2 Preparation of single-particle samples

Stock solutions of chlorosomes ($OD_{733}=58$ for a sample of 1 cm thickness) from the wild type, the *bchR* mutant and the *bchQR* mutant were stored at -20 °C in a buffer solution (5 mM dipotassium phosphate (K_2HPO_4), 5 mM monopotassium phosphate (KH_2PO_4), 150 nM sodium chloride (NaCl), pH 7.2 at room temperature). For the preparation of a single-particle sample, the stock solutions were diluted in the same buffer to a concentration of nM. An amount of about 10 μ l of the diluted sample was adsorbed onto a SiO_2 substrate under nitrogen atmosphere for 20 min to 30 min. The chlorosomes align with their long axis parallel to the substrate surface [58, 59]. After spin-coating the samples for 30 s at 2000 RPM to remove any remains from the buffer, the sample was mounted in a helium bath cryostat [2–4].

At room temperature, prereducing the samples with sodium dithionite ($Na_2S_2O_4$) 5 mM causes a significant increase in the fluorescence emission. At cryogenic temperatures, however, there is no dependence of the fluorescence intensity on the reduction of the sample [4]. Therefore the reducing treatment of the samples was only used for room temperature measurements.

5.3 Single-particle spectroscopy

Two individual home-built widefield/confocal microscopes for fluorescence-excitation spectroscopy were used to study the spectral properties of chlorosomes from the WT and the mutants of *Cba. tepidum*. The design and function of the setups are similar. A helium bath cryostat was used to perform spectroscopy at cryogenic temperature. By storing the sample in superfluid helium, the thermal molecular movement and dephasing are reduced and, therefore, also spectral widening. Furthermore, photostability is increased, and photobleaching is nearly completely suppressed. In the following, the general microscope setup is described. The specific components are listed that were used in the setup for the experiments on the WT samples, whereas those used in the setup for the mutants are given in square brackets. Subsequently, details of the polarization-resolved spectroscopy part of the setup will be discussed.

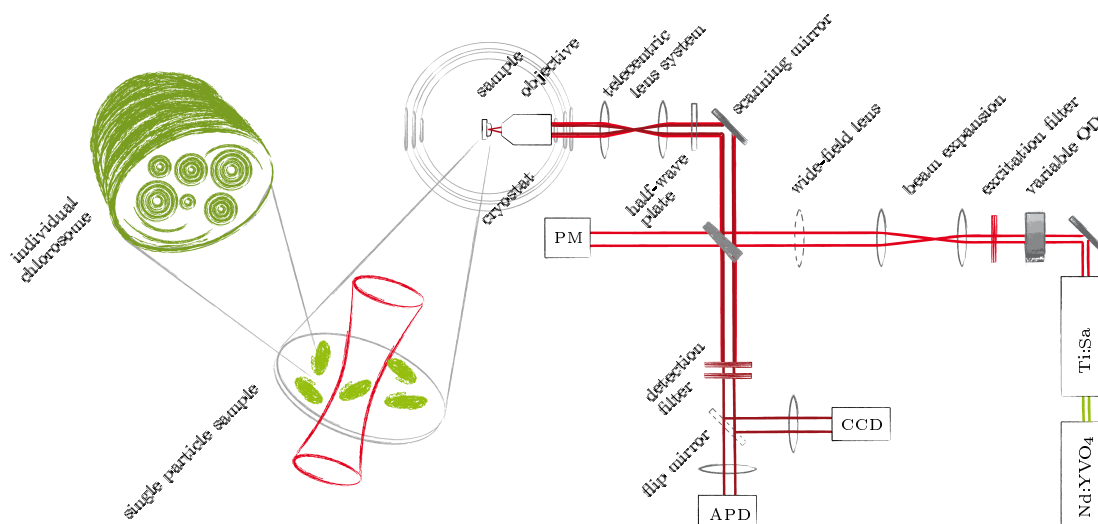


Figure 5.1: Schematic illustration of the single-particle spectroscopy setup. The figure shows the beam path of the laser-generated excitation light to the sample in the cryostat and the detection path for the emitted light. The sample and the objective are located in the cryostat. The section enlargements show a single-particle sample of chlorosomes and the cross-section of a chlorosome. Dashed lines indicate optics that were variably positioned in the beam path.

A tunable titanium:sapphire (Ti:Sa) laser (3900 S, Spectra Physics; [899-01, Coherent]) that is pumped by a frequency-doubled continuous-wave neodymium-yttrium-vanadate (Nd:YVO₄) laser (Millenia Vs, Spectra Physics; [Verdi V10, Coherent]) provided the excitation light in the setup presented in figure 5.1. The laser wavelength was scanned between 718 nm and 775 nm (698 nm–795 nm for the *bchR* and *bchQR* mutant) with a rate of 3 nm/s (2.8 nm/s) by rotating a birefringent filter via a motorized micrometer screw (Actuator 850 F, Motion Controller MM4005, Newport; [Nanomover, Melles Griot]). The

accuracy and the reproducibility of the wavelength variation of the excitation beam was 1 cm^{-1} and was verified with a wavemeter (WaveMaster, Coherent; both setups). The laser beam was linear polarized, perpendicular to the table plane. The laser intensity was controlled using a continuously variable neutral density filter (Variable wedge attenuator M-925B, Newport; both setups). It was adjusted to 25 W/cm^2 (5 W/cm^2 for the *bchR* and the *bchQR* mutant). A bandpass filter (SP 785 RazorEdge, AHF Analysentechnik; [BP 736/128, AHF Analysentechnik]) was used to suppress nonamplified fluorescence from the laser crystal. A system of two lenses (Edmund Optics) was used to expand the beam so that the diameter of the excitation beam corresponds to the diameter of the posterior focal plane of the objective. In this setup, it was possible to place a pinhole between the two lenses to spatially clean the beam profile. However, since the beam showed a clean profile, this was omitted. The excitation path was separated from the detection path using a glass wedge (96% transmission). The part of the beam transmitted by the glass wedge was used for the reference measurement of the laser power parallel to the data acquisition (LaserMate-Q, Coherent; both setups). A combination of a scanning mirror (Thorlabs), a telecentric lens system ($f = 100 \text{ mm}$, Edmund Optics), and an objective (Mikrothek, NA = 0.85; [Edmund Optics, NA = 0.85]) was used to direct the diffraction-limited laser spot on single particles. The objective was mounted in the cryostat and used for focusing the laser beam as well as the collection of the emission from the sample. After passing suitable detection filters (LP 780, AHF Analysentechnik; [BP 850/80, AHF Analysentechnik]) to block residual laser light, the emission from a single particle was focused onto a single photon counting avalanche photodiode (APD) (PCM-AQR-16, PerkinElmer; [SPCM-AQR-15, PerkinElmer]).

For localizing single particles, a wide-field fluorescence image was recorded by defocusing the excitation with an additional lens (Edmund Optics) in the excitation path to a spot size of about $20 \mu\text{m}$. The wide-field fluorescence image was then recorded with a charge-coupled device camera (CCD) (iKon, Andor; [LUCAEM R 604, Andor Technology Ltd.]). From this image, individual, spatially well-separated chlorosomes were selected. After removing the wide-field lens, the diffraction-limited laser spot was directed onto the selected chlorosomes.

Polarization-resolved spectroscopy

The polarization of the excitation light was rotated in steps of steps of 6.2° (3°) between two successive scans by a half-wave plate (Achromatic half-wave plate 400 nm–800 nm, Thorlabs Inc.; both setups) operated by a stepper motor to investigate the polarization dependence of the absorption properties of the samples. A rotation of the wave plate by a certain angle corresponds to twice the angle of rotation of the polarization of the linear excitation light. For each particle, 97-250 of such scans were recorded to determine

the spectral position and polarization dependence of bands [2, 3]. Since the polarization of the emission of the chlorosomes does not depend on the polarization direction of the excitation light, the measurement is not influenced by the fact that excitation and detection beams are partially combined, i.e., the emission passes the waveplates [82].

5.4 Model simulations

For simulations of spectra of the secondary structures in chlorosomes, a model structure was used where the 2D lattice structure, obtained from NMR and molecular modeling [1], was wrapped onto a cylindrical structure (see figure 3.6). Details of this model structure have already been described in section 3.4. The model described in reference [1] presented two rolling directions of the lattice. As seen in figure 3.6 these rolling vectors C_{WT} and C_{QRU} are parallel or perpendicularly to the \mathbf{a} axis of the lattice. This model was used as a starting point. Details of the theoretical description of cylindrical aggregates were given in section 4.3. The adaptation of this model and details to the fine-tuning of the model parameters are described in sections 7.1 and 7.2.

For the simulations, the standard Frenkel exciton Hamiltonian in the Heitler-London approximation was used (see equation 4.9). The excitation transfer interaction between molecules n and m (equation 4.10) was calculated in the point-dipole approximation. The Hamiltonian for a particular cylinder was diagonalized, which yielded the collective excited states. The exciton eigenstates and exciton energies were obtained from the numerical diagonalization of the Frenkel Hamiltonian. From these eigenstates and energies, the fluorescence excitation spectrum was calculated.

$$FE(\omega) = S_k^{-1} \sum_k |\mu_k \cdot e|^2 \exp \left[-(\hbar\omega - E_k)^2 / 2S_k^2 \right] \quad (5.1)$$

The inhomogeneous width S_k expressed as a standard deviation can be converted into a FWHM:

$$W_k = 2\sqrt{2 \ln 2} S_k \quad (5.2)$$

For the simulation of multiwalled cylinders, inter-wall dipole interactions were neglected [75, 76].

6 Polarization-resolved fluorescence-excitation spectroscopy of individual chlorosomes

The following chapter presents, among others, the experiments and the results from publications [2] and [3] and puts them into context. Sections are partly taken directly from the publications.

In chapter 2, the unique features - high light-harvesting efficiency and self-assembly in the absence of a protein scaffold - of chlorosomes with respect to their structure and function were described. Hence, it is understandable that there is a huge interest in elucidating the design principles of such natural systems, because of the great impact of the strategies that are considered for the development of novel organic solar cells [83–85]. However, the detailed supramolecular organization of the BChls in chlorosomes, which dictates the nature of the electronically excited states that determine their light-harvesting performance, is the subject of a still ongoing debate. Previous studies have led to various models for the structure, including tubular, lamellar, and rolled lamellar formations [42, 44, 45, 52, 54, 55, 58, 59, 86] (see section 3.1). In the course of chapter 3, it was explained that this diversity is a direct consequence of the large degree of the structural heterogeneity of the chlorosomes; i.e., variations occur in the size of the aggregates and mixtures of the various types of BChl molecules, which prevent structural determination with atomic resolution using X-ray crystallography. The most detailed structural model that has been proposed to date has emerged from combining genetic modification of the BChl homolog distribution, cryo-EM imaging, molecular modeling, and solid-state nuclear magnetic resonance (NMR) (see section 3.4) [1, 50]. Owing to the more uniform pigment content of a triple mutant (*bchQRU*) and a double mutant (*bchQR*) from the species *Cba. tepidum*, in which the compositions of the BChl side chains were controlled [87], it was possible to grow bacteria with chlorosomes that were structurally more homogeneous than those of the wild type (WT). This yielded a detailed microscopic picture for the *bchQRU* mutant chlorosomes, which in turn has been transferred into a structural model for the WT chlorosomes, and the *bchQR* mutant chlorosomes, featuring the arrangement of BChl *c* molecules in multilayer tubular superstructures (see section 3.4). Additional information about the supramolecular arrangement of the molecular building

blocks is accessible from optical spectroscopy [33, 48, 49, 88]. This is because the properties of the electronically excited states, such as their energetic positions, their oscillator strengths, or the mutual orientations of their transition dipole moments, depend crucially on the structure and the resulting intermolecular interactions within such aggregates [77, 89, 90]. Therefore, the photophysics of molecular aggregates was discussed in chapter 4. Analyzing the photophysics of these systems allows one to test whether a proposed structural model is compatible with the experimentally observed spectra and to discriminate between different structures.

In summary, none of the previous studies have led to a detailed structural model with regard to the structure and photophysics of the chromophoric assembly, either because of inherent sample heterogeneity, a significant degree of structural disorder in the chlorosomes themselves or because spectroscopic data was not considered. Therefore, in this thesis, polarization-resolved fluorescence-excitation spectroscopy was used to obtain information about the structural arrangement of the secondary structures in chlorosomes. Using the detailed model from Ganapathy et al. as a starting point, it seems obvious to study the chlorosomes from the WT and *bchQRU* mutant spectroscopically. However, the *bchU* mutation included in the triple mutant converts BChl *c* into BChl *d* (see section 3.3). Unfortunately, this shifts the monomer absorption from 666 nm to 655 nm in organic solvents [36], and correspondingly, the absorption peak for BChl *d* containing chlorosomes shifts to about 729 nm [80], which is out of the spectral range accessible for fluorescence-excitation spectroscopy in our experimental setup (see chapter 5). Therefore, in this study, chlorosomes from the WT were compared to those from the *bchQR* double mutant and those from the *bchR* single mutant. In the *bchQR* mutant strain, the composition of all three side groups of the BChl molecules is defined, yet the spectral positions of the absorption bands are still within the experimentally accessible range because this mutant also produces BChl *c* [50, 87]. The *bchR* mutant is included as there was no published model of the structure to date. Furthermore, the lower degree of defined side chains in the BChl monomers of this mutant allows a comparison of the spectral heterogeneity of the chlorosomes from the WT, the *bchR* mutant, and the *bchQR* mutant.

Before going into detail and to avoid confusion, it is worthwhile to clarify once more the hierarchies in the structural arrangements of the BChl molecules (as described in chapter 2). First, the BChl monomers form supramolecular aggregates, which determine the internal structure of chlorosomes. Hence, a single chlorosome refers to a small subensemble of several tens of molecular aggregates, each consisting of thousands of BChl molecules. Three organizational levels are distinguished: monomers - aggregates - chlorosomes.

6.1 Spectra of chlorosomes from the wild type, the *bchR* mutant and the *bchQR* mutant

Figure 6.1 shows examples of polarization-resolved, fluorescence-excitation spectra from individual chlorosomes at low temperature (1.2 K-1.5 K). Each row shows three examples of the spectra from the WT, the *bchR* mutant, and the *bchQR* mutant.

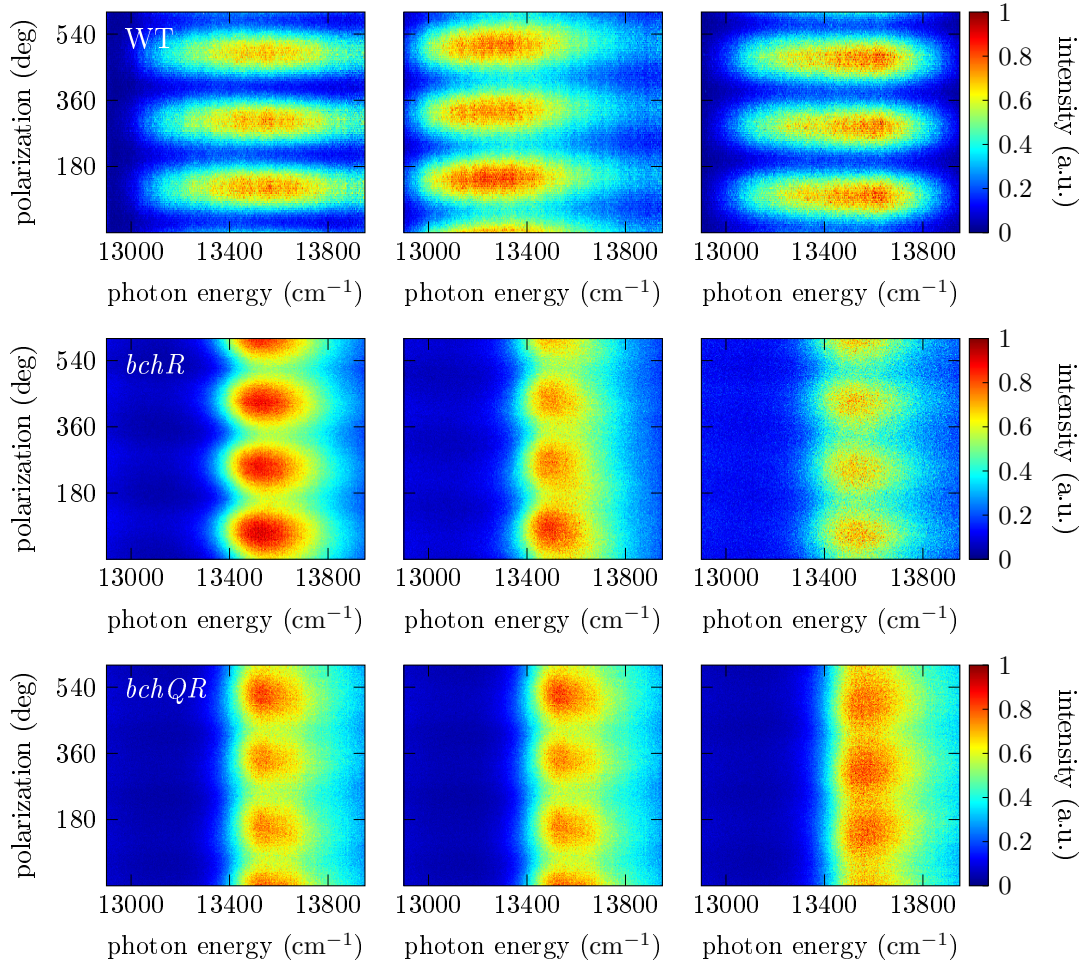


Figure 6.1: Examples of polarization-resolved fluorescence-excitation spectra of individual chlorosomes in a two-dimensional representation. All spectra have been recorded at 1.2 K-1.5 K. (Top row) WT, stack of 97 spectra, recorded with an excitation intensity of 25 W cm^{-1} . (Center row) *bchR* mutant and (Bottom row) *bchQR* mutant, stack of 200 spectra, recorded with an excitation intensity of 5 W cm^{-1} . The relative normalized intensity is given by the color bar.

The spectra in the top row have been taken from single chlorosomes from the WT, whereas the center row shows spectra from single chlorosomes from the *bchR* mutant and the bottom row from single chlorosomes from the *bchQR* mutant. An individual pattern displays 97 (WT) or 200 (*bchR* and *bchQR* mutant) consecutively recorded fluorescence-

excitation spectra, for which the horizontal axis corresponds to the photon energy of the excitation light and the vertical axis corresponds to the polarization angle. Between two successive scans, the linear polarization of the excitation light was rotated by a few degrees. The resulting fluorescence intensity is given by the color code. The spectra show a band that arises from the Q_y -transition of aggregated BChls (see figure 3.4). For details of the experiments see section 5.3.

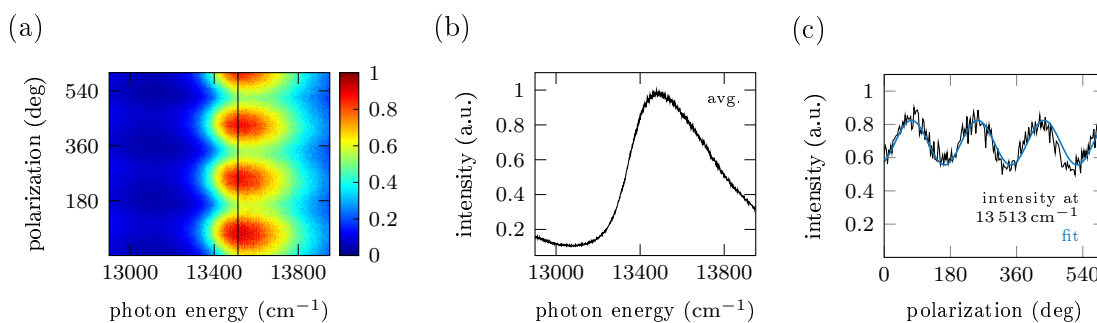


Figure 6.2: (a) Polarization-resolved fluorescence-excitation spectrum of an individual chlorosome from the *bchR* mutant at low temperature (1.5 K). The black line indicates the absorption maximum of the ensemble spectrum of the chlorosomes from the *bchR* mutant at 740 nm (13 513 cm⁻¹). (b) Polarization-independent fluorescence-excitation spectrum (average over all polarizations in panel a) (black) (c) The black line shows the fluorescence intensity modulation as a function of the polarization of the excitation light, whereas the blue line shows a cos²-fit of the data.

Between individual chlorosomes, the spectral patterns show variations in their appearance. However, despite these variations, two observations are striking. First, for the chlorosomes from the *bchQR* mutant (figure 6.1 bottom) and for the chlorosomes from the *bchR* mutant (figure 6.1 center), the widths of spectral features are significantly reduced with respect to those from the WT chlorosomes (figure 6.1 top). This clearly reflects the reduction in heterogeneity owing to the definition of the BChl side groups by mutagenesis. This effect could already be observed in the ensemble absorption spectra (see figure 3.4) of the WT and mutant chlorosomes. Second, for all spectra of the WT, the *bchR* mutant, and the *bchQR* mutant, the intensity is clearly modulated as a function of the polarization of the excitation light with a periodicity of 180° over the entire spectral band. Considering that the spectra are generated by the interaction of hundreds of thousands of transition dipole moments, the observed polarization dependence is most remarkable, indicating that collective excitations dominate the spectrum. This reflects a high degree of organization of the BChl molecules that contribute to a single chlorosome spectrum. This polarization feature was observed in each of the 75 recorded spectra from individual chlorosomes of the WT, 66 spectra of the *bchR* mutant, and 29 spectra of the *bchQR* mutant.

In figure 6.2, a more detailed view on the polarization dependent features of the

spectrum of an individual chlorosome from the *bchR* mutant is shown (the spectrum in panel a was taken from figure 6.1). Averaging over all polarizations of the polarization-resolved fluorescence-excitation spectrum yields the spectrum shown by the black line in figure 6.2b, which features an asymmetric band with a width of 479 cm^{-1} (FWHM) and a maximum at $13\,476 \text{ cm}^{-1}$. The modulation of 180° as a function of the polarization of the excitation light, as seen in the spectra of all measured chlorosomes (see also figure 6.1), is a clear indication for the orientation of the secondary structures in chlorosome. In a 2D representation of the fluorescence intensity as a function of the polarization at a distinct wavelength, the \cos^2 -modulation can be observed directly. Figure 6.2c shows the modulation of the fluorescence intensity as a function of the polarization of the excitation light at 740 nm ($13\,513 \text{ cm}^{-1}$). 740 nm equals the maximum of the ensemble absorption spectrum of the chlorosomes from the *bchR* mutant (see figure 3.4). The fit (blue) with a \cos^2 -function shows a good agreement with the data.

6.2 Analysing polarization-resolved spectra with a global fit routine

In order to analyze the fluorescence-excitation spectra and the underlying spectral contributions more quantitatively, a fit routine based on the following general expression for the polarization-resolved fluorescence-excitation spectrum was developed:

$$F(E, \Theta) = B + \sum_{i=1}^4 A_i(E) \cdot [\cos(\Theta - \varphi_i)]^2 \cdot \exp\left(-\frac{(E - E_i)^2}{W_i^2/4 \ln 2}\right) \quad (6.1)$$

Here B is a small constant to account for background signals, i counts the spectral contributions associated with the individual chlorosome, Θ is the polarization angle of the incident light with respect to a laboratory frame, and φ_i represents the angle of the projection of the transition dipole vector of the respective spectral component onto the sample plane with respect to some arbitrary reference axis. Finally, A_i give the amplitudes of the spectral bands. The latter is assumed to have a Gaussian form characterized by the energetic center position E_i and a width (full width at half-maximum (FWHM)) denoted by W_i . The Gaussian lineshape is defined by:

$$\frac{1}{S_i^2} \exp\left(-\frac{(E - E_i)^2}{2S_i^2}\right) \quad \text{with} \quad S_i = \frac{W_i}{2\sqrt{2 \ln 2}} \quad (6.2)$$

The experimental 2D polarization-resolved spectra are fitted to equation 6.1 using a standard, nonlinear fitting approach based on the least-squares method. The amplitudes $A_i(E)$ and the phase angles φ_i were treated as global parameters. The number of spectral contributions i taken into account was restricted to four, because this is the minimal

number of transitions necessary to reproduce all the features of the experimental spectra reasonably well. These considerations also resulted in consistent and physically reasonable values for the fit parameters (see below). Note that there is a total of 17 (B , $4 \cdot \varphi_i$, $4 \cdot A_i$, $4 \cdot E_i$, $4 \cdot W_i$) independent fitting parameters associated with these four spectral bands. These parameters were used in a global fitting procedure, i.e. 97-200 spectra are fitted with these parameters at once.

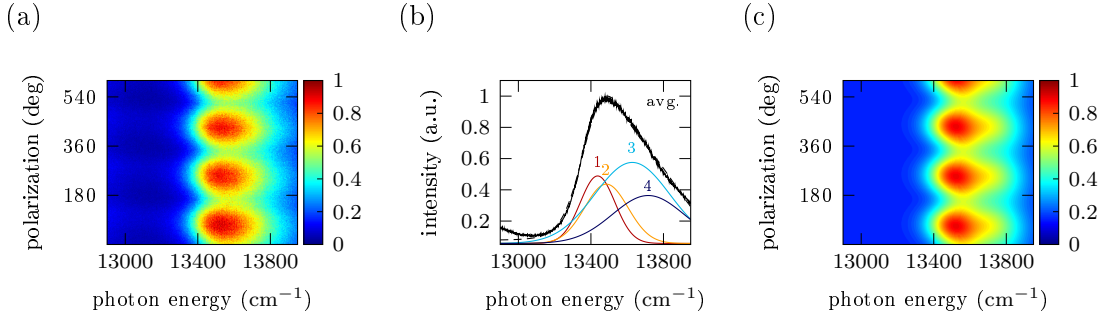


Figure 6.3: (a) Polarization-resolved fluorescence-excitation spectrum of an individual chlorosome from the *bchR* mutant (see figures 6.1 and 6.2) (b) Fluorescence-excitation spectrum of panel a averaged over all polarizations (black), together with its decomposition into four Gaussians (colored). (c) Fitted polarization-resolved fluorescence excitation spectra according to equation 6.1.

Figure 6.3b displays the decomposition of the polarization-averaged spectrum from figure 6.3a (also figure 6.2a) into four Gaussian transition bands. For future reference, these bands are labeled 1-4, in order of increasing energy. For the example in figure 6.3, this analysis revealed broad absorption bands with energy positions (FWHM) of $E_1 = 13437 \text{ cm}^{-1}$ ($W_1 = 226 \text{ cm}^{-1}$), $E_2 = 13484 \text{ cm}^{-1}$ ($W_2 = 280 \text{ cm}^{-1}$), $E_3 = 13629 \text{ cm}^{-1}$ ($W_3 = 487 \text{ cm}^{-1}$), and $E_4 = 13716 \text{ cm}^{-1}$ ($W_4 = 464 \text{ cm}^{-1}$). The mutual polarization angles between the various absorption bands, determined as $\Delta\Phi_{ij} = |\varphi_i - \varphi_j|$ if the result is less than 90° and $\Delta\Phi_{ij} = |180^\circ - |\varphi_i - \varphi_j||$ otherwise, are given by $\Delta\Phi_{12} = 79.4^\circ$, $\Delta\Phi_{13} = 4.4^\circ$, $\Delta\Phi_{14} = 80.7^\circ$, $\Delta\Phi_{23} = 83.8^\circ$, $\Delta\Phi_{24} = 1.3^\circ$, and $\Delta\Phi_{34} = 85.1^\circ$. The fitted 2D polarization spectrum for the measurement presented in figure 6.3a is shown in figure 6.3c.

Statistical analysis of the Gaussian contributions to the polarization-resolved, fluorescence-excitation spectra

This procedure was employed to analyze the polarization-resolved fluorescence-excitation spectra from 75 individual chlorosomes of the WT, 66 individual chlorosomes from the *bchR*, and 29 individual chlorosomes from the *bchQR* mutant from *Cba. tepidum*. 72 out of the 75 spectra from the WT, 58 out of 66 from the *bchR* mutant, and all of the spectra

from the *bchQR* mutant could be decomposed into four spectral contributions similar to the example given in figure 6.3. The remaining spectra could not be analyzed in this way, and they were not considered for further analysis. The decomposed spectra of all the examples given in figure 6.1 can be found in the appendix A.1. The histograms in figure 6.4 display the statistics of the energetic positions (a,c,e) and the widths (b,d,f) of the four bands for the analyzed chlorosomes. It is important to note that a single chlorosome corresponds to a small subensemble of molecular aggregates. Hence, each entry in the histograms represents an average over such a subensemble, whereas the whole histogram represents the distribution of these averages within the macroscopic ensemble of chlorosomes. The histograms presented in figure 6.4 can be characterized by the statistical parameters summarized in table 6.1.

Table 6.1: Mean values (standard deviations) of the spectral positions E_i and linewidths W_i (FWHM) of the Gaussians obtained from sets of 72, 58, and 29 individual chlorosomes of the WT, the *bchR*, and the *bchQR* strains.

strain	WT	<i>bchR</i>	<i>bchQR</i>
$E_{\text{peak,overall}}$ (cm^{-1})	13366(97)	13609(33)	13492(21)
W_{overall} (cm^{-1})	783(91)	437(54)	441(70)
E_1 (cm^{-1})	13170(56)	13468(26)	13452(18)
W_1 (cm^{-1})	310(86)	233(35)	198(25)
E_2 (cm^{-1})	13274(59)	13502(41)	13471(21)
W_2 (cm^{-1})	432(76)	270(41)	230(28)
E_3 (cm^{-1})	13517(80)	13685(39)	13656(40)
W_3 (cm^{-1})	685(109)	495(66)	404(31)
E_4 (cm^{-1})	13649(91)	13747(52)	13695(45)
W_4 (cm^{-1})	701(98)	501(63)	408(27)

The distribution of the peak positions of the overall (polarization averaged) spectra, shown in the first two rows of table 6.1, are characterized by a mean of $E = 13\,366\text{ cm}^{-1}$ for the WT chlorosomes and a width (standard deviation) of 97 cm^{-1} , which is about a factor of 3 to 4 larger than the 33 cm^{-1} that have been found for the width of the corresponding distribution of the *bchR* chlorosome sample and the 21 cm^{-1} of the *bchQR* chlorosome sample. This indicates a more homogeneous overall absorption band for the chlorosomes of the *bchR* mutant and the *bchQR* mutant, which is also reflected in the statistics of the underlying spectral contributions, revealing narrow distributions for the energy positions and FWHMs as summarized in table 6.1. The reduction of sample heterogeneity is reflected by the decrease of the FWHM of the absorption band, which arises from the Q_y transition of the aggregated BChls, from 783 cm^{-1} for the WT to 437 cm^{-1} for the *bchR* mutant and 441 cm^{-1} for the *bchQR* mutant.

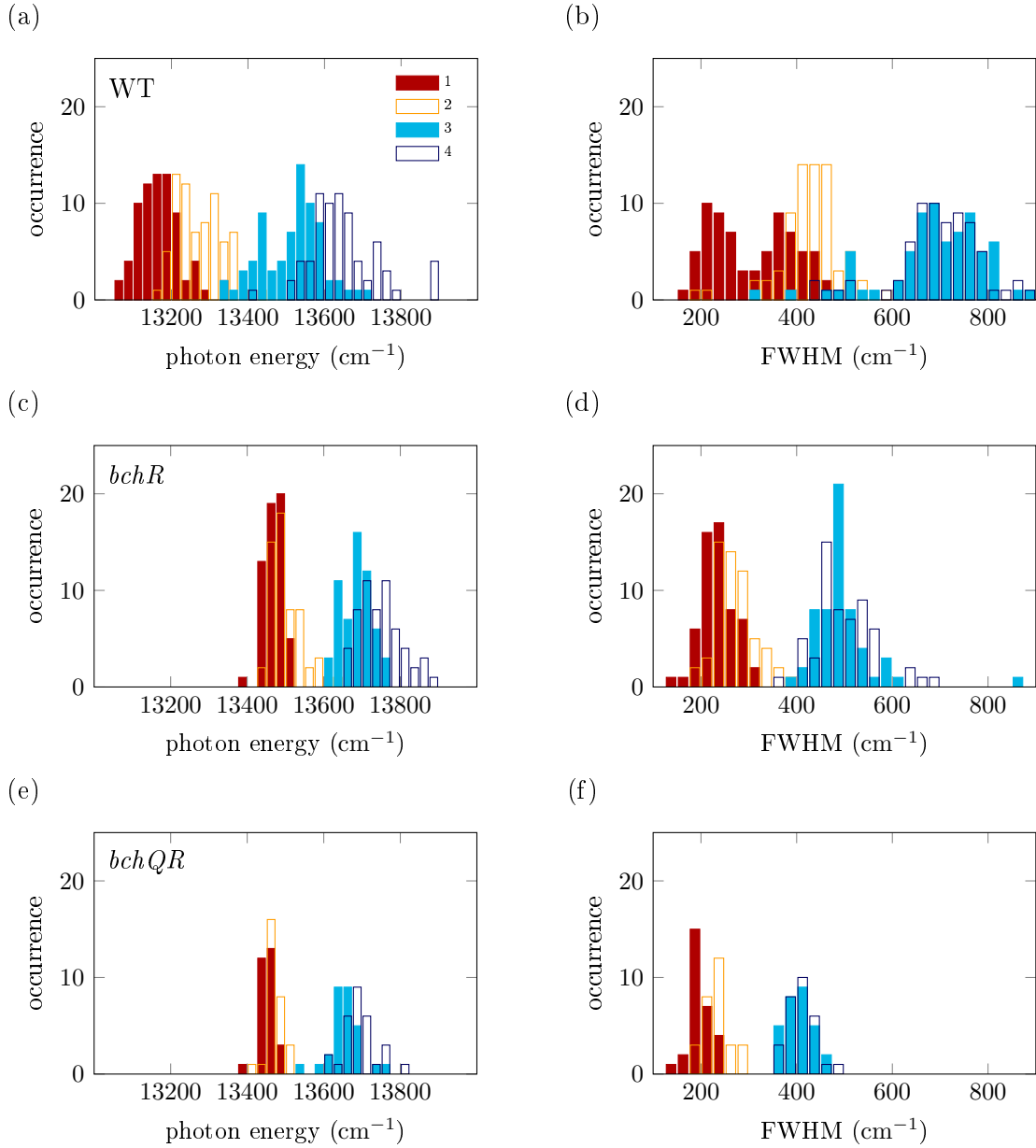


Figure 6.4: Top: WT; Center: *bchR* mutant; Bottom: *bchQR* mutant. (a,c,e) Distributions of the spectral peak positions of the fitted Gaussians and (b,d,f) distributions of the widths (FWHM) of the fitted Gaussians.

For the WT chlorosomes, the widths of 310 cm^{-1} and 432 cm^{-1} of the two spectral components E_1 and E_2 are significantly narrower than the 685 cm^{-1} and 701 cm^{-1} values that have been found for the spectral components E_3 and E_4 . The same holds true for the spectral components of the *bchR* mutant (233 cm^{-1} and 270 cm^{-1} vs 495 cm^{-1} and 501 cm^{-1}) and for those from the *bchQR* mutant (198 cm^{-1} and 230 cm^{-1} vs 404 cm^{-1} and 408 cm^{-1}). The statistics clearly show that there are two pairs of spectral components

energetically close to each other, one in the low-energy part of the spectrum and another one in the high-energy part of the spectrum. In the following analysis, the four spectral components are grouped into a low-energy pair, E_1 and E_2 , and a high-energy pair, E_3 and E_4 . These pairs of two transitions will be referred to as the low-energy doublet and the high-energy doublet. Moreover, from the FWHM distributions, it follows that high-energy doublet transitions are broader than the low-energy components. The width of the transitions are caused by inhomogeneous line broadening.

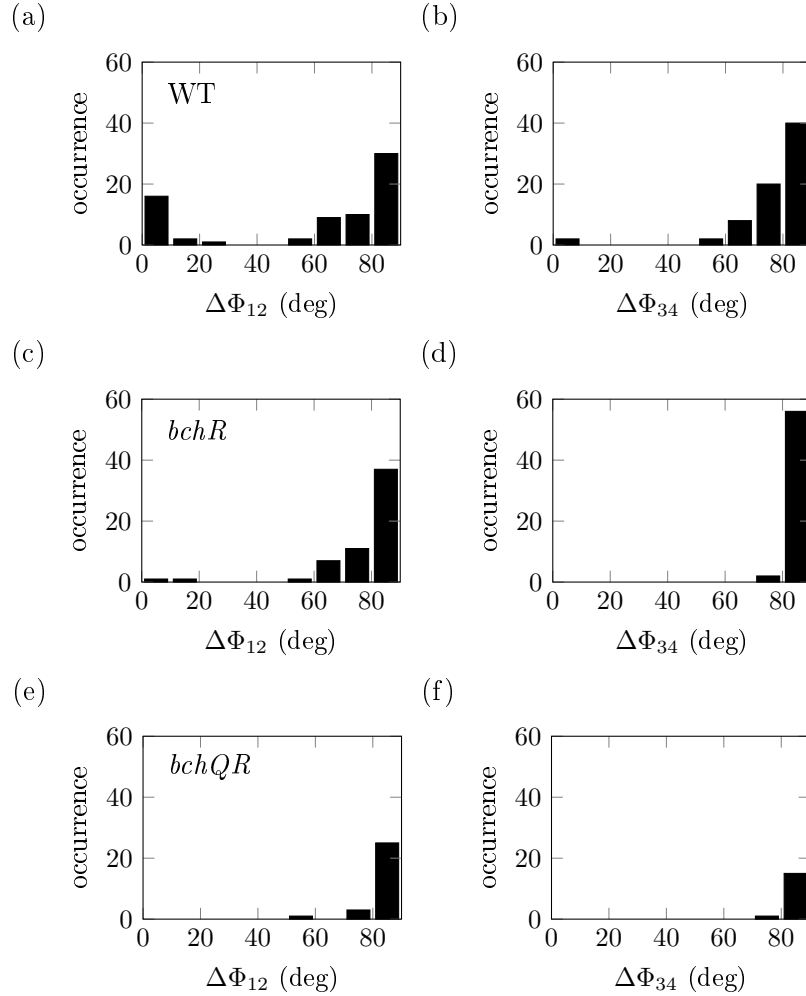


Figure 6.5: Distributions of the relative phase angles $\Delta\Phi$ between the bands 1 and 2 and between the bands 3 and 4 for chlorosomes from (a,b) the WT, (c,d) the *bchR* mutant, and (e,f) the *bchQR* mutant.

The information about the polarization angles of the bands is analyzed to obtain more information about the arrangement of the transition dipole moments of the electronic states. The difference of the polarization angles, $\Delta\Phi_{12}$ and $\Delta\Phi_{34}$, between the transitions within one pair are determined for each individual chlorosome. The distributions of $\Delta\Phi_{12}$ and $\Delta\Phi_{34}$ for the WT, the *bchR* mutant and the *bchQR* mutant are presented in figure

6.5, whereas the mean values and standard deviations are given in table 6.2.

For the WT sample, the differences in phase angles between bands 1 and 2 form a bimodal distribution peaking around 0° and 90° , which is averaged out to the values of $(60 \pm 34)^\circ$ for the mean and the standard deviation. This illustrates the added value of single-molecule techniques, which allow one to obtain information about the distributions of parameters rather than only about their average values.

In contrast, the two spectral components in the low- and high-energy doublets for the *bchR* chlorosomes and the *bchQR* chlorosomes are strongly perpendicularly polarized to each other, as demonstrated by the narrowness of the distributions for $\Delta\Phi_{12}$ and $\Delta\Phi_{34}$. This holds true for the distributions of $\Delta\Phi_{34}$ for the WT chlorosomes. The distributions of $\Delta\Phi_{ij}$ for the WT and the mutants are presented in the appendix, figures A.4, A.5, A.6. The mean values and standard deviations are given in table A.1.

Table 6.2: Mean values (standard deviations) of the relative phase angles between the bands 1 and 2 and between the bands 3 and 4 for the three types of chlorosomes.

ij	12			34		
	WT	<i>bchR</i>	<i>bchQR</i>	WT	<i>bchR</i>	<i>bchQR</i>
$\Delta\Phi_{ij}$ (deg)	60(34)	78(16)	83(6)	77(16)	87(3)	88(3)

The observed perpendicular polarization properties of the spectra of the mutants and a part of the spectra of the WT are consistent with an underlying circular symmetry for the overall BChl arrangement within an aggregate [75, 77, 79, 88]. Nevertheless, previous to further evaluation of the data with regard to a cylindrical symmetry, the partly deviating polarization behavior for the WT chlorosomes must be discussed.

6.3 Polarization properties of the spectra of individual chlorosomes from the wild type

For the chlorosomes from the *bchR* mutant and the *bchQR* mutant, the phase differences between the bands within the low-energy pair and the high-energy pair, $\Delta\Phi_{12}$ and $\Delta\Phi_{34}$, mostly occur at 90° (see figure 6.5). For the chlorosomes from the WT, this observation is not that straightforward. Here, the phase differences between the bands in the high-energy pair, $\Delta\Phi_{34}$, also accumulate at 90° , whereas those between the low-energy pair, $\Delta\Phi_{12}$, show a bimodal distribution peaking at 0° and at 90° .

To analyze this observation in more detail, figure 6.6 displays the correlation between the phase differences $\Delta\Phi_{12}$ and $\Delta\Phi_{13}$ for the WT, the *bchR* mutant and the *bchQR* mutant. The data points can be divided roughly into two groups, namely, those that exhibit hardly any correlation between $\Delta\Phi_{12}$ and $\Delta\Phi_{13}$ (group 1; grey shaded area in figure 6.6) and those that do exhibit strong correlation (group 2). Group 1 includes all

chlorosomes of the *bchQR* mutant, 56 chlorosomes from the *bchR* mutant (97%) and 53 chlorosomes from the WT (74%). For the chlorosomes of group 1, the data points cluster around $\Delta\Phi_{12} \approx 70^\circ - 90^\circ$ ($1\perp 2$), and the spectra feature approximately two mutually orthogonally polarized bands within each pair (in short: $1\perp 2$ and $3\perp 4$) and in addition two predominantly parallel-polarized pairs of bands $1\parallel 3$ and $2\parallel 4$. Group 2 includes exclusively the remaining 26% of the WT chlorosomes, and 3% of the *bchR* mutant chlorosomes studied. Here, it is found $\Delta\Phi_{13} \approx 65^\circ - 90^\circ$ ($1\perp 3$) and $\Delta\Phi_{12} \leq 30^\circ$ ($1\parallel 2$). For this group of chlorosomes, the analysis of the polarization behavior of the spectral bands yields approximately $1\parallel 2$, $3\perp 4$, and $1\perp 3$ (implying $1\parallel 4$, $2\perp 3$, and $2\parallel 4$).

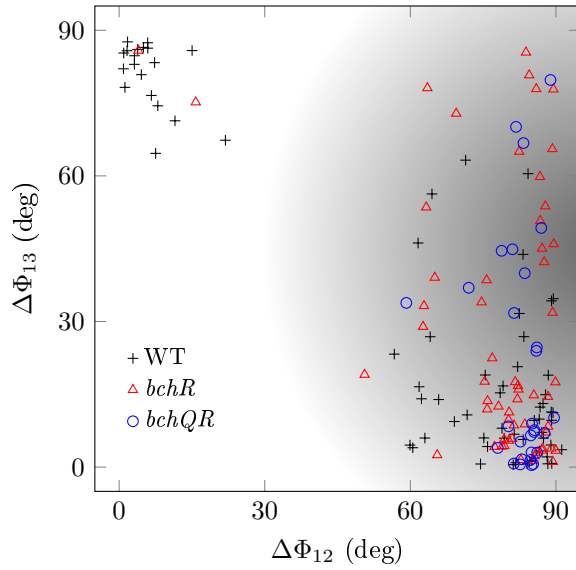


Figure 6.6: Correlation between the phase differences between the bands within the low-energy pair, $\Delta\Phi_{12}$, and the bands 1 and 3, $\Delta\Phi_{13}$, for individual chlorosomes from the WT (crosses), the *bchR* mutant (red triangles), and from the *bchQR* mutant (blue circles). The shaded area indicates those chlorosomes that are referred to as WT-group1 in the text.

In the following, it will be referred to the WT chlorosomes in the two groups as WT-group1 and WT-group2, respectively. The distributions of the relative phase angles $\Delta\Phi_{ij}$ from the chlorosomes of WT-group1 and WT-group2 are displayed separately in figures A.7 and A.8. The mean values and standard deviations are given in table A.1. The chlorosomes from the *bchR* mutant are still assigned to one group since only a minority of two of the chlorosomes show a different polarization behavior. As an assignment of a structure to the chlorosomes of WT-group2 is not that obvious as to the chlorosomes of WT-group1, the *bchR* mutant, and the *bchQR* mutant, the chlorosomes of WT-group2 are not considered for the following analysis.

6.4 Orientation of the transition dipole moments of BCHs in cylindrical structures

The statistics (see table 6.1) clearly showed that there are two pairs of spectral components energetically close to each other. For the WT-group1 chlorosomes, now, the distributions for the energetic separations, ΔE_{12} and ΔE_{34} are given in figure 6.7, together with the corresponding distributions for the *bchR* mutant, and the *bchQR* mutant.

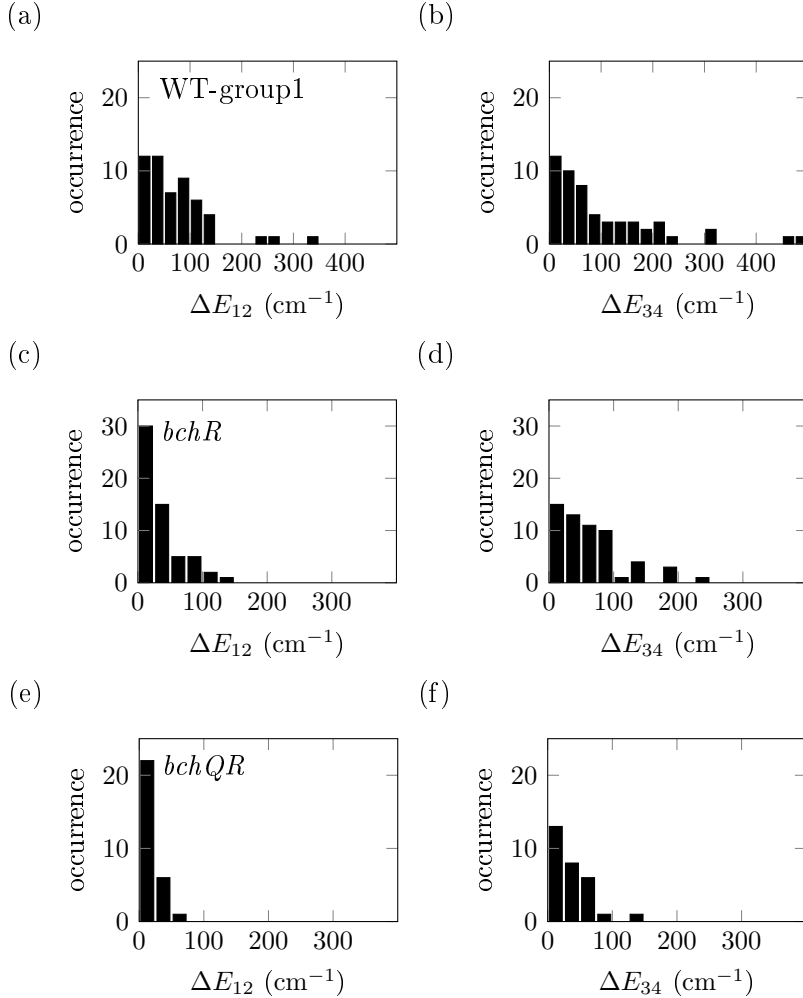


Figure 6.7: Distributions of the energetic separation between the low-energy bands ΔE_{12} and the high-energy bands ΔE_{34} for an individual chlorosome of (a,b) the WT-group1, (c,d) the *bchR* mutant and (e,f) the *bchQR* mutant.

For the WT-group1 chlorosomes, the distributions for the energetic separations of the spectral components in the low- and high-energy pairs are rather wide with respect to those from the *bchR* mutant and the *bchQR* mutant that generally are separated by less than 100 cm^{-1} . The same holds true for the widths of the mutual phase differences (see figures 6.5 and 6.8). The widths of the distributions for the mutants are clearly narrower

than those of the corresponding distributions for the WT-group1 chlorosomes. This is clearly reflected by the corresponding standard deviations (see table 6.3), which decrease in the order WT-group1, *bchR* (single mutation), *bchQR* (double mutation).

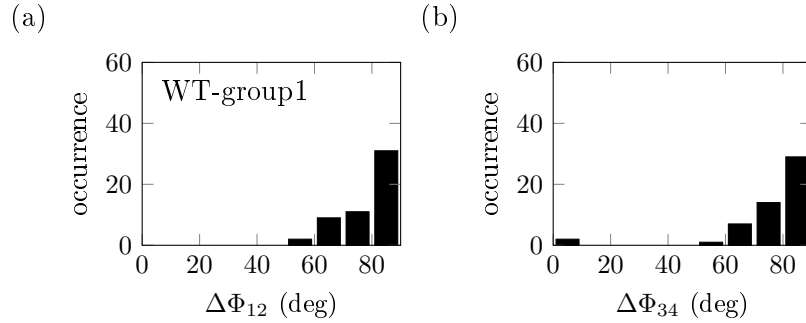


Figure 6.8: Distributions of the relative phase angles $\Delta\Phi_{12}$ and $\Delta\Phi_{34}$ of the chlorosomes from WT-group1.

The chlorosomes from the *bchQR* mutant, the *bchR* mutant as well as those assigned to WT-group1 exhibit the typical polarization behavior that is associated with molecular aggregates with an underlying tubular arrangement of the BChls [75, 77, 79]. Briefly, for an ideal and sufficiently long molecular aggregate of cylindrical symmetry, that is, exhibiting neither structural nor energetic disorder, the electronic coupling between the monomers gives rise to only three exciton states with a nonzero transition dipole moment for transitions from and to the electronic ground state (see section 4.3). The transition dipole moment of the lowest exciton state, μ_{\parallel} , is oriented parallel to the symmetry axis of the cylinder. In contrast, the other two transition dipole moments result from a pair of degenerate exciton states with mutually orthogonal transition dipole moments, $\mu_{\perp x}$ and $\mu_{\perp y}$, both oriented perpendicularly with respect to the symmetry axis of the tube (see figure 6.9).

Table 6.3: Mean values (standard deviations) of the energetic separations and relative phase angles between the bands 1 and 2 and between the bands 3 and 4 for the three types of chlorosomes (WT-group1, *bchR*, *bchQR*).

ij	12			34		
	WT-group1	<i>bchR</i>	<i>bchQR</i>	WT-group1	<i>bchR</i>	<i>bchQR</i>
ΔE_{ij} (cm ⁻¹)	71(66)	34(31)	19(13)	101(107)	62(53)	38(32)
$\Delta\Phi_{ij}$ (deg)	79(10)	78(16)	83(6)	76(17)	87(3)	88(3)

Together with the information that the chlorosomes are oriented with their long axis parallel to the surface of the substrate [59] and that for (the vast majority of) the molecular aggregates the long axes of the secondary structures within a chlorosome are oriented parallel with respect to each other [1, 56, 91], this leads to a clear interpretation of bands

1-4 found in the analyses for the WT-group1, the *bchR* mutant, and the *bchQR* mutant chlorosomes. Bands 1 and 2 result from pairs of exciton states with transition dipoles parallel and perpendicular, respectively, to the axes of the cylindrical aggregates that make up the chlorosomes. Bands 3 and 4 derive from similar pairs with higher energies.

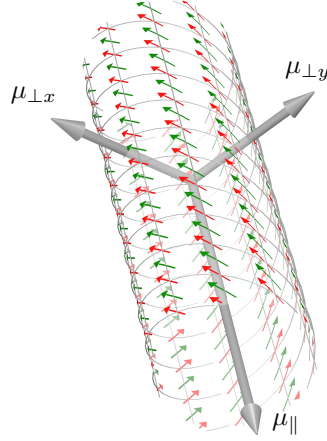


Figure 6.9: Molecular aggregate with cylindrical symmetry. Electronic coupling yields three exciton states with dipole-allowed transitions to the electronic ground state. The corresponding transition dipole moments are oriented parallel to the symmetry axis (μ_{\parallel}) and mutually orthogonal ($\mu_{\perp x}$, $\mu_{\perp y}$) with respect to that axis.

The widths of the various distributions in figures 6.1 and 6.5 reflect small variations in the arrangements and (or) the microscopic disorder realizations of the light-harvesting aggregates in individual chlorosomes, as will be demonstrated below. The distributions for the mutual polarization angles between transitions in the low-energy doublet and transitions in the high-energy doublet ($\Delta\Phi_{13}$, $\Delta\Phi_{14}$, $\Delta\Phi_{23}$, $\Delta\Phi_{24}$; see table A.1) are broader than those for $\Delta\Phi_{12}$ and $\Delta\Phi_{34}$, although there still seems to be some preference for parallel or perpendicular orientations. A likely explanation for this is that the low- and high-energy doublets originate from different cylindrical arrangements that either are not aligned perfectly parallel to each other or have different disorder characteristics. In principle, structural models that contain two molecules per unit cell also can give rise to four optical peaks in total, two of which are parallel and two (2-fold degenerate ones) that are perpendicular to the cylinder axis. In that case, it is expected that the distributions of the mutual angles between the various transitions are all very similar, which is in contrast to the data displayed in figure 6.5 (also see figures A.1, A.2, A.3). Hence, on the basis of the statistics presented, transitions 1-4 likely do not all belong to the same cylinder. The low-energy doublet, consisting of transitions 1 and 2, arises from one type of tubular structure, while transitions 3 and 4, which form the high-energy doublet, are associated with a slightly different tubular arrangement.

The abovementioned interpretation yields a direct relationship between the oscillator strength of the parallel and perpendicular polarized exciton transitions and the angle β between the transition dipole moments of the monomers and the symmetry axis of the cylinder (see section 4.3 and reference [75]).

$$\beta = \arctan \sqrt{\frac{2O_{\perp}}{O_{\parallel}}} \quad (6.3)$$

Here the additional factor of 2 accounts for the fact that the polarization-resolved measurements are on average sensitive to only half of the perpendicular oscillator strength, because it is known that the chlorosomes are oriented with their long axis parallel to the surface of the substrate [59].

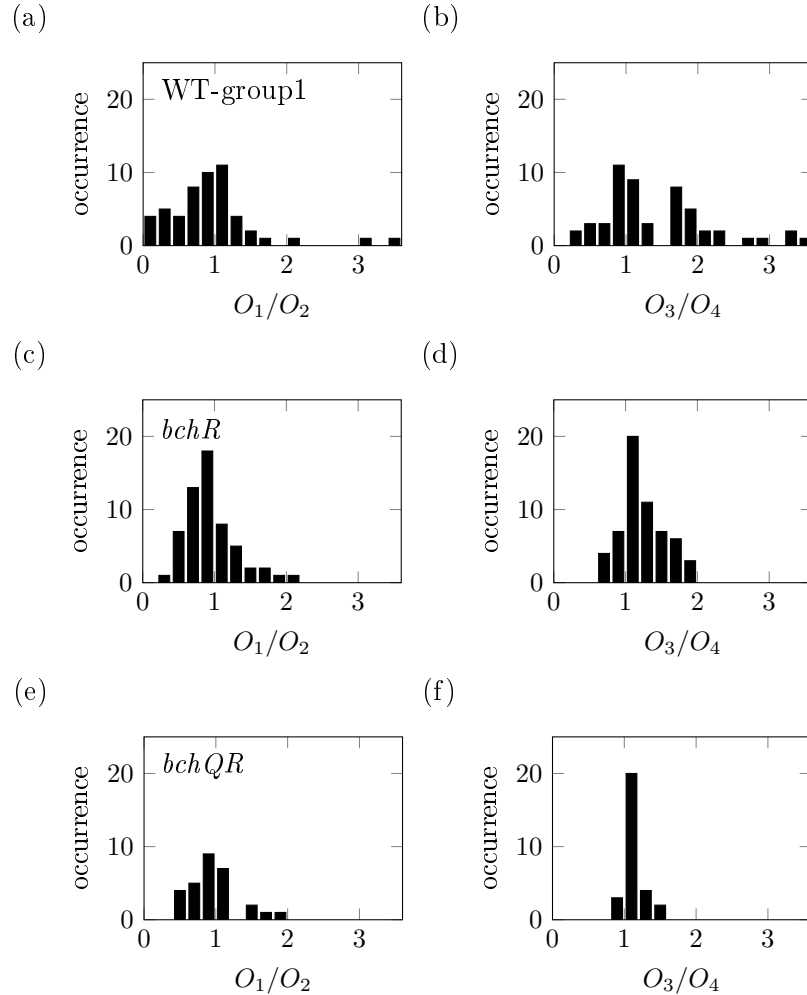


Figure 6.10: Distributions of the ratio of the oscillator strength between bands 1 and 2 and between bands 3 and 4 for an individual chlorosome of (a,b) the WT-group1, (c,d) the *bchR* mutant and (e,f) the *bchQR* mutant.

The distributions of the ratios of the oscillator strength of the low- and high-energy

doublet, O_1/O_2 and O_3/O_4 are given in figure 6.10 for the WT-group1 chlorosomes, together with the corresponding distributions for the $bchR$ mutant, and the $bchQR$ mutant. For the WT-group1 chlorosomes, the distributions for the ratios of the oscillator strengths of the spectral components in the low and high-energy pairs are rather wide with respect to those from the $bchR$ mutant, and the $bchQR$ mutant. This is also reflected by the corresponding standard deviations (see table 6.4).

Table 6.4: Mean values (standard deviations) of the ratios of the oscillator strengths between the bands 1 and 2 and between the bands 3 and 4 for the three types of chlorosomes (WT-group1, $bchR$, $bchQR$).

ij	12			34		
	WT-group1	$bchR$	$bchQR$	WT-group1	$bchR$	$bchQR$
O_i/O_j	1.04(0.95)	0.95(0.35)	0.95(0.34)	1.42(0.77)	1.24(0.30)	1.13(0.13)

Denoting the monomer dipole angles thus derived from the low-energy and the high-energy pair as β_{12} and β_{34} , respectively, and using the data for the oscillator strengths, the distributions of these angles as shown in figure 6.11a for the WT-group1, in figure 6.11b for the $bchR$ mutant and in figure 6.11c for the $bchQR$ mutant are obtained. The mean values and standard deviations of these histograms are given in table 6.5. Again, the widths of the distributions decrease in the order WT-group1, $bchR$ mutant, $bchQR$ mutant, which suggests that the structures of the molecular aggregates within the chlorosomes are better defined when the homolog variation due to the BChl side groups is more restricted. Yet, within statistical accuracy, all distributions are centered around a similar mean of about 56° for β_{12} and 52° for β_{34} . The differences in the values for dipole angles β_{12} and β_{34} suggests that tubes responsible for the low and high energy doublet transitions indeed have slightly different structural arrangements.

Table 6.5: Mean values (standard deviations) of the distributions of the molecular dipole angles β_{12} (low-energy doublet) and β_{34} (high-energy doublet) obtained from the spectral analyses

	WT-group1	$bchR$	$bchQR$
β_{12} (deg)	57.3(9.6)	56(4.7)	56.1(4.5)
β_{34} (deg)	51.7(7.4)	52(3.4)	53.1(1.6)

The calculation of β is based on the assumption that the chlorosome represents an ensemble of cylindrical structures, aligned parallel to each other. Nevertheless, for the $bchQR$ chlorosomes, in some cases, the cryo-EM images revealed secondary cylinder-like structures, whose symmetry axes were oriented mutually orthogonal with respect to each other. Therefore, the influence of a fraction of “misaligned” tubular structures on the determination of β is modeled in the appendix, chapter B. The calculations show that

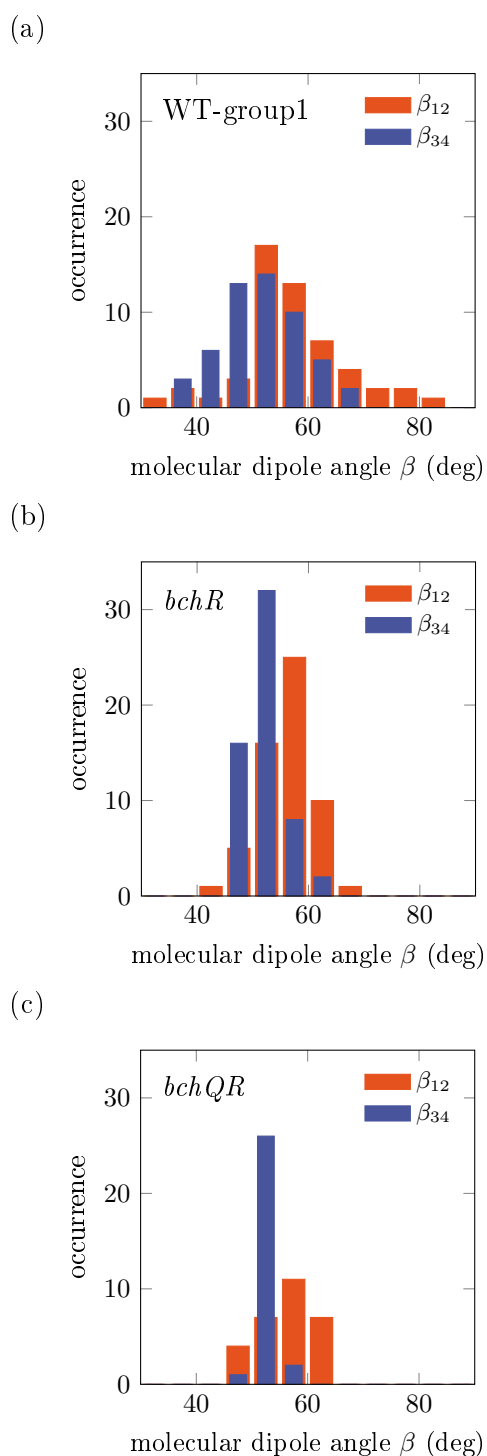


Figure 6.11: Distributions of the angles β_{12} (low-energy pair) and β_{34} (high-energy pair) that are enclosed between the transition dipole moments of the monomers and the symmetry axis of the cylinder for (a) the WT-group1, (b) the *bchR* mutant, and (c) the *bchQR* mutant.

the variation of β amounts to a few degrees depending on the fraction of “misaligned” structures. Nevertheless, it cannot be excluded that the “misaligned” secondary structures contribute to a small extent also to the widths of the distributions shown in figure 6.11.

6.5 Reconstruction of LD spectra from the polarization-resolved spectra

In previous studies [58, 92], LD spectroscopy was used to study polarization-dependent features of optical spectra rather than polarization-resolved spectroscopy. Polarization-resolved spectroscopy provides spectra with almost any polarization relative to the orientation of individual chlorosomes (see figure 6.1), as these spectra were obtained by rotating the polarization by a few degrees between two successive scans of the spectrum. Therefore, LD spectra can be reconstructed from polarization-resolved spectra. It should be noted that these LD spectra emerge from fluorescence-excitation spectra rather than absorption spectra, which are commonly used in LD spectroscopy. For the chlorosomes studied, the fluorescence-excitation spectrum is directly proportional to the absorption spectrum [4]. Therefore, the spectra taken for the calculation of the LD spectra are denoted with $A(E)$.

In reference [92], it was found that the maxima of the modulation shown in figure 6.2c, at an angle Φ_{\parallel} , can be associated with the transition dipole moment along the long axis of the secondary, cylindrical structures in chlorosomes (see section 4.3). According to the definition used in these publications, the angle $\Phi_{\parallel 1}$ (the angle of the first maximum of the modulation shown in figure 6.2c) corresponds to a polarization of the excitation light parallel to the long axis of the chlorosome with respect to a laboratory frame. Therefore, the fluorescence-excitation spectrum at this polarization is defined as $A_{\parallel}(E)$ (where E denotes the photon energy of the excitation light). The fluorescence-excitation spectrum $A_{\perp}(E)$ occurs at an angle $\Phi_{\perp 1} = \Phi_{\parallel 1} \pm 90^\circ$ of the polarization of the excitation light. The angle $\Phi_{\perp 1}$ is equivalent to the first minimum of the fit presented in figure 6.2c.

The LD spectrum of an individual chlorosome is then reconstructed by subtracting the fluorescence-excitation spectrum for the excitation with light that is parallel to the long axis from the one with light that is perpendicular to it:

$$LD(E) = A_{\parallel}(E) - A_{\perp}(E) \quad (6.4)$$

The spectra $A_{\parallel}(E)$ and $A_{\perp}(E)$ are averages over all polarizations $\Phi_{\parallel} = \Phi_{\parallel 1} + n \cdot 180^\circ$ ($\Phi_{\perp} = \Phi_{\perp 1} + n \cdot 180^\circ$) that occur in the polarization-resolved spectrum. Figure 6.12 presents four LD spectra of individual chlorosomes from the WT, the *bchR* mutant and the *bchQR* mutant, respectively.

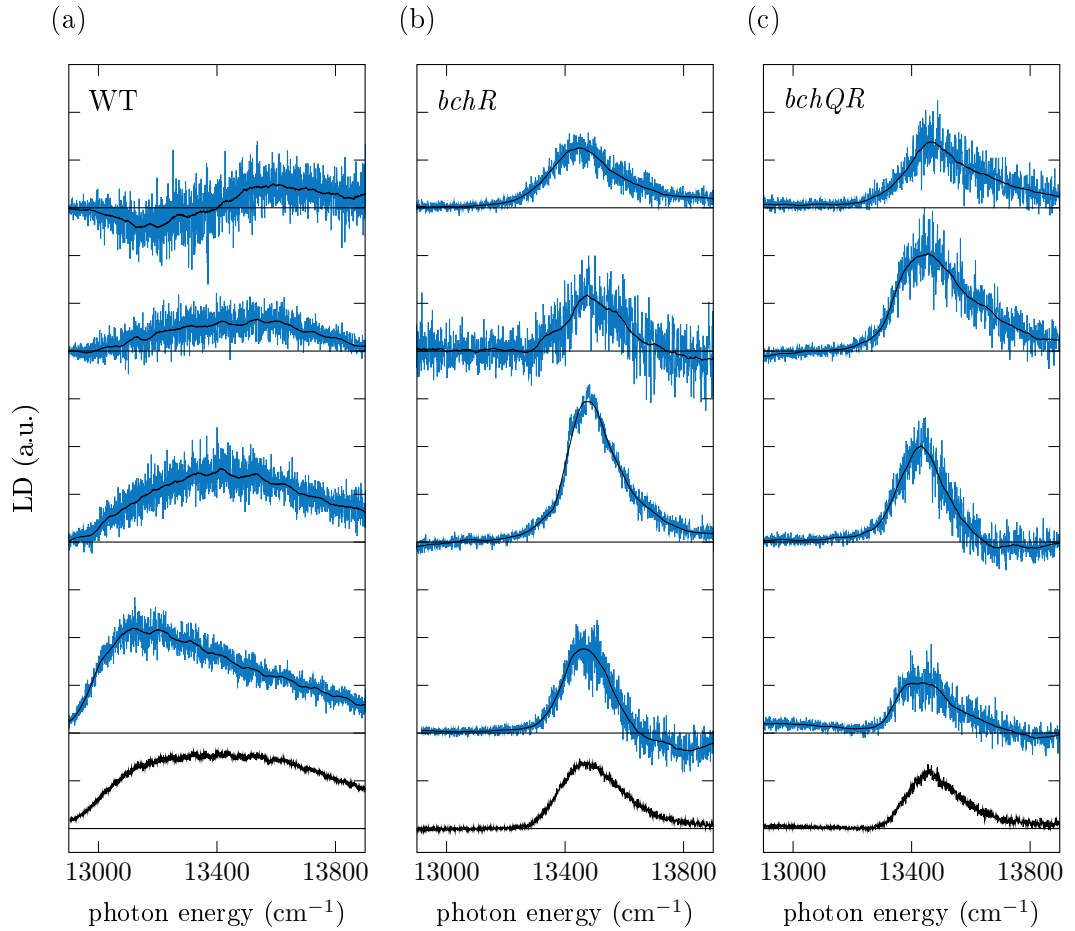


Figure 6.12: Four representative LD spectra of individual chlorosomes (mid blue) from (a) the WT, (b) the *bchR* mutant, and (c) the *bchQR* mutant, respectively, are shown. The spectra were reconstructed from polarization-resolved fluorescence-excitation measurements. The black line represents a spline fit of the data and serves as a guide for the eye. The spectra are offset along the vertical axis for clarity. At the bottom of the figure, the average of 72 LD spectra of individual chlorosomes from the WT, 66 spectra of the *bchR* mutant, and 29 spectra of the *bchQR* mutant is shown in black. The horizontal black line corresponds to the zero line of each spectrum.

The spectra are reconstructed from the normalized polarization-resolved fluorescence-excitation spectra. The black curve represents the filtered data and serves as a guide for the eye to identify positive and negative bands. Some of the LD spectra feature one positive band, whereas others feature two bands. The LD spectra of the chlorosomes from the *bchR* mutant and the *bchQR* mutant exhibit a positive band at lower energies and a negative band at higher energies, whereas the sequence of positive and negative bands is the other way around for the chlorosomes of the WT. In total, 68 spectra from individual chlorosomes of the WT, 50 spectra of the *bchR* mutant chlorosomes, and 22 spectra of the *bchQR* mutant chlorosomes feature one band. The remaining 4 spectra of the WT, 16 of the *bchR* mutant, and 7 of *bchQR* mutant feature two bands. It can also

be noted that, in the spectra of the *bchR* mutant and the *bchQR* mutant, the intensity of the positive band is significantly higher than the intensity of the negative band.

The positive band of all spectra of the chlorosomes of the *bchR* mutant and the *bchQR* mutant is roughly located around $13\,450\text{ cm}^{-1}$. The measurements on chlorosomes from the WT show a substantial variation in the position of the positive band. Again, this represents the structural, and therefore spectral, heterogeneity in the WT chlorosomes.

Besides the LD spectra of individual chlorosomes, figure 6.12 displays the average of the LD spectra from individual chlorosomes at the bottom, which corresponds to an ensemble spectrum. It can easily be seen that the ensemble spectrum only features one positive band, whereas some of the individual spectra feature two bands. In the ensemble spectrum, the negative band vanishes as only a minority of the spectra show a negative band with low intensity.

Usually, the precise measurement of an ensemble LD spectrum depends on the perfect alignment of the sample. The measurement of the presented LD ensemble spectra of chlorosomes was realized with the single chlorosome technique. As an individual chlorosome is per se oriented, as described above, the combination of their LD spectra to an ensemble spectrum represents the spectrum of a perfectly aligned sample of chlorosomes. Unlike other techniques of sample orientation, e.g., gel compression or orientation in electric fields [42, 93–95], this method leaves no room for deviation in the orientation of the chlorosomes. A misalignment of the chlorosome sample yields the same spectrum, yet the LD spectrum shows lower signal strength. Details on the effect of misalignment of the sample on the LD spectra can be found in section B.2.

The polarization features of the LD spectra are often used to obtain information about the orientation of the transition dipole moments in the sample. In principle, it is possible to calculate the angle of the molecular transition dipole moment with respect to the cylinder axis β also from the LD spectra (see section 4.3). For such an analysis, however, LD measurements on individual cylinders or a perfectly oriented sample are necessary. Therefore, the exact determination of β from LD spectra for cylindrical aggregates relies strongly on the proper alignment of the sample. For the misalignment of the cylinders with respect to each other, this method overestimates β [75]. The chlorosome represents an ensemble of cylindrical structures. Due to structural variations, the cylindrical structures are not perfectly parallel aligned with respect to each other. Therefore, it is not possible to obtain information about the angle β in chlorosomes from the LD spectra. This illustrates the added value of the polarization-resolved measurements since it was possible to determine the angle β from the spectra of individual chlorosomes using global analysis.

Furthermore, the LD spectra do not yield sufficient information to explain the differences between the spectra of individual chlorosomes. However, as the LD spectra were reconstructed from polarization-resolved measurements, the full information of these

measurements can be used to explain the LD spectra of individual chlorosomes. In figure 6.13a,b the averaged fluorescence-excitation spectra of individual chlorosomes from the *bchR* mutant and their Gaussian transition bands are shown. Below, in panel c,d the corresponding LD spectra are shown. Similar to the spectra presented in figure 6.12b, the spectrum in figure 6.13c features a positive, asymmetric band, whereas the LD spectrum of the chlorosome in figure 6.13d shows a positive and a negative band.

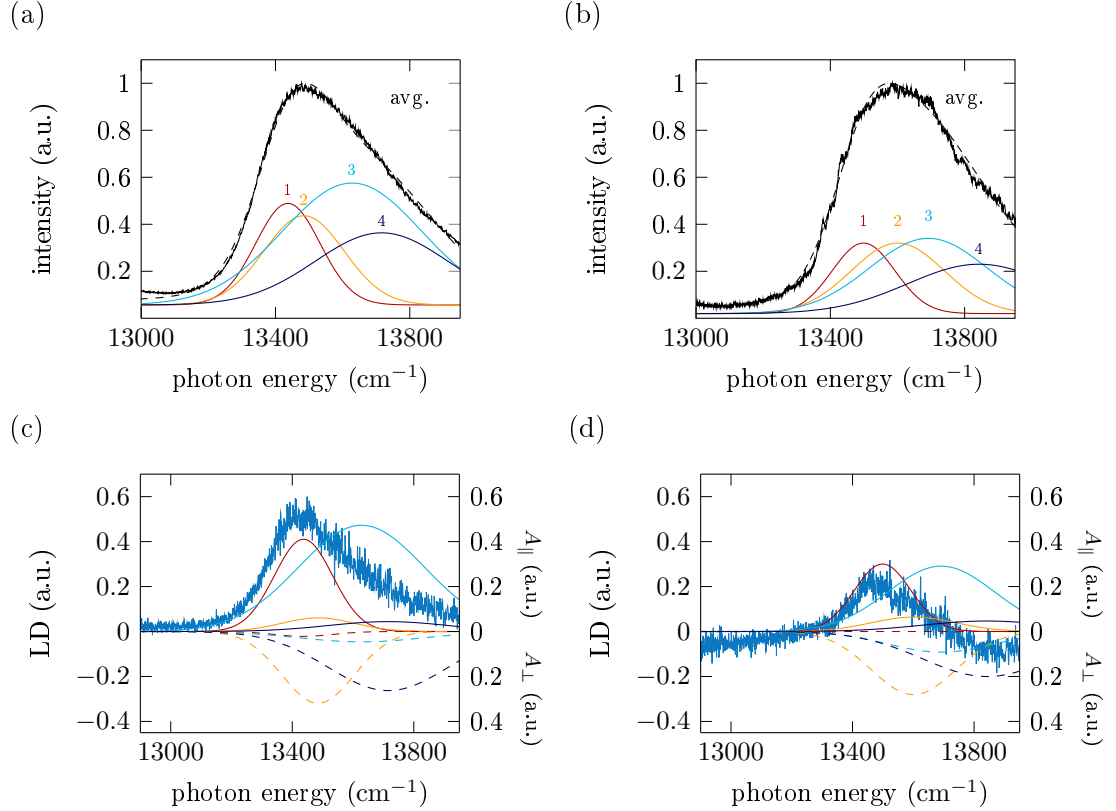


Figure 6.13: (a,b) Fluorescence-excitation spectrum of an individual chlorosome (black) together with its decomposition into four Gaussians (colored). Panel a was already shown in figure 6.2b. (c,d) LD spectra (mid blue) of the chlorosomes presented in a,b. The parallel and perpendicular orientation of the chlorosomes were determined by the maxima and minima of the fluorescence modulation presented in figure 6.2c. The gaussian contributions to the polarization resolved spectra are shown in yellow, red, cyan and dark blue. In panels c and d the contributions of the gaussians to the parallel spectrum are plotted to the positive axis of the spectrum, whereas contributions to the perpendicular spectrum are plotted to the negative axis of the spectrum.

One way to obtain an insight into the composition of the LD spectra of individual chlorosomes is the analysis of the spectral contributions in figures 6.13a,b. Therefore in figures 6.13c,d, the spectral contributions (red, yellow, cyan, dark blue) to the parallel absorption (Gaussian transition bands at the angle $\Phi_{\parallel 1}$) of the LD spectrum are plotted to the positive axis in the spectrum, whereas the spectral contributions to the perpendicular

absorption (Gaussian transition bands at the angle $\Phi_{\perp 1}$) are plotted to the negative axis of the graph. The analysis of the angles between spectral contributions (see section 6.2) showed that these transition bands are polarized more or less perpendicular to each other. Accordingly, the parallel and the perpendicular part of the spectrum (presented in the LD spectrum), consists mainly of two spectral contributions each. Contributions 1 and 3 give rise to $A_{\parallel}(\omega)$ whereas contributions 2 and 4 form $A_{\perp}(\omega)$. There are small contributions from bands 1 and 3 to $A_{\perp}(\omega)$ and bands 2 and 4 to $A_{\parallel}(\omega)$. This results from the fact that the gauss transition bands are not perfectly perpendicular to each other. The angles $\Phi_{\parallel 1}$ and $\Phi_{\perp 1}$ are determined from the entire spectrum. Therefore, the polarization maxima and minima of the individual spectral contributions might deviate from these angles as the angle ϕ_i was treated as a free parameter in the fit of the Gaussian contributions (equation 6.1). The LD spectrum results from the differences between the parallel and the perpendicular contributions to the spectrum (see equation 6.4). Taking the individual spectral contributions from the decomposed spectrum, the LD spectrum can be written as:

$$LD(E) = \sum_{i=1}^4 G_i^{\parallel} - \sum_{i=1}^4 G_i^{\perp} \quad (6.5)$$

G_i^{\parallel} denotes the individual contributions ($i = 1, \dots, 4$) to the parallel part of the spectrum and G_i^{\perp} the individual contributions to the perpendicular part of the spectrum. The individual contributions G_i^{\parallel} (G_i^{\perp}) result from the fit (equation 6.1) at an angle $\Phi_{\parallel 1}$ ($\Phi_{\perp 1}$) of the spectrum:

$$G_i^{\parallel/\perp} = A_i(E) \cdot [\cos(\Phi_{\parallel/\perp})]^2 \cdot \exp\left(-\frac{(E - E_i)^2}{W_i^2/4 \ln 2}\right) \quad (6.6)$$

By comparing the spectral contributions to the LD spectrum in figures 6.13c and d, the origin of the bands of the LD spectra is revealed. For figure 6.13c the energy differences $\Delta E_{ij} = E_i - E_j$ between bands 1 and 2, 3 and 4 (ΔE_{12} and ΔE_{34}) are small compared to the ones in figure 6.13d. The LD spectrum results from the differences in amplitude of the individual contributions. As the amplitude of G_3^{\parallel} is significantly larger than the amplitude of G_4^{\perp} and the spectral separation ΔE_{34} small, there is no negative contribution to the LD spectrum. On the other hand, for the spectrum shown in figure 6.13d, the energetic separations ΔE_{34} are significantly larger than for the spectrum in figure 6.13c. Together with nearly equal amplitudes of the contributions G_3^{\parallel} and G_4^{\perp} , this results in a negative band of the LD spectrum at higher energies.

This analysis showed that the amplitude and the spectral separation of the gaussian transition bands determine the formation of bands in the LD spectrum of individual chlorosomes. The distribution of ΔE_{12} and ΔE_{34} in figure 6.7 showed that only few spectra show a large energetic separation ΔE_{ij} . This explains the small number of

spectra with a negative LD band. Hence, in the ensemble spectrum, the small negative band vanishes due to the larger number of spectra without a negative band (see figure 6.12).

6.6 Discussion of WT-group2

The attention is now shifted to the chlorosomes that were assigned to WT-group2, which make up 26% of population observed. For this group, it was found above that the polarization-resolved fluorescence-excitation spectra do not follow the “standard” pattern that may be attributed to tubular structures. Instead, their spectra can be decomposed into four contributions whose gross mutual polarization behavior can be expressed as $1\parallel 2$, $1\perp 3$, and $3\perp 4$ (implying $1\parallel 4$ and $2\parallel 4$). At first sight, the mutually orthogonal

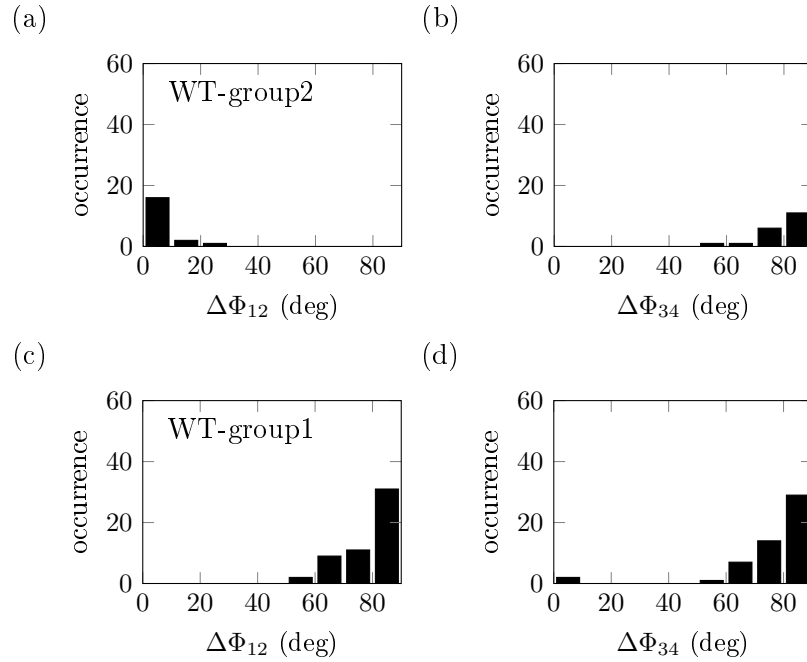


Figure 6.14: Distributions of the relative phase angles Φ between the bands 1 and 2 and between the bands 3 and 4 for the chlorosomes from (a,b) the WT-group2 and (c,d) WT-group1.

transition dipole moments for the two transitions highest in energy (see figure 6.14b) seem to suggest that some structural elements of cylindrical symmetry prevail as well for the WT-group2 chlorosomes.

However, it is worth noting that except for the deviation of the polarization pattern from that of the WT-group1 chlorosomes, no other observations were found that could be used for discriminating the two groups of chlorosomes. The distributions of the spectral peak positions E_1 - E_4 and the widths W_1 - W_4 of the four bands cover a similar range for

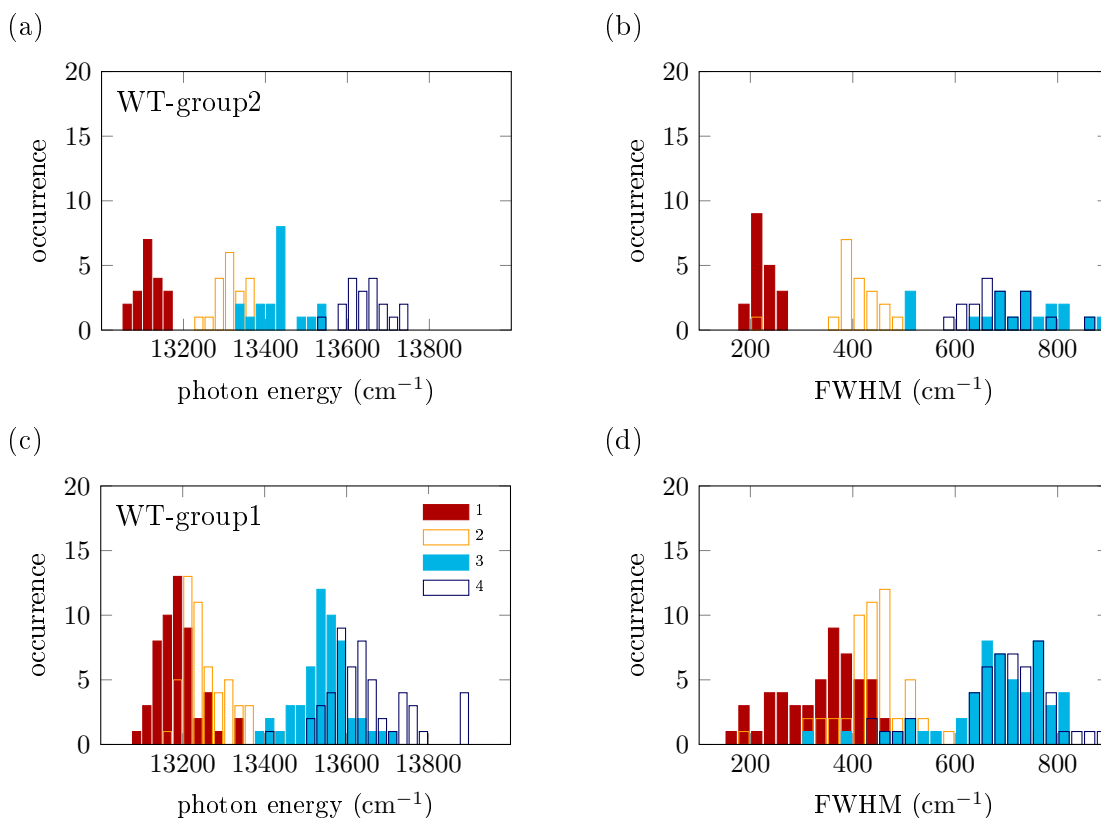


Figure 6.15: Top: WT-group2; Bottom: WT-group1. (a,c) Distributions of the spectral peak positions of the fitted Gaussians and (b,d) distributions of the widths (FWHM) of the fitted Gaussians.

both groups (see figure 6.15). Summing the polarization-averaged spectra from individual chlorosomes for each group separately yields similar fluorescence-excitation spectra, peaking at $13\,458\text{ cm}^{-1}$ (743.1 nm) and $13\,435\text{ cm}^{-1}$ (744.3 nm) with widths (FWHM) of 785 cm^{-1} and 766 cm^{-1} for WT-group1 and WT-group2, respectively. Interestingly, comparing the distributions of the spectral peak positions shown in figure 6.15a,c reveals that for the WT-group2 chlorosomes, the peak positions of the four fitted bands are spread evenly across the spectrum. In other words, grouping the four bands into a low-energy pair and a high-energy pair, which was an obvious step to take for the chlorosomes from WT-group1, cannot be easily justified for the WT-group2 chlorosomes. Hence, on the basis of the information at hand, it cannot be ruled out that all four transitions come from one superstructure.

7 Structure and structural variations of light-harvesting aggregates in chlorosomes

The following chapter presents, among others, the interpretation of the data presented in chapter 6, which has been published in references [2] and [3]. Sections are partly taken directly from the publications.

The analysis of the optical features of the polarization-resolved spectra in chapter 6 elucidated tubular arrangements of BChl as the dominant structure of the light-harvesting aggregates in chlorosomes from the *bchR* mutant, the *bchQR* mutant, and in a majority of the chlorosomes from the WT (WT-group1). The angle between the molecular transition dipole moments and the cylinder axis (β) was determined from the analysis of the polarization-resolved spectra. In order to associate the spectroscopic data with a microscopic model, the lattice structure deduced by Ganapathy et al. from NMR and molecular modeling (see section 3.4) is now used as a starting point. The results obtained by the polarization-resolved, fluorescence-excitation spectroscopy are combined with the information from this model and from cryo-electron microscopy images. The combination of these techniques yields unambiguous information on the structure of the bacteriochlorophyll aggregates within the chlorosomes. Furthermore, theoretical modeling will be used to simulate spectra of the obtained model structure.

The single-particle technique also revealed small spectral variations between the spectra of individual chlorosomes, which can be interpreted as structural variations. These variations are studied by theoretical modeling. Moreover, it is possible to estimate the curvature variation of the secondary structures in chlorosomes quantitatively.

7.1 Modelstructure of the secondary structures in chlorosomes

The data of the mutual polarization angles presented in section 6.2 showed that certain optical transitions that underlie the spectra of individual chlorosomes are polarized more or less perpendicular to each other, while others are polarized nearly parallel to each other. The observed polarization properties are consistent with, and a strong independent

indication for, an underlying tubular symmetry for the overall BChl arrangement within an aggregate [77, 79, 88]. The strong resonant excitation-transfer interactions between the individual BChl molecules lead to the formation of Frenkel excitons, i.e., collective electronic excitations shared by many molecules. The observations reflect the robustness of excitons in self-assembled nanotubes against the localization effects of random disorder in their microscopic parameters, such as the transition energies of the individual molecules as a result of random solvent shifts [96]. This robustness can be traced back to the behavior of the exciton density of states near the band bottom and results in strongly delocalized exciton states whose wave functions (and thus excitation densities) wind around the tube at least once, which in turn leads to a clear distinction between optical transitions with a polarization perpendicular and parallel, respectively, to the axis of the tube [96]. This interpretation is confirmed by cryo-EM imaging, which indeed reveals a tubular arrangement of the BChl molecules.

Structural models for tubular aggregates can be obtained by wrapping a two-dimensional lattice of molecules on a cylindrical surface [75]. In order to associate the spectroscopic and cryo-EM imaging data with a microscopic model, as a starting point the type of lattice deduced by Ganapathy et al. from NMR and molecular modeling for the chlorosomes from the WT, the *bchQRU* mutant and the *bchQR* mutant was used [1, 50] (see section 3.4). Thus, an oblique two-dimensional lattice, as depicted in figure 7.1 is considered. This lattice is rolled on a cylindrical surface along the chiral vector C that makes an angle δ with the a -axis. In order to obtain a seamless tube, the chiral vector should connect two lattice points. Its length equals the tube's circumference.

To be able to translate the information about the angles β_{12} and β_{34} unambiguously into model for the molecular arrangement of transition dipole moments on a cylindrical surface, information from cryo-EM is needed. From the cryo-EM power spectra of individual chlorosomes, a repeat distance (stacking distance d) in the tubular arrangement of the BChl molecules within the aggregates of (1.24 ± 0.06) nm in the direction of the cylinder axis was observed for the chlorosomes of the *bchR* mutant (see figure A.9). This value is close to the (1.22 ± 0.03) nm that has been found for the WT [1]. Table 7.1 provides the distances that were obtained from cryo-EM for the three species. Here, the value of 0.69 nm found for the *bchQR* mutant [50] is significantly smaller than the values that have been found for the WT and the *bchR* mutant, respectively. However, this discrepancy is easy to understand. The stacking distance is defined as the spacing between adjacent, symmetry-equivalent BChls within the supramolecular structures. According to reference [50], the structural changes induced by the *bchQR* mutation lead to a deformation of the tetrapyrrole backbone of the BChl molecules that induces an arrangement of the BChl molecules in extended domains of alternating stacks of BChl molecules either in *syn* or *anti* orientation. In other words, in contrast to the chlorosomes of the WT and *bchR* strains, for which the molecules are arranged in dimeric *syn-anti* stacks, the

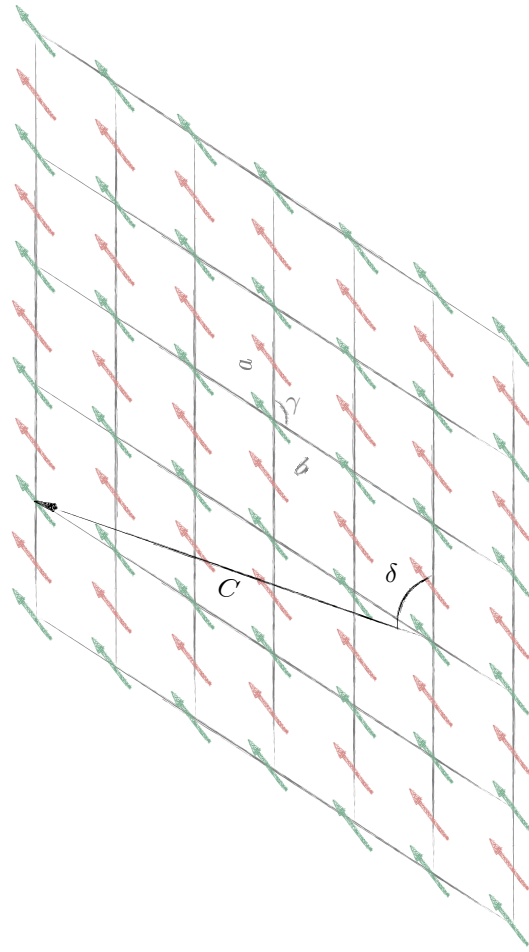


Figure 7.1: Lattice structure of the bacteriochlorophyll monomer arrangement as proposed in [1]. The rolling vector is referred to as C .

BChl molecules in the *bchQR* mutant are arranged in monomer stacks (see section 3.4). As a consequence of this, the distance between adjacent, symmetry-equivalent BChls of 0.69 nm refers to the monomer repeat distance and not to the dimer repeat distance as for the other two species. Considering that in the *bchQR* mutant the assembly in parallel monomers is imposed by structural deformations of the BChl molecules, the value of 0.69 nm is in reasonable agreement with the 0.63 nm that results when the lattice parameter of $a \approx 1.25$ nm of the unit cell shown in figure 3.4 is cut in half. At any rate, from the perspective of spectroscopy, it is impossible to distinguish between dimeric *syn-anti* stacking or extended domains of monomeric (whether *syn* or *anti*) BChl arrangements because for *syn-anti* stacking, the concomitant alternation of the transition dipole moments by only $\pm 4^\circ$ with respect to the plane of the cylinder is too small to make a detectable impact on the spectra.

Hence, the stacking distances of the WT, the *bchR* mutant, and the *bchQR* mutant are almost identical. The stacking distance of the WT was transferred into a supramolecular

Table 7.1: Summary of the values of the model parameters for the WT, the *bchR* mutant, and the *bchQR* mutant obtained by spectroscopy (*), cryo-EM (this work **) and from references [1, 50].

	WT	<i>bchR</i>	<i>bchQR</i>
a (nm)	1.25	1.297/1.294	1.25
b (nm)	0.98	0.98	0.98
γ ($^\circ$)	122	122	122
η ($^\circ$)	35	35	35
β ($^\circ$)	57.3/51.7 *	56/52 *	56.1/53.1 *
d (nm)	1.22	1.24 **	0.69

model structure by Ganapathy et al. using the molecular grid presented in figure 7.1. Therefore, the lattice structure is wrapped onto a cylindrical surface with an angle δ . From the stacking distance, a rolling angle of $\delta = 90^\circ$ was concluded for the WT. This lead to a spatial periodicity given by the lattice constant a for the WT, which showed good agreement with the stacking distance observed in cryo-EM for this species. The lattice parameters are also listed in table 7.1.

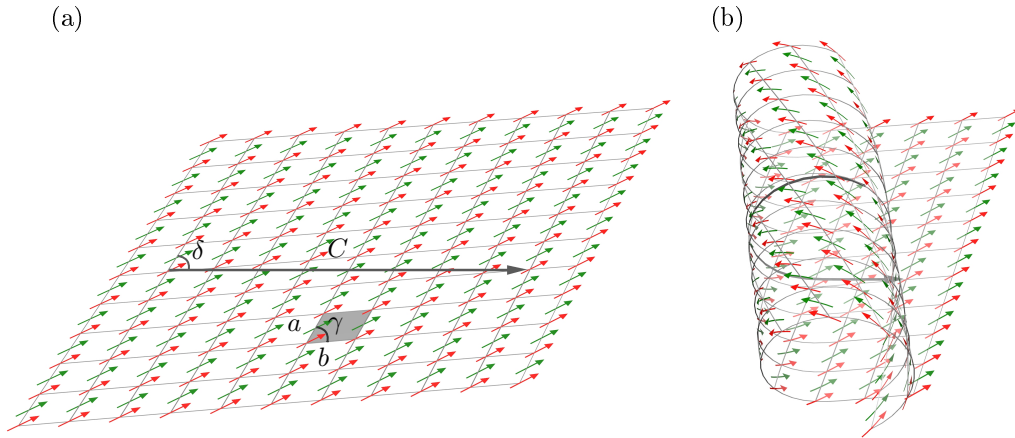


Figure 7.2: (a) Bravais lattice obtained from NMR for the short-range order of the BChl molecules according to reference [1]. Each arrow represents the Q_y transition dipole moment of a BChl molecule. The molecules are arranged on the lattice as described in the caption of figure 3.6. (b) Wrapping the grid onto a cylindrical surface along a rolling vector \vec{C} (black arrow in part (a)) enclosing an angle of $\delta \approx 70^\circ$ with the a -axis of the grid yields the model structure for secondary elements in the chlorosomes of the WT, the *bchR* mutant and the *bchQR* mutant.

The values β obtained by fluorescence-excitation spectroscopy for the WT-group1, the *bchR* mutant and the *bchQR* mutant are provided in table 7.1. Remarkably, the angles β are centered around a similar mean of about 55° . The value of the angle β of $57.3^\circ/51.7^\circ$ for the chlorosomes of WT-group1 is in contrast to the models presented in reference [1], where an angle $\beta = 35^\circ$ was concluded for the wild type by modeling the structural arrangement. In contrast to reference [1], the values β_{12} and β_{34} are obtained experimentally. Thus, from the data it follows that the angles β for all three species, WT-group1, *bchR* mutant, and *bchQR* mutant are very similar, indicating the same basic arrangement of the transition dipole moments in the chlorosomes for these species.

Hence, with the additional information from the fluorescence-excitation experiments, the interpretation of the data in terms of the models presented by Ganapathy et al. should be reconsidered. The only way to explain both the fluorescence excitation experiments and the cryo-EM measurements for the WT (WT-group1), the *bchR* mutant, and the *bchQR* mutant is to use a rolling vector of $\delta \approx 70^\circ$, which gives rise to the tube depicted schematically in figure 7.2.

The important conclusion from the above-presented data from NMR, cryo-EM, and single-molecule spectroscopy yields for all three species, WT-group1, *bchR*, and *bchQR*, the same basic arrangement of the transition dipole moments, that can be visualized by wrapping the lattice obtained from NMR onto a cylindrical surface along a chiral vector that includes an angle δ with the *a*-axis, as illustrated in figure 7.2.

7.2 Theoretical modeling of the spectra of model structures

The above model was used to simulate the polarization-resolved fluorescence-excitation spectra of cylindrical structures. For the theoretical modeling of a spectrum that can be compared to the experimental chlorosome spectra, two cylindrical structures were used to account for the low- and high-energy doublets of the spectrum, respectively.

In order to consider the (possibly) different electrostatic local environments, slightly different (1.5%) site energies for the BChl molecules in the two tubular structures are used. In this context, it is important to note that, given the spacing between the concentric cylinders of about 2.1 nm, the multiple cylinders can be treated as uncoupled systems for modeling the optical spectra, as has been shown previously [88]. The parameters used for the modeling are given in table 7.1.

The simulations have been carried out for cylindrical structures with radii $r_1 = 14.7$ nm and $r_2 = 9.7$ nm that have a length of 30 nm each and *N* molecules. In order to obtain closed cylinders that are consistent with the structure parameters given in table 7.1, the lattice parameters of the grid were slightly varied as detailed in table 7.2. The angle β is directly linked to the rolling angle δ via $\beta = |(90^\circ - \delta + \eta) \bmod 180^\circ|$. The stacking distance *d* along the tube's axis is given by $d = a \cdot \sin \delta$. For the dipole strength of

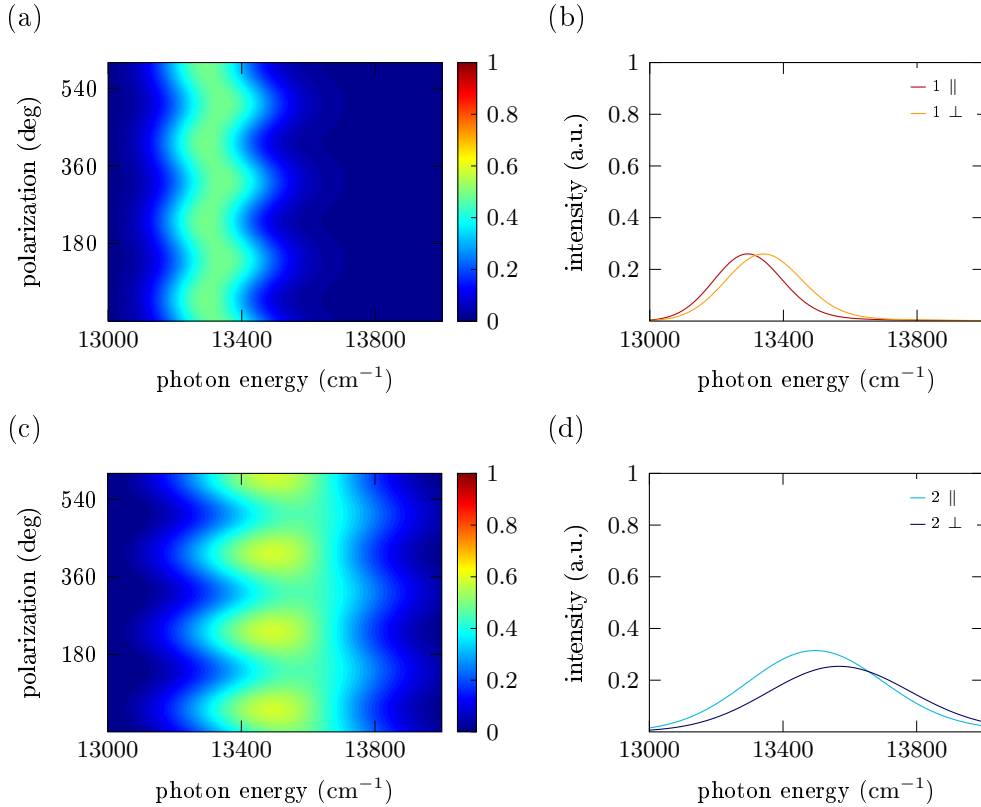


Figure 7.3: Spectra of the individual cylinders used for the simulation shown in figure 7.4. (a) Polarisation-resolved spectrum from cylinder 1, and (b) polarisation-resolved spectrum averaged over all polarisations. (c,d) Polarisation-resolved and averaged spectrum from cylinder 2. The values used for the parameters of the simulation are given in table 7.2.

the monomers $\mu^2 = 30 \text{ D}^2$ was used [43], and for the site energies of the monomers within the two cylinders 15300 cm^{-1} and 15500 cm^{-1} was used, respectively. A slight difference in site energies can be the result of different local environments, caused for example by different dielectric shielding. This is not unlikely if both cylinders together make up a double-walled structure. Subsequently, the stick spectrum resulting from eigenvectors and eigenvalues of the Hamiltonian (as described in section 5.4) was dressed with a gaussian lineshapes. The width of the gaussians were chosen similar to the results from the experiment (see figure 6.4): $S_1 = 100 \text{ cm}^{-1}$, $S_2 = 100 \text{ cm}^{-1}$, $S_3 = 200 \text{ cm}^{-1}$, $S_4 = 200 \text{ cm}^{-1}$. Figure 7.3 shows the contributions of the individual cylinders to the overall spectrum in figure 7.4.

The simulated spectrum presented in figure 7.4, which is a combination of the spectra from the two cylindrical arrangements, shows a reasonable agreement with the measured one in figure 6.3c. In particular, the energy spacing (both magnitude and direction) between the transitions in the low- and high-energy doublets from the analysis of the experimental data ($\Delta E_{12} = 34 \text{ cm}^{-1}$, $\Delta E_{34} = 62 \text{ cm}^{-1}$, see figure 6.3b) is reproduced rather

Table 7.2: Parameters used to simulate the spectra presented in 7.3 and 7.4

	Cylinder 1	Cylinder 2
a (nm)	1.297	1.294
b (nm)	0.98	0.98
d (nm)	1.21	1.24
r (nm)	14.7	9.7
δ ($^\circ$)	69	79
η ($^\circ$)	35	35
β ($^\circ$)	56	52
μ (D)	5.5	5.5
E_0/hc (cm^{-1})	15300	15500
N	5152	3388

well by the simulations ($\Delta E_{12} = 39 \text{ cm}^{-1}$; $\Delta E_{34} = 59 \text{ cm}^{-1}$, see figure 7.4b). For both arrangements, the spatial periodicity (stacking distance of equivalent BChl molecules) along the a -axis agrees within experimental accuracies with the results from cryo-EM. It should be pointed out that the modeling is performed for single aggregates, whereas the spectra have been taken for single chlorosomes that represent an assembly of aggregates. In performing the simulation of figure 7.4, fluctuations in the structure and model pa-

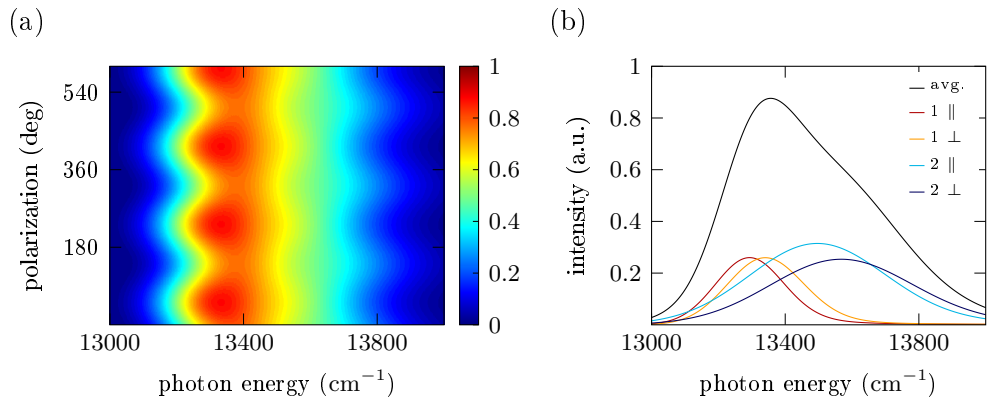


Figure 7.4: Simulation of the polarization-resolved fluorescence-excitation spectrum from two cylindrical aggregates. Each cylinder has a length of 30 nm. The molecules are arranged according to the proposed structure for the WT, the *bchR* mutant and the *bchQR* mutant (see figure 7.2). (a) Two-dimensional polarization-resolved representation. (b) Gaussian profiles of the underlying transitions from cylinder 1 (red, yellow) and cylinder 2 (cyan, blue).

rameters for a single aggregate, such as random transition energy disorder for molecules within an aggregate, have not been taken into account. Furthermore, the value used for the lattice constant a was allowed to differ by at most a few percent, from that reported

by Ganapathy et al. [1], for the WT and *bchQRU* mutant. Given the different side groups of the BChl molecules, such a small variation is not unreasonable.

7.3 Spectral variations explained as variations of the model structure

7.3.1 Simulations of variations of the radius r , rolling angle δ and lattice parameter a

It should be emphasized that the above conclusions are based on quantities obtained from the fluorescence-excitation experiments on individual chlorosomes. Each individual entry in the distributions for the values of these quantities (see figures 6.4, 6.5, 6.7, and 6.10) represents an average over the small ensemble of aggregates that constitutes the particular chlorosome under study (intra-chlorosome variation). Hence, these distributions correspond to the ones of a macroscopic ensemble of chlorosomes. Their widths reflect the fact that, even for the mutant species, heterogeneity is still an important factor. Sources of heterogeneity may be variation in the structural model parameters as well as random disorder in the exciton Hamiltonian resulting from local fluctuations.

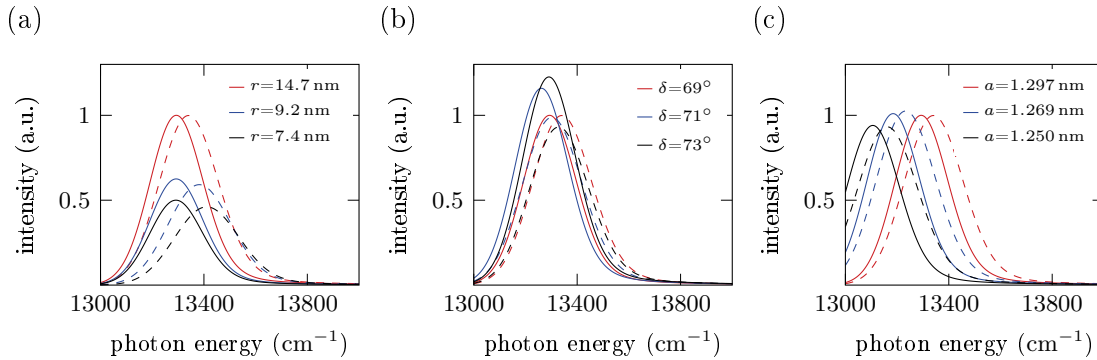


Figure 7.5: Simulated spectra from cylinder structures based on the model described in section 7.1. Each panel shows spectra for three cylinders that differ with respect to each other in one of the model parameters. (a) variation of the cylinder radius r , (b) variation of the wrapping angle δ , (c) variation of the lattice parameter a of the unit cell. In the individual panels the solid line corresponds to the spectral component polarized parallel to the cylinder axis, and the dashed line corresponds to the spectral component polarized perpendicular to the cylinder axis, whereas different colours refer to different values of the parameters used.

In order to address the widths of the distributions of the spectral parameters more quantitatively, the spectral positions and the intensities of the transitions as a function of the radius r , rolling angle δ and lattice parameter a on the spectral positions and intensities of the perpendicular and parallel absorption bands were calculated for a single-wall cylindrical aggregate. Therefore, the values applied for one of the cylinder structures

(cylinder 1) used for figure 7.4 were chosen as the default values (see table 7.3). Subsequently, one of these parameters was varied within reasonable limits, while all other parameters were fixed at their default values, see table 7.3*. In particular, changing the radius r of the cylinder, mainly affects the energy spacing between the superradiant transitions (figure 7.5a). Furthermore, small changes of the rolling direction of the lattice, i.e. the angle δ , affect the ratio of the oscillator strengths of the parallel and perpendicular bands (figure 7.5b). Finally, the unit cell parameter a influences the spectral position of both bands (figure 7.5c). Note that, d is directly related to a via $d = a \cdot \sin \delta$.

These calculations show that broadening of the Gaussian transition bands as well as the fluctuations seen in the histograms of figures 6.4 and 6.2 might be caused by small variations of the molecular arrangement and sizes of the tubes.

Table 7.3: Model parameters used to simulate the spectra displayed in figure 7.5. The colours in the legend on the left hand side correspond to the colours of the spectra shown in the figure. The grey background marks the parameters that were varied. The lattice parameters may vary slightly from the default parameters to obtain closed cylinders.

Set of default values of cylinder 1							
	a (nm)	d (nm)	r nm	δ ($^\circ$)	η ($^\circ$)	β ($^\circ$)	N
Red	1.297	1.21	14.7	69	35	56	5152
Variation of radius r							
Blue	1.297	1.21	9.2	69	35	56	3220
Black	1.297	1.21	7.4	69	35	56	2576
Variation of rolling angle δ							
Blue	1.287	1.22	15.4	71	35	54	5400
Black	1.297	1.24	15.2	73	35	52	5324
Variation of lattice parameter a							
Blue	1.269	1.18	14.8	69	35	56	5280
Black	1.250	1.17	13.5	69	35	56	4890

7.3.2 Correlation between the energetic separation of spectral components and the radius of cylindrical structures

The evaluation of the polarization-resolved spectra revealed pairs of gaussian transitions energetically close to each other (see section 6.2). In figure 6.7 the statistics of the energetic separations ΔE_{12} and ΔE_{34} of the two mutually orthogonal polarized spectral components from the low-energy doublet and high-energy-doublet for WT-group1, the

*Note that the lattice parameters may vary slightly from the default parameters to obtain closed cylinders.

bchR mutant and the *bchQR* mutant were presented. Both doublets feature distributions for their spectral separation. Nevertheless, for an individual chlorosome, the spectral separations within the low-energy doublet and the high-energy doublet, ΔE_{12} or ΔE_{34} , are correlated. Remarkably, figure 7.6 shows that the energetic separations for all three species (WT-group1, *bchR*, and *bchQR*) correlate and accumulate around a line that roughly satisfies the relation $\Delta E_{34} \approx 1.5 \cdot \Delta E_{12}$. Such correlations are not observable for other combinations ΔE_{ij} and ΔE_{kl} (for $i, j \neq k, l$), as it is demonstrated for the *bchR* mutant in figures A.10b,c.

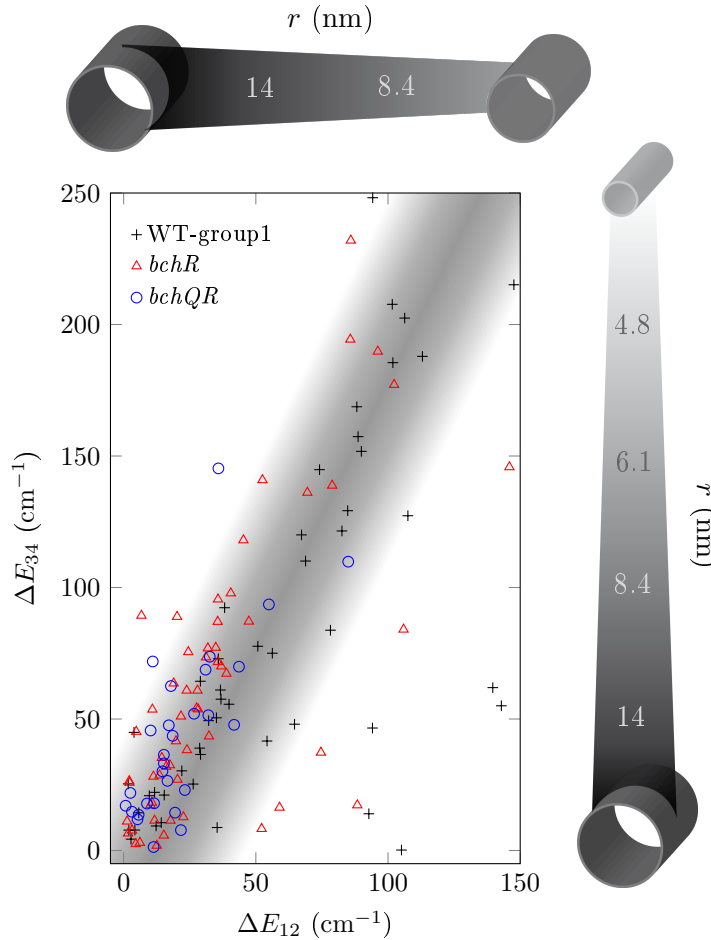


Figure 7.6: Correlation between the energetic separations of the low- and high-energy doublet ΔE_{12} and ΔE_{34} . The shaded area indicates the range of the most frequently observed energy splittings. The structures on the top and on the right-hand side of the diagram illustrate the radii of tubular structures that are consistent with the respective energy differences. The particular radius scales displayed here have been obtained using exciton model calculations.

For single-wall aggregates of tubular symmetry, the energetic separation between mutually orthogonal polarized spectral bands, i.e., ΔE_{12} and ΔE_{34} , is related to the curvature of the structure [77]. Explicitly, the energetic separation scales roughly proportional to

the curvature. Simulations, as in section 7.3.1, were made to link the energetic separations with actual values for radii. Therefore, the fluorescence-excitation spectra of cylinders with parameters $a = 1.297$ nm, $b = 0.98$ nm, $\delta = 69^\circ$, and $\eta = 35^\circ$ were simulated. The radius was varied between 3.7 nm and 16.6 nm. From these spectra, the energetic splitting between the bands was analyzed. The data is presented in table 7.4.

The energetic splitting increases for increasing curvature, i.e. decreasing radius of the underlying cylinder, see table 7.4 and figure 7.7. The data has been fitted using the equation [77]:

$$\Delta E = 8J \sin^2 \left(\frac{s \cdot \sin \theta + d \cdot \cos \theta}{2r} \right) \quad (7.1)$$

Here, J denotes the exciton transfer interaction, s , θ , and d are structural lattice parameters and r the radius of the cylindrical structure presented in reference [77].

Table 7.4: Relation between the radius of the underlying cylinder structure and the energetic separation $\Delta E_{\parallel,\perp}$ of the two mutually orthogonal polarised bands in the spectrum.

r (nm)	3.7	5.5	7.4	9.2	11.1	12.9	14.7	16.6
$\Delta E_{\parallel,\perp}$ (cm ⁻¹)	270	169	119	89	70	57	47	40

With the results from the simulation, it is possible to give a physical interpretation of the energy differences ΔE_{12} and ΔE_{34} within both pairs of transitions for the WT-group1, *bchR*, and *bchQR* species (the data is shown in figure 6.7) and a speculation about the relation between both pairs.

The data points of the energy splitting in figure 7.6 accumulate around a line indicated by the gray shaded area, that includes 89 % of the total data points (87 % for WT-group1, 86 % for *bchR*, 97 % for *bchQR*). For the chlorosomes from the WT-group1 and the *bchR* mutant, ΔE_{12} (ΔE_{34}) covers the range of 0 cm⁻¹ to 150 cm⁻¹ (250 cm⁻¹), whereas these ranges are restricted for ΔE_{12} (ΔE_{34}) to 0 cm⁻¹-50 cm⁻¹ (150 cm⁻¹), respectively, for the *bchQR* mutant. This correlation implies, in particular, that the structure associated with the low-energy doublet (12) has a smaller curvature than the one associated with the high-energy doublet (34). This would be consistent with interpreting both doublets to derive from concentric double- or multilayer tubular arrangements of the BChl aggregates within the chlorosomes. Using values for the radius, obtained by the exciton model calculations from above (see figure 7.7), the variation of the radius is found to cover a range of about 4 nm to 20 nm for WT-group1 and the *bchR* mutant, whereas this inter-chlorosome variation is less pronounced for the *bchQR* mutant featuring structures with radii in the range of 7 nm to 20 nm, that is lacking the structures with the strongest curvature (see right and top axes in figure 7.6).

Furthermore, the correlation between ΔE_{12} and ΔE_{34} is a strong signature for an underlying structural hierarchy within the overall organization of the BChl assembly.

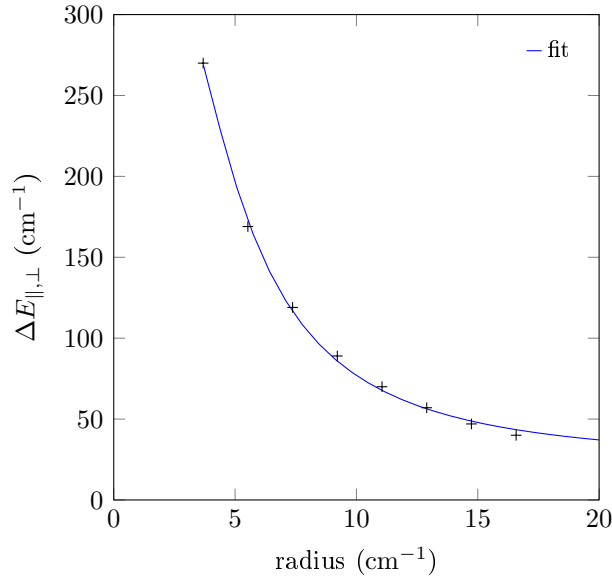


Figure 7.7: Energetic separation $\Delta E_{||,\perp}$ between the two mutually orthogonal polarized spectral components in a doublet as a function of the cylinder radius. For this example calculation the default values in table 7.3) have been used as parameters with a variation of r . The data has been fitted using the equation given in reference [77].

The average curvature of the structural elements within a particular chlorosome displays strong variations from one chlorosome to the other (interchlorosome variation) for all three species. Given the widths of the distributions for ΔE_{12} and ΔE_{34} on the one hand and the reasonable degree of correlation between their values in an individual chlorosome, on the other hand, the data shown in figure 7.6 provide information about the extremes of the variations of the structural elements between the individual chlorosomes. Hence, it is conceivable that for some chlorosomes the dominating spectral contributions stem from structural elements with rather similar curvatures, figure 7.8a, whereas for other chlorosomes, the dominating spectral contributions stem from structural elements with a higher degree of variation, figure 7.8b. However, in a macroscopic ensemble of chlorosomes, this will be manifested as a contribution to the broadening of the distributions. Considering the strong variation of the radii of the structures in individual chlorosomes, it is reasonable to speculate, that a chlorosome contains a mixture of secondary aggregates with various radii (see figure 7.8c).

The variations of the energetic splitting (i.e., the size of the tubular structures) within one species may reflect different growth conditions for the different bacteria from which the macroscopic ensemble of chlorosomes is extracted, for example, differences in chlorosome structure during the course of growth and biogenesis of these structures.

This idea is supported by the existence of some degree of correlation between the energetic splitting within one of the doublets and the corresponding emitted intensity. Figure

7.9 displays the integrated emission intensity from a single chlorosome as a function of the energetic splitting ΔE_{12} . However, a quantitative comparison of the intensities was difficult to accomplish, because the experiments were carried out over an extended period in time on different setups using slightly different experimental parameters (focussing, transmission differences of optical filters etc.). Therefore, six individual chlorosomes

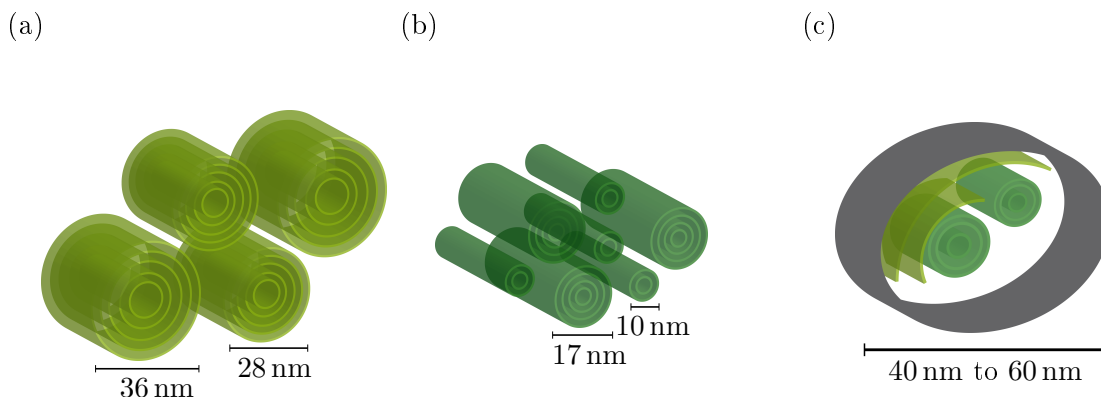


Figure 7.8: Speculation about the variation of the overall supramolecular arrangement of the BChl molecules between individual chlorosomes. (a) Cylinders with an overall similar curvature. (b) Cylinders with strongly varying curvatures. (c) Cylinders and curved lamellae with strongly varying curvatures. The gray structure indicates the phospholipid envelope.

were chosen featuring a small energetic splitting, an intermediate energetic splitting, and a large energetic splitting ΔE_{12} , respectively. The red crosses in figure 7.9 correspond to the median of both parameters (splitting and intensity) for each group separately. Figure 7.9 displays a weak correlation between these parameters. The emitted intensity is proportional to the number of monomers in the chlorosome. Furthermore the number of BChls in a chlorosome is proportional to the size of the chlorosome and therefore its state of growth. In particular, this means that chlorosomes that have a higher emission are in general larger than chlorosomes emitting only a low intensity. The energetic splitting, on the other hand, is proportional to the curvature of the secondary structures in chlorosomes. Therefore, the correlation of the emitted intensity and the energetic splitting suggests that during growth, the average radius of the tubular aggregates within a chlorosome increases. This might result from an increased occurrence of multilayer concentric BChl aggregates during growth, which would be favorable, as it leads to a high-density packing of molecules.

7.4 Discussion

A large amount of information was obtained from the polarization-resolved, fluorescence-excitation spectra of individual chlorosomes from the WT, the *bchR* single mutant, and

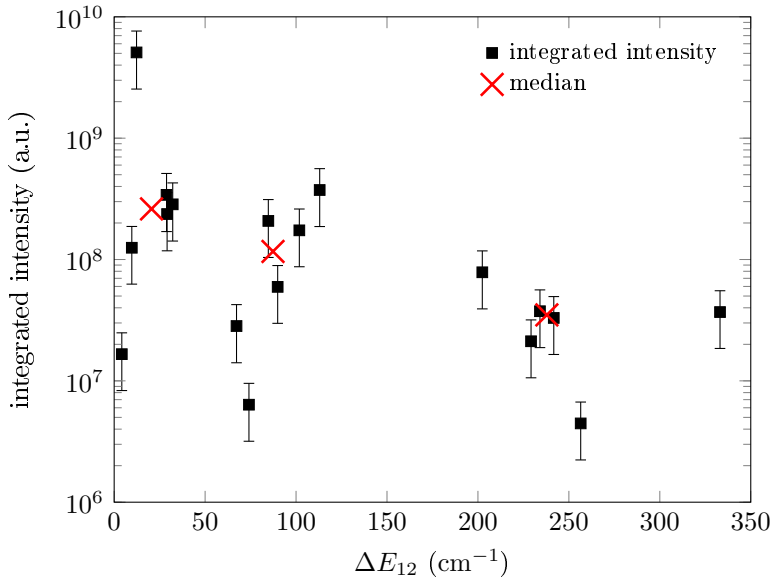


Figure 7.9: Integrated intensity of the emission of single chlorosomes from WT-group1 as a function of the energetic splitting, ΔE_{12} , of the low-energy doublet. The data correspond to 3 groups of 6 chlorosomes each featuring a small, intermediate and large energy splitting ΔE_{12} . The red crosses correspond to the median of both parameters (intensity and energetic splitting) for each subgroup of the chlorosomes.

the *bchQR* double mutant. The detailed analysis of these spectra allows to draw conclusions about the structural arrangement of the BChls in chlorosomes, but also to determine structural differences.

It was observed that the spectral heterogeneity diminished in the order WT > *bchR* single mutant > *bchQR* double mutant, clearly demonstrating that the higher degree of structural order achieved through the mutations allows better resolution of distinctive spectral features (also see reference [87]). The *bchR* and *bchQR* mutations correspond to a removal of methyl groups from the sidechains of the BChl *c* molecules, namely, one at C-12 for *bchR*, and additional ones at C-8 for *bchQR* (see also table 3.1). It is therefore tempting to speculate that the methylations effectively substitute for protein interactions for fine-tuning the site energies of the monomers to achieve a broadening of the absorption band for better spectral coverage in the natural organisms. If so, the methylations and the induced structural disorder would be of functional importance for optimizing the light-harvesting efficiency of the chlorosomes. From the linewidth distributions of the single chlorosome spectra (see figure 6.4b,d,f), it becomes apparent that this overall broadening is already a property of the individual chlorosomes rather than of the macroscopic population as a whole.

A global analysis revealed that the spectra of individual chlorosomes are composed of four Gaussian transition bands. The statistics of the fit parameters showed that bands 1 and 2 result from pairs of exciton states with lower energies, whereas bands 3 and 4 derive

from similar pairs with higher energies. The polarization features of these pairs revealed a cylindrical symmetry for the arrangement of the BChls in the chlorosomes of the *bchR* mutant, the *bchQR* mutant and a vast majority of the WT chlorosomes. Therefore, the low- and high-energy doublets are associated with different cylindrical arrangements in the chlorosome. The reason that both doublets have a different average transition energy may originate from different solvent shifts for the molecular transition energies, owing to a different environment within a multilayer structure and (or) to slightly different lattice parameters for the different cylindrical aggregates. It is also tempting to speculate, that the correlation of the width (see figure 6.4b,d,f) between the pairs of electronic transitions, can be interpreted as a relaxation of the states of the higher-lying doublet to the lower one. However, the correlation of the width of the transitions within one of the doublets is not so easy to explain. In the chlorosomes the width of the transition parallel to the cylinder axis is, in general, smaller than the width of the perpendicular one. A study on artificial light-harvesting nanotubes (self-aggregated zinc chlorin monomers), which mimic the secondary aggregates in chlorosomes, showed an inverse behaviour of the FWHM of the transition bands [97]. Therefore, the origin of the correlation of the width between the pairs of electronic transitions needs further investigation. However, the study showed that this biomimetic light-harvesting aggregate might function as a model system for the secondary structures in chlorosomes. The nanotubes reproduce the angle β (angle between the molecular dipole moment of the BChls and the long axis of the cylindrical aggregates), which was determined to be around 55° for all species of chlorosomes (WT-group1, *bchR* mutant, *bchQR* mutant). Interestingly, this value corresponds approximately to the magic angle. This connection shows impressively how well designed the chlorosomes are. The arrangement of BChls close to the magic angle allows the most efficient absorption of photons regardless of their polarization.

Another important piece of information was obtained from cryo-EM experiments. The stacking distance along the axis of the tube is given by $d = a \cdot \sin \delta$. The close agreement between the stacking distance for the WT, the *bchR* mutant and the *bchQR* mutant (table 7.1) suggested that all chlorosome arrangements are compatible with the same structural model. Together with the angle β , which is directly linked to the rolling angle δ via $\beta = |(90^\circ - \delta + \eta) \bmod 180^\circ|$, a model structure was built by wrapping the NMR lattice reported in reference [1] onto a cylindrical surface along a rolling vector that is inclined by about $\delta \approx 70^\circ$ with respect to the a -axis of the grid.

This unified model structure for the secondary structures in chlorosomes from the WT, the *bchR* mutant, and the *bchQR* mutant was obtained from the combination of information from single-particle spectroscopy and cryo-EM with previous data from NMR and molecular modeling. Recent studies also claimed that the combination of techniques is necessary to obtain unambiguous information about the structure of the aggregates in chlorosomes [98]. In contrast to the statement from Li et al. that their results contradict

the results presented in this work, values for the rolling vector δ similar to the one presented here arise from their theoretical study. The fact that another theoretical approach comes up with similar results as the experimental study presented here supports again the presented model structure.

Yet, only the experimental study on individual chlorosomes presented here enables one to study differences in the details of the monomer arrangement between the strains, and between the secondary structures within one strain. Interestingly, the simulations revealed that the influence of the long-range order of the BChl arrangement, such as variations of the curvature of the cylindrical surface or a spread in the rolling angle are not decisive for the details in the ensemble absorption spectra of the chlorosomes. A scatter in these parameters manifests itself mainly in the widths of the absorption bands. The energy splittings observed between the various spectral peaks of individual chlorosomes of the WT-group1, the *bchR* mutant, and *bchQR* mutant strains revealed interesting information. In particular, (i) a strong correlation exists between the energetic separations within the absorption doublets that are observed (i.e., ΔE_{12} vs. ΔE_{34}). This provides strong evidence for close similarities in the molecular arrangement for all three chlorosome types and for a structural hierarchy in the molecular packing within one chlorosome. In particular, the structure associated with the low-energy doublet (12) has a larger radius than the one associated with the high-energy doublet (34). This would be consistent with interpreting both doublets to derive from concentric double- or multilayer tubular arrangements of the BChl aggregates within the chlorosomes. For instance, the aggregates of radii r_1 and r_2 used in the above modeling (section 7.2) may well be concentric tubes (as depicted in figure 7.8). (ii) Within an ensemble of chlorosomes from the same strain, the individual aggregates feature strong variations in the curvature of their secondary structural elements. (iii) Between different strains (here WT, *bchR* mutant vs *bchQR* mutant), the chlorosomes feature strong variations in the radii of their secondary structural elements. It appears that in the *bchQR* chlorosomes, the tubular elements with small radii are lacking, which is in contrast to those from the other two strains.

Given that distributions for all experimental parameters were observed, it is reasonable to propose that a macroscopic ensemble of chlorosomes is best represented by a mixture of organelles in which each individual chlorosome accommodates differently curved superstructures (see figures 7.6 and 7.8).

This conclusion is supported by the second spectral pattern that was found for about one-quarter of the WT chlorosomes. The spectra showed features that might originate from cylindrical as well as other secondary structural elements. As shown by the Vacha group [58], for sufficiently large curvatures, it suffices to consider only a quarter-cylinder as the primary structural element to reproduce similar spectral signatures as obtained for a closed cylinder. Hence, it finally may be speculated that curved structural elements

other than closed cylinders, i.e., partial cylinders, lamellae, or spirals could contribute to the observed spectral properties (see figure 7.8c). This might also explain some of the debates in the literature concerning different supramolecular organisations of the BChl molecules [1, 42, 44–46, 50, 52, 55, 57–59, 86, 89] (see section 3.2).

8 Summary

In this thesis, individual chlorosomes from the WT, the *bchR* single mutant, and the *bchQR* double mutant were studied by polarization-resolved, fluorescence-excitation spectroscopy. The polarization features observed in these spectra reflected a high degree of organization of the BChls molecules in the chlorosomes. This indicated the arrangement of the BChls into secondary structural elements.

The analysis of the polarization-resolved spectra revealed two types of spectral patterns for the chlorosomes of the WT. The optical features of the single-particle spectra of the vast majority of the WT chlorosomes (75%), as well as for the chlorosomes of the *bchR* single mutant and the *bchQR* double mutant showed that the predominant structural element for the meso-organization of the monomers features a tubular symmetry.

To pinpoint the precise structure of the light-harvesting aggregates in individual chlorosomes, a combination of optical and cryo-EM and NMR experiments was used. Two essential pieces of information were derived from these experiments. The optical data yield the angle β , which is the angle between the molecular transition dipole moment of the BChls and the long axis of cylindrical aggregates. The EM data yield the stacking distance along the axis of the tube. These two informations are combined to a model of the molecular arrangement of BChls in secondary structures in the chlorosomes. The molecular packing of these aggregates can be reproduced by wrapping the lattice structure reported in reference [1] onto a cylindrical surface along a rolling vector that is inclined by about $\delta = 70^\circ$ with respect to the *a*-axis of the grid. For the WT chlorosomes, this is in contrast to what has been reported before [1]. The presented model structure is compatible with the data of the chlorosomes from all three species. This implies that the secondary structures of all species can be described with a single model structure.

It was shown, that it is possible to reconstruct LD spectra from polarization-resolved, fluorescence-excitation spectra of individual chlorosomes. Although this technique produces the LD ensemble spectrum of a perfectly aligned sample of chlorosomes, it does not yield the spectroscopic information on which the presented model structure is based.

Simulations of spectra obtained by theoretical modeling of the presented structure showed a good agreement with the experimental spectra. Furthermore, studying variations of the structural parameters complete the image that a chlorosome is best represented by a mixture of differently curved superstructures, wherein each structure corresponds to a small variation of the presented model structure.

In summary, by combining information from single-particle spectroscopy and cryo-EM with previous data from NMR and molecular modeling, the dominant structure as well as the structural variation of the light-harvesting aggregates in chlorosomes of *Cba. tepidum* was elucidated. The most important result of this work is that only the combination of these techniques yields unambiguous information on the structure. In contrast, the information from only one technique would have led to different results [2, 3].

Appendices

A Additional experimental data

A.1 Decomposition of the polarization-resolved fluorescence-excitation spectra

The polarization-resolved fluorescence-excitation spectra shown in figure 6.1 were globally fitted using the equation:

$$F(E, \Theta) = B + \sum_{i=1}^4 A_i(E) \cdot [\cos(\Theta - \varphi_i)]^2 \cdot \exp\left(-\frac{(E - E_i)^2}{W_i^2/4 \ln 2}\right) \quad (\text{A.1})$$

A.1.1 Spectra of the wild type

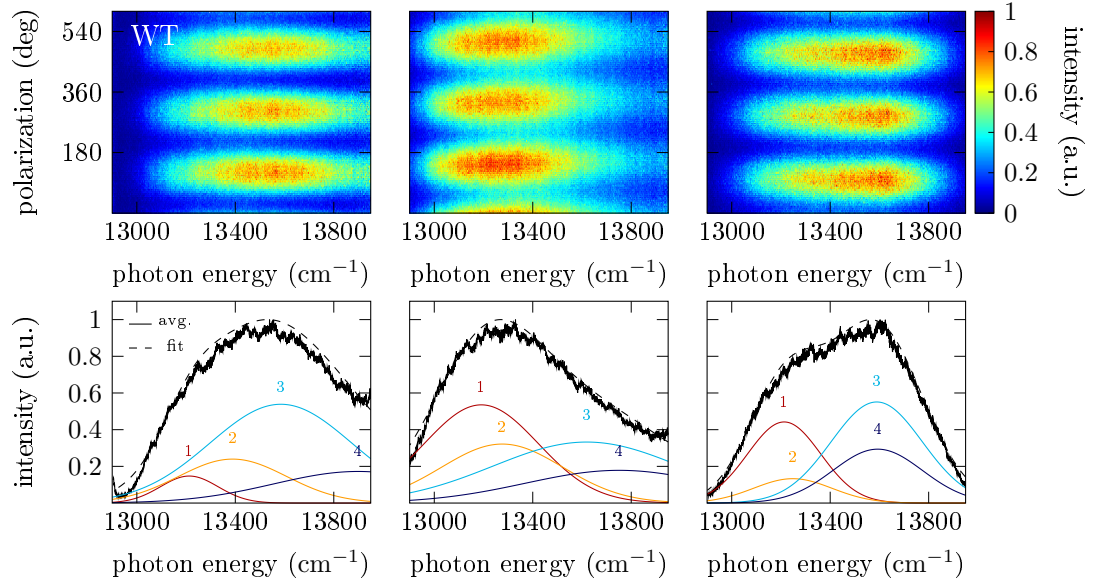


Figure A.1: Examples of polarization-resolved fluorescence-excitation spectra of individual chlorosomes from the WT (spectra from figure 6.1) together with the spectra decomposed into four Gaussians.

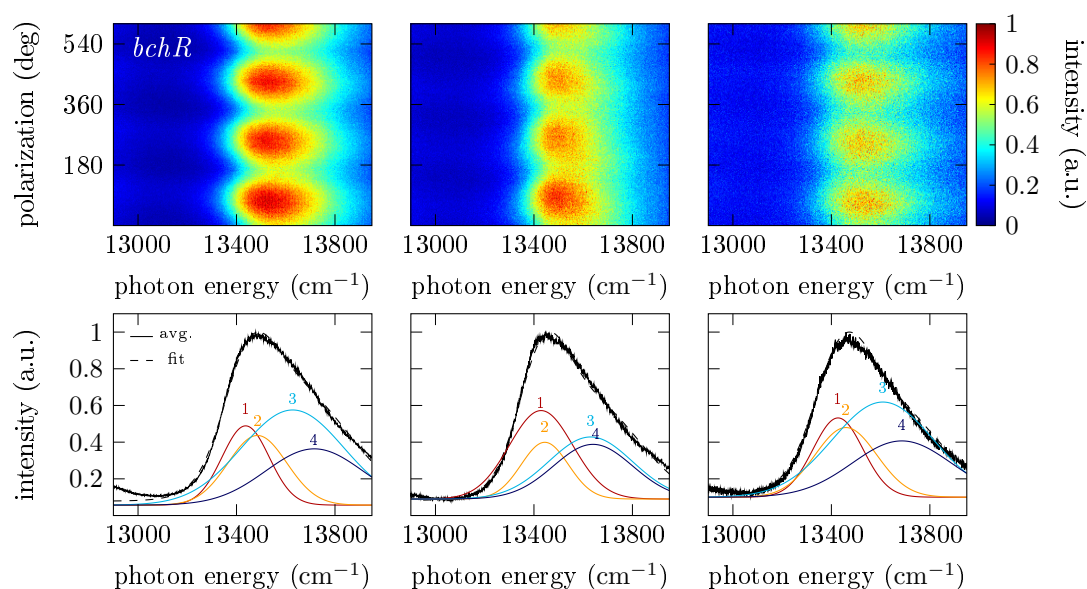
A.1.2 Spectra of the *bchR* mutant

Figure A.2: Examples of polarization-resolved fluorescence-excitation spectra of individual chlorosomes from the *bchR* mutant (spectra from figure 6.1) together with the spectra decomposed into four Gaussians.

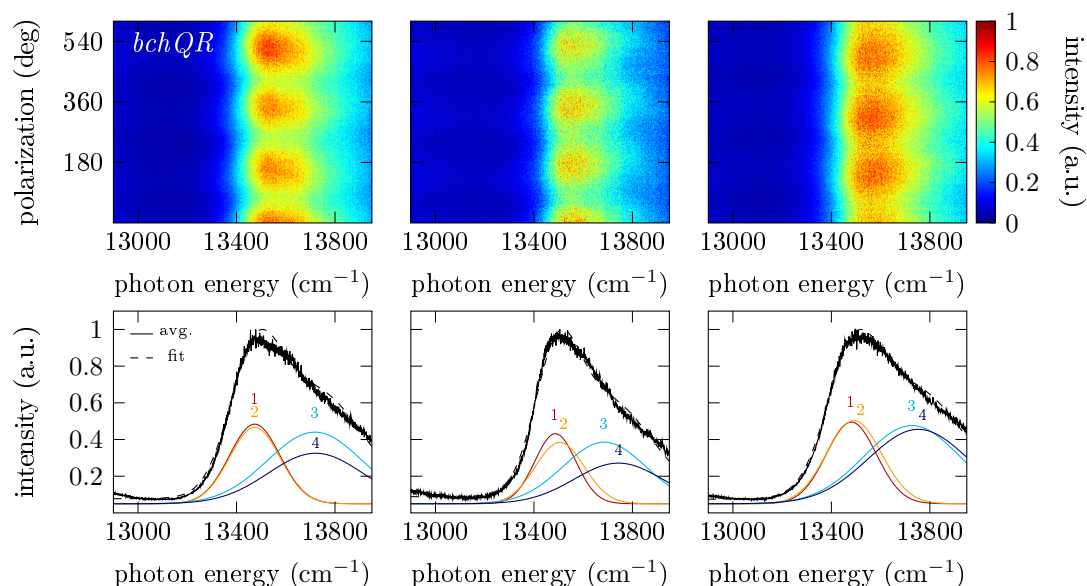
A.1.3 Spectra of the *bchQR* mutant

Figure A.3: Examples of polarization-resolved fluorescence-excitation spectra of individual chlorosomes from the *bchQR* mutant (spectra from figure 6.1) together with the spectra decomposed into four Gaussians.

A.2 Distribution of the relative phase angles $\Delta\Phi_{ij}$

A.2.1 Distribution of $\Delta\Phi_{ij}$ of the wild type

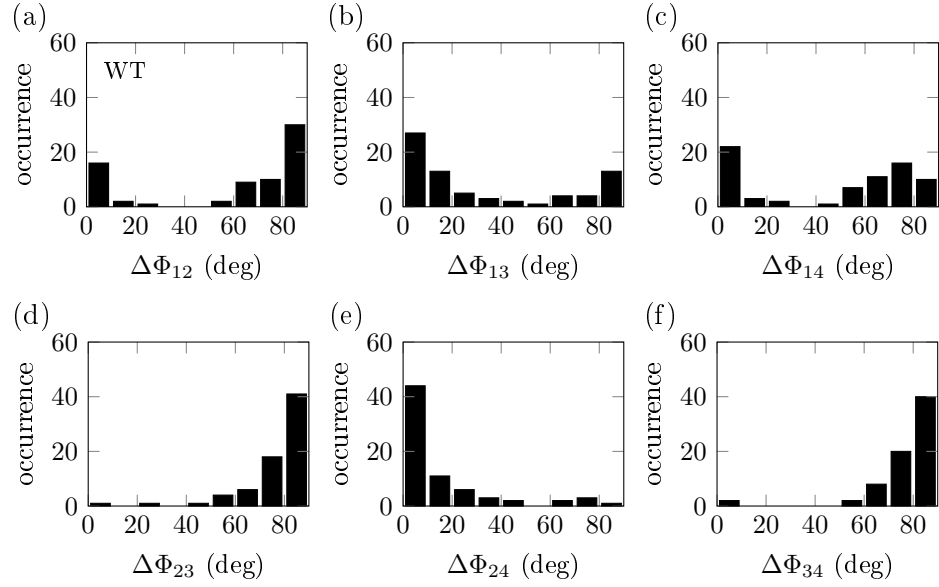


Figure A.4: Distributions of the relative phase angles $\Delta\Phi_{ij}$ of chlorosomes from the WT

A.2.2 Distribution of $\Delta\Phi_{ij}$ of the *bchR* mutant

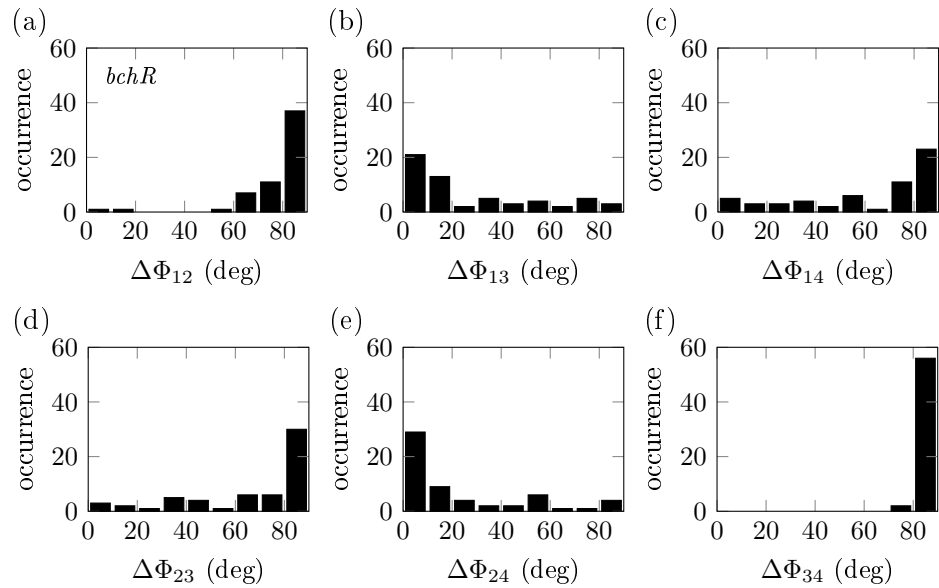


Figure A.5: Distributions of the relative phase angles $\Delta\Phi_{ij}$ of chlorosomes from the *bchR* mutant

A.2.3 Distribution of $\Delta\Phi_{ij}$ of the *bchQR* mutant

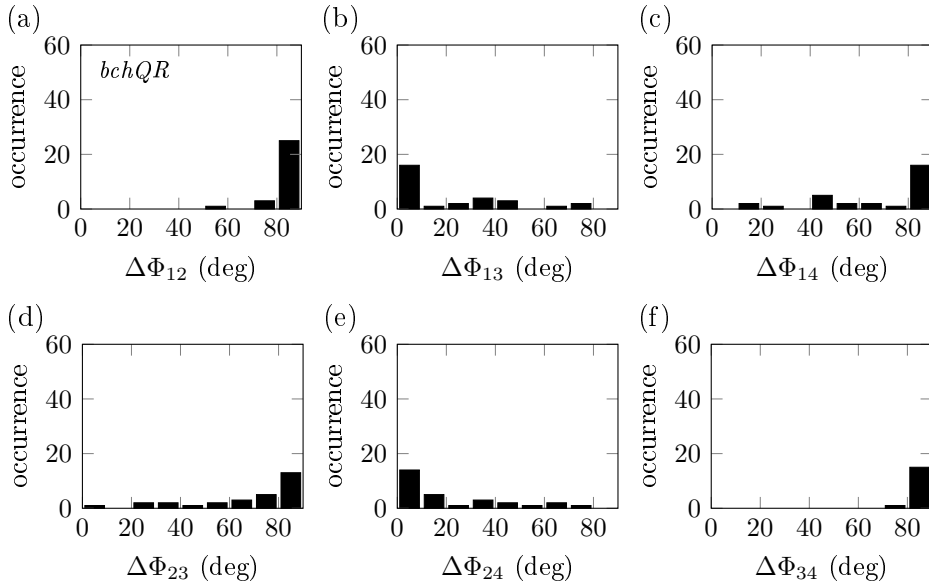


Figure A.6: Distributions of the relative phase angles $\Delta\Phi_{ij}$ of chlorosomes from the *bchQR* mutant

A.2.4 Distribution of $\Delta\Phi_{ij}$ of WT-group1

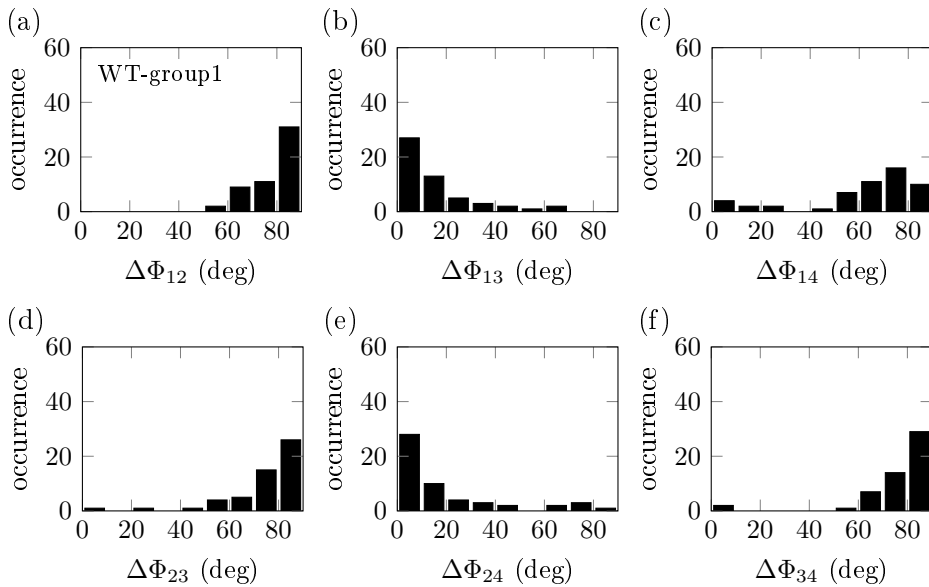


Figure A.7: Distributions of the relative phase angles $\Delta\Phi_{ij}$ of chlorosomes from WT-group1

A.2.5 Distribution of $\Delta\Phi_{ij}$ of WT-group2

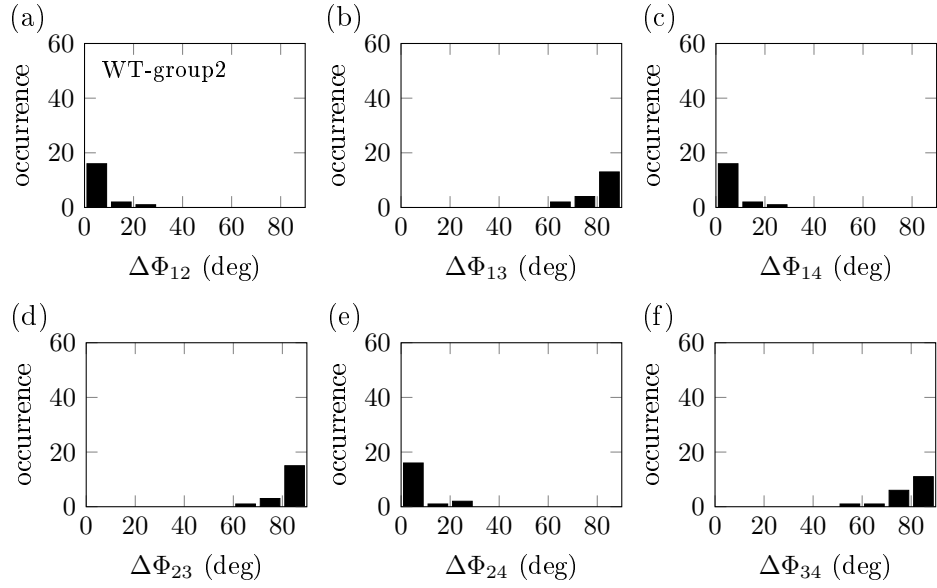


Figure A.8: Distributions of the relative phase angles $\Delta\Phi_{ij}$ of chlorosomes from WT-group2

A.2.6 Mean values and standard deviations of the distributions of the relative phase angles

Table A.1: Mean values (standard deviations) of the relative phase angles $\Delta\Phi_{ij}$ between the bands for the three types of chlorosomes.

$\Delta\Phi_{ij}$ (deg)	12	13	14	23	24	34
WT	60(34)	33(32)	47(33)	78(14)	16(20)	77(16)
WT-group1	79(10)	15(16)	63(24)	76(16)	19(22)	76(16)
WT-group2	6(5)	81(7)	4(4)	84(6)	6(7)	80(7)
<i>bchR</i>	78(16)	28(27)	62(28)	67(26)	23(26)	87(3)
<i>bchQR</i>	83(6)	17(27)	69(24)	68(22)	19(25)	88(3)

A.3 Stacking distances of *bchR* mutant chlorosomes from cryo-electron microscopy

Cryo-electron micrographs of *bchR* mutant chlorosomes appear rather similar to the ones from WT chlorosomes. The lamellar organization, indicated by the stripes in the direction of the long axis, appears somewhat less regular, suggesting more structural heterogeneity at the microscopic level (figure A.9a). Images of individual chlorosomes were analysed by Fourier transformation of boxed areas. In the derived power spectra equatorial reflections are visible, originating from the lamellar spacing (green arrow in figure A.9b). Although more fuzzy, the average lamellar spacing of 2.1 nm was the same as that found for the WT chlorosomes. A weak but significant layer line is present at $1/1.24\text{nm}^{-1}$ (red arrow), suggesting a helical arrangement of the BChls in which hetero (*syn-anti*) dimers are the building blocks of the chlorophyll stacks, again similar to WT chlorosomes. 16 power spectra as in figure A.9b were added after rotational alignment to illustrate the periodicity more clearly in figure A.9c.

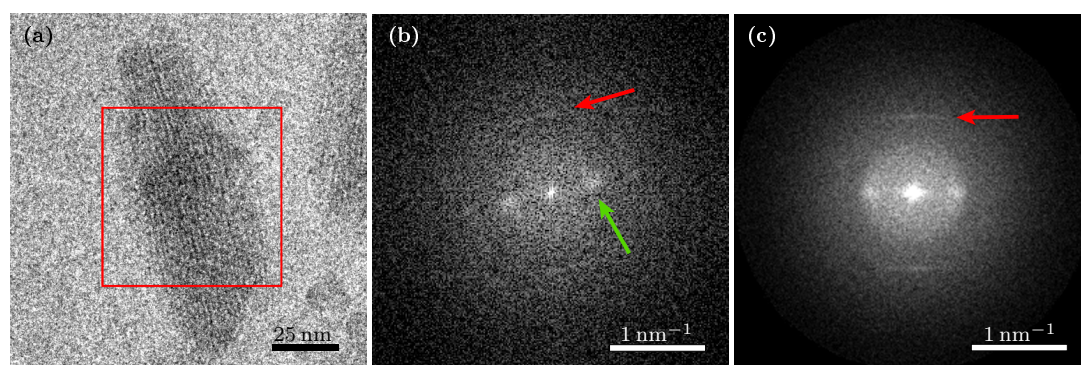


Figure A.9: (a) Cryo-electron micrograph of a *bchR* mutant chlorosome. (b) Power spectrum of the boxed area in (a). A green arrow points at the equatorial reflection originating from the lamellar spacing. The red arrow indicates the position of a layer line at $1/1.24\text{nm}^{-1}$. (c) Averaged power spectrum from 16 individual cryo-EM images of *bchR* mutant chlorosomes. The red arrow indicates the presence of a layerline at $1/1.24\text{ nm}^{-1}$. [2]

A.4 Correlations between the energetic separations of the spectral components

The correlation between the energetic separations ΔE_{ij} and ΔE_{kl} (for $i, j \neq k, l$) of the spectral components from the same individual chlorosome is shown in figure A.10. A significant correlation is only observable for the energy splittings ΔE_{12} vs. ΔE_{34} of the spectral components within the low- and the high-energy doublet (figure A.10a).

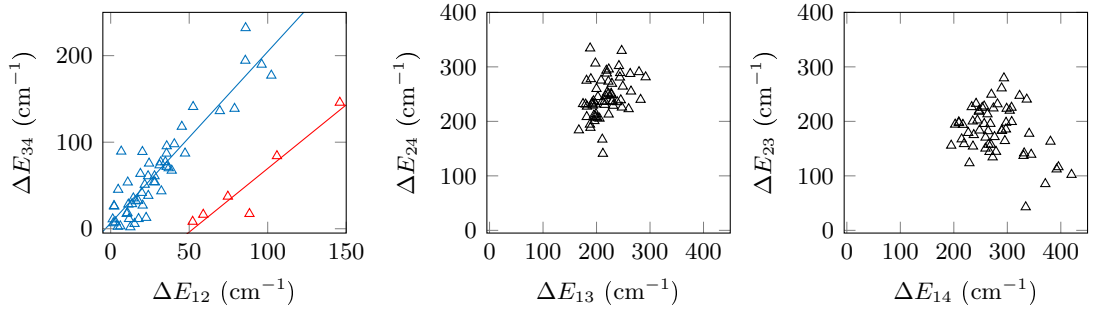


Figure A.10: Each cross corresponds to the energetic separations ΔE_{ij} and ΔE_{kl} (for $i, j \neq k, l$) of the spectral components of the same individual chlorosome from the *bchR* mutant. (a) ΔE_{12} vs. ΔE_{34} , i.e. between the spectral components within the low- and the high-energy doublet. The correlation coefficient for the full data set from 58 individual chlorosomes amounts to 0.7. If the data points marked in blue or red are treated separately the correlation coefficients are 0.93 (blue) and 0.95 (red), respectively. Both relations are reasonably well represented by a linear dependence. (b) ΔE_{13} vs. ΔE_{24} . The correlation coefficient amounts to 0.36. (c) ΔE_{14} vs. ΔE_{23} . The correlation coefficient amounts to 0.34. [2]

Two example spectra from chlorosomes that give rise to the data points marked in red in figure A.10a are shown in figure A.11. The setup of the figure is similar to that of figure 6.7. The fluorescence-excitation spectra of these chlorosomes showed “unusual” features compared to the spectra from the other chlorosomes. For some of them the emitted intensity drops to a low level during data acquisition (figures A.11a,b), whereas others display a pronounced shoulder on the high-energy side of the spectrum (A.11c,d). Some of these chlorosomes exhibit both in their spectra: a drop in intensity as well as a pronounced high-energy wing. In particular the high-energy spectral feature is tempting us to speculate whether the data points marked in blue and red in figure A.10a result from two structural elements that differ quantitatively in their pigment arrangement. However, at the current stage this remains an open question.

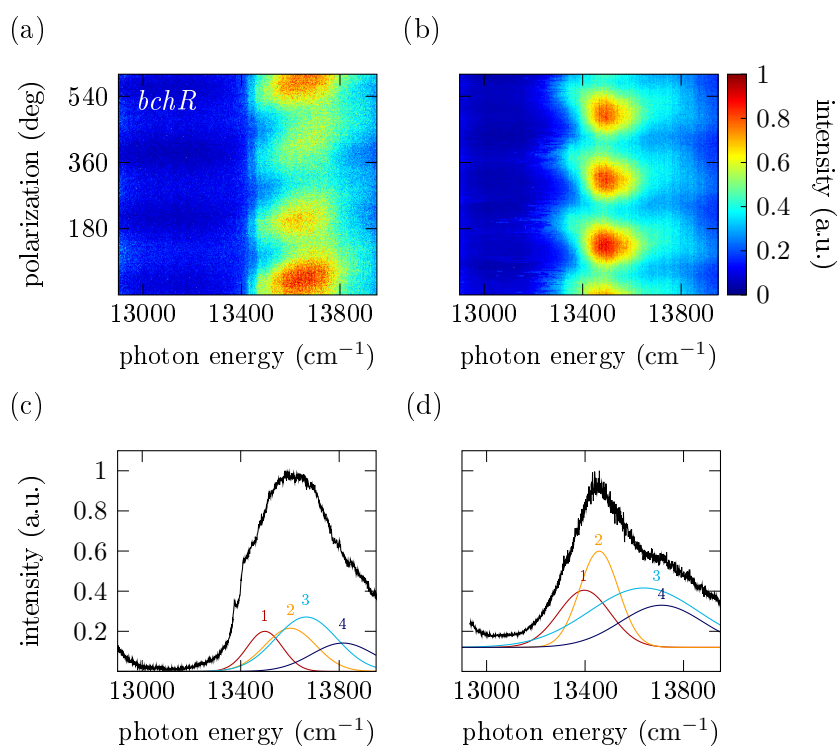


Figure A.11: Examples of spectra from individual chlorosomes that give rise to the data points marked in red in A.10a. The top panels a,c correspond each to a stack of 250 fluorescence-excitation spectra from one particular chlorosome as a function of the polarization of the excitation light. The spectra have been recorded at 1.5 K. At the bottom (b,d) the black lines correspond to the fluorescence-excitation spectra averaged over all polarisations, and the coloured lines represent the decomposition into four Gaussians. [2]

B Effect of misalignment of structures for polarization-resolved fluorescence-excitation and LD spectra

B.1 Polarization-resolved spectra

For the *bchQR* chlorosomes, in some cases, the cryo-EM images revealed secondary cylinder-like structures, whose symmetry axes were oriented mutually orthogonal with respect to each other [50]. In order to test the influence of a fraction of “misaligned” tubular structures within an individual chlorosomes on the optical spectra two extreme situations were modeled:

1. Symmetry axes of the cylinders perpendicular with respect to each other and perpendicular to the optical axis, see figure B.1

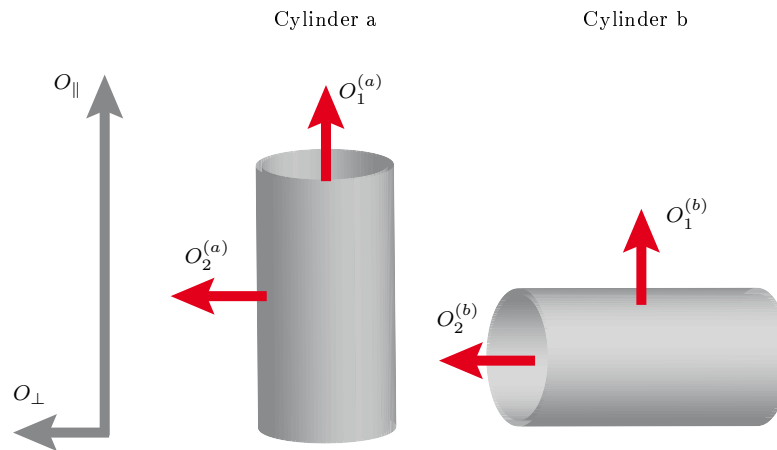


Figure B.1: Schematic illustration of mutually perpendicular oriented cylinder structures, where both symmetry axes are oriented perpendicular to the optical axis (perpendicular to the plane of the paper). The resulting polarizations of the allowed exciton transitions are indicated by the red arrows and the corresponding oscillator strengths are denoted by O . The grey axes set the reference frame which determines parallel (\parallel) and perpendicular (\perp) polarizations.

Without loss of generality it can be assumed that the majority of the secondary struc-

tures is oriented as cylinder a , which sets the reference frame (\parallel , \perp). Let n denote the fraction of structures oriented as cylinder a . Then the contributions to the overall oscillator strength are given as

$$O_{\parallel} = n O_1^{(a)} + (1 - n) O_1^{(b)} \quad (\text{B.1})$$

$$O_{\perp} = n O_2^{(a)} + (1 - n) O_2^{(b)} \quad (\text{B.2})$$

Under the reasonable assumption that the internal structures of the cylinders a and b are equivalent, this yields

$$O_2^{(a)} = O_1^{(b)} \quad \text{and} \quad O_1^{(a)} = O_2^{(b)} \quad (\text{B.3})$$

and

$$\frac{O_{\parallel}}{O_{\perp}} = \frac{n \left(O_1^{(a)} / O_2^{(a)} \right) + (1 - n)}{n + (1 - n) \left(O_1^{(a)} / O_2^{(a)} \right)} \quad (\text{B.4})$$

is found for the ratio of the measured oscillator strengths.

2. Symmetry axes of the cylinders perpendicular with respect to each other and one symmetry axis parallel to the optical axis, see figure B.2

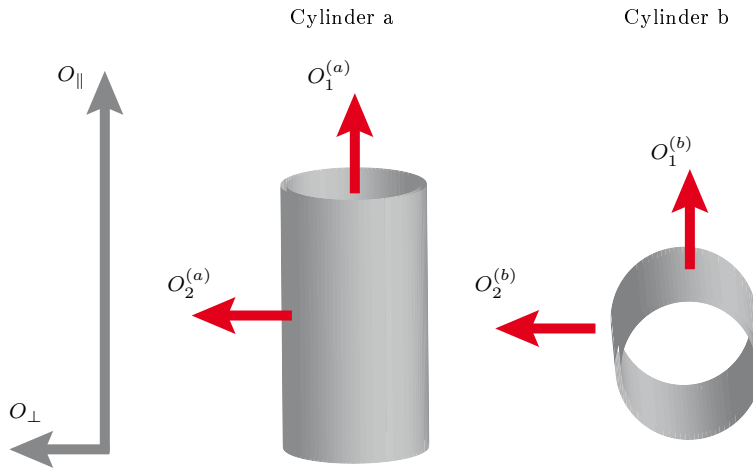


Figure B.2: Schematic illustration of mutually perpendicular oriented cylinder structures, where one symmetry axis is oriented perpendicular to the optical axis (perpendicular to the plane of the paper). The resulting polarizations of the allowed exciton transitions are indicated by the red arrows and the corresponding oscillator strengths are denoted by O . The grey axes set the reference frame which determines parallel (\parallel) and perpendicular (\perp) polarizations.

Under similar assumptions as above this yields

$$O_{\parallel} = n O_1^{(a)} + (1 - n) O_1^{(b)} \quad (\text{B.5})$$

$$O_{\perp} = n O_2^{(a)} + (1 - n) O_2^{(b)} \quad (\text{B.6})$$

and

$$O_2^{(a)} = O_1^{(b)} \quad \text{and} \quad O_2^{(b)} = O_1^{(a)} \quad (\text{B.7})$$

and finally

$$\frac{O_{\parallel}}{O_{\perp}} = n \frac{O_1^{(a)}}{O_2^{(a)}} + (1 - n) \quad (\text{B.8})$$

As detailed in chapter 6 the angle β between the monomer transition-dipole moments and the symmetry axis of the cylinder is given as

$$\beta = \arctan \sqrt{2 \frac{O_{\perp}}{O_{\parallel}}} \quad (\text{B.9})$$

From the cryo-EM data it can be deduced that the fraction of “misaligned” structures amounts at most to 10%, i.e., $n \geq 0.9$. Figure B.3 shows the variation of β as a function of the fraction n of “properly oriented” cylinders for both scenarios for the range $n = 1$ to $n = 0.5$. For the range of interest, i.e. $n \geq 0.9$, and $0.75 \leq O_1/O_2 \leq 1.25$, which covers the bulk of the experimental data, the variation of β amounts to a few degrees.

Nevertheless, it cannot be excluded that those “misaligned” secondary structures that have been observed in cryo-EM in the chlorosomes of the *bchQR* mutant, contribute to a small extent also to the widths of the distributions shown in figure 6.11.

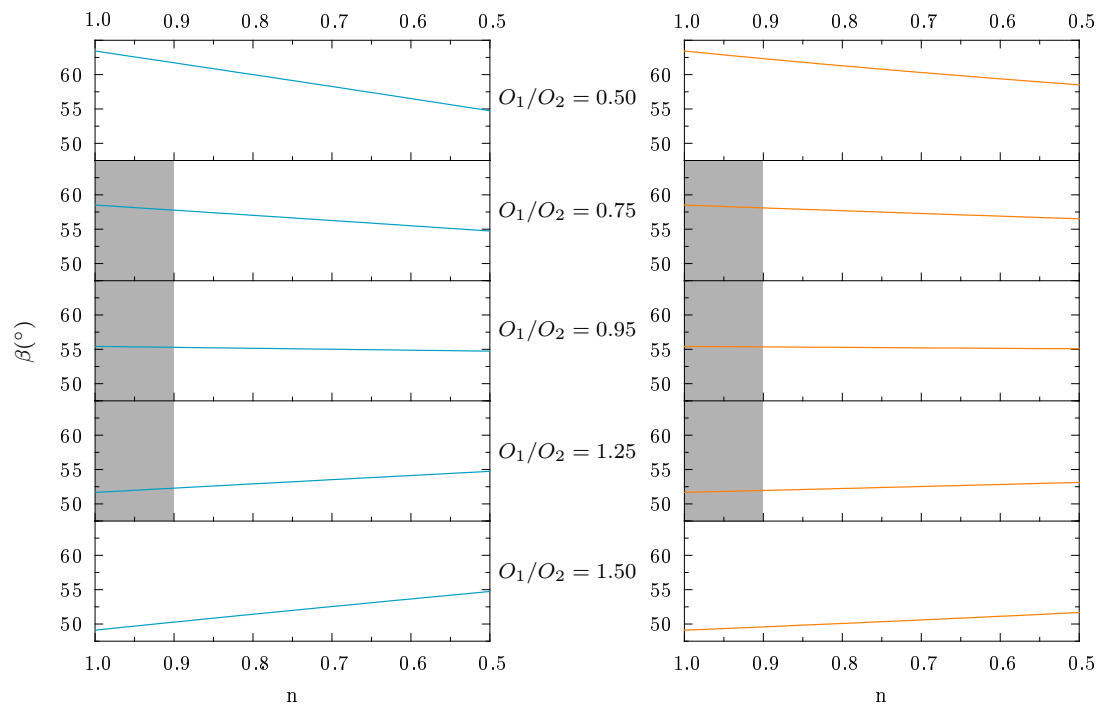


Figure B.3: Variation of the angle β as a function of n and as a function of the ratio of the oscillator strengths. The left-hand side refers to situation 1 (figure B.1) and the right hand side refers to situation 2 (figure B.2). The grey area refers to the parameter range that is relevant for this work.

B.2 LD spectra

The LD spectra presented in figure 6.12 are reconstructed from the polarization-resolved spectra in a way that they represent a perfect alignment of the chlorosome with respect to the parallel and perpendicular polarization of the excitation light. The influence of the misalignment on the LD spectra is investigated by studying a single cylinder, as schematically depicted in figure B.4.

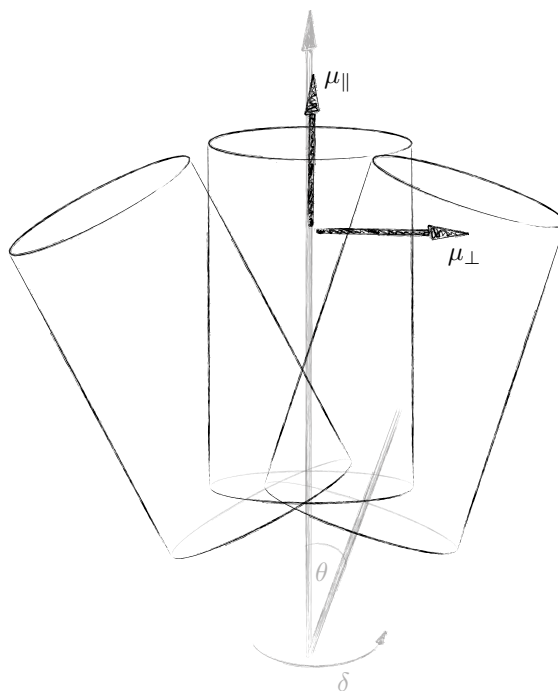


Figure B.4: Schematic illustration of a cylinder with its transition dipole moments μ_{\parallel} and μ_{\perp} . Parallel to the long axis of the middle cylinder (grey) the reference axis of perfect alignment is shown. The two cylinders sideways inclined represent misaligned cylinders with an inclination θ with respect to the reference axis and a rotation of δ around the axis.

The LD spectrum of a perfectly aligned single cylinder arises from absorption spectra with a polarization of the excitation light parallel to the long axis of the cylinder (grey) and perpendicular to it. The LD spectrum can be influenced by an inclination of the cylinder of θ with respect to the long axis of the perfectly aligned cylinder and a rotation δ around this axis. For cylinders, which are not perfectly aligned, the LD spectrum is:

$$LD \sim (A_{\parallel} - A_{\perp}) = |\mu_i^2| \left(\sum_i \cos^2 \theta_i - \sum_i \sin^2 \theta_i \right) \quad (\text{B.10})$$

The effect of θ on the LD spectrum of an individual cylinder was studied by simulating

polarization-resolved of individual cylinders, as in section 7.2. The LD spectra were then reconstructed using an angle $\Phi_{\parallel, \text{mis}}$, which is slightly changed from the angle Φ_{\parallel} by an angle of misalignment θ .

$$\Phi_{\parallel, \text{mis}} = \Phi_{\parallel} \pm \theta \quad (\text{B.11})$$

The angle $\Phi_{\perp, \text{mis}}$ is chosen perpendicular to $\Phi_{\parallel, \text{mis}}$. In figure B.5 shows the LD signal of a single cylinder with an angle $\theta = 0^\circ, 15^\circ, 30^\circ, 45^\circ, 60^\circ$ to the axis of perfect alignment. The LD signal decreases as a result of a disorientation from this axis. At an angle $\theta = 45^\circ$ the sign of the LD bands changes.

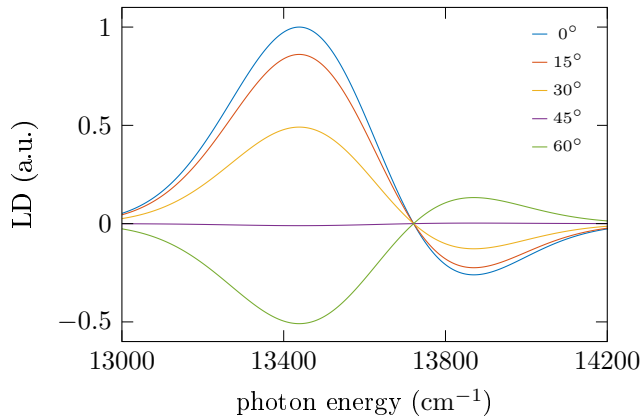


Figure B.5: LD spectra of a simulated cylindrical arrangement of BChls. The different spectra result from a disorientation of the cylinder with respect to the perfectly aligned reference axis.

The misalignment of chlorosomes in an ensemble can be studied in a similar way. The LD spectrum of an ensemble with perfectly aligned chlorosomes is presented in figure B.6. The angle θ of misalignment equals zero. For individual chlorosomes a misalignment of a random angle θ in the range from -15° to 15° (-30° to 30° , and -60° to 60°) is now chosen. The ensemble LD spectrum results from the average of the 66 LD spectra of individual chlorosomes with a random degree of misalignment θ . The spectra in figure B.6 show that the LD signal is decreased by a higher factor of misalignment. Furthermore, the noise remains the same for all spectra and the signal to noise ratio gets worse with a lower degree of orientation of the chlorosomes.

It has to be noted that the ensemble LD spectra are not only influenced by a misalignment of the chlorosomes with respect to the polarization of the excitation light. As an individual chlorosome itself represents an ensemble of not perfectly aligned individual cylindrical structures, the LD spectrum of an individual chlorosome is already obstructed by the orientation of the aggregated structures.

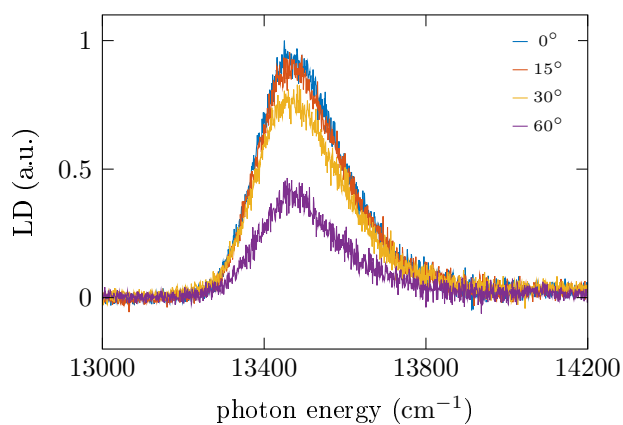


Figure B.6: Ensemble LD spectra with a variation of the orientation of the chlorosomes with respect to the perfect orientation. The ensemble spectrum from figure 6.12 is shown in blue for the perfect orientation with 0° with respect to the axis of perfect alignment. For the other spectra for each of the 66 spectra a random degree of misalignment was chosen in the range from -15° to 15° (-30° to 30° , -60° to 60°).

References

1. Ganapathy, S., Oostergetel, G. T., Wawrzyniak, P. K., Reus, M., Gomez Maqueo Chew, A., Buda, F., Boekema, E. J., Bryant, D. A., Holzwarth, A. R. & de Groot, H. J. M. Alternating syn-anti bacteriochlorophylls form concentric helical nanotubes in chlorosomes. *Proceedings of the National Academy of Sciences of the United States of America* **106**, 8525–8530 (2009).
2. Günther, L. M., Jendryny, M., Bloemsma, E. A., Tank, M., Oostergetel, G. T., Bryant, D. A., Knoester, J. & Köhler, J. Structure of Light-Harvesting Aggregates in Individual Chlorosomes. *The Journal of Physical Chemistry B* **120**, 5367–5376 (2016).
3. Günther, L. M., Löhner, A., Reiher, C., Kunsel, T., Jansen, T. L. C., Tank, M., Bryant, D. A., Knoester, J. & Köhler, J. Structural Variations in Chlorosomes from Wild-Type and a bchQR Mutant of *Chlorobaculum tepidum* Revealed by Single-Molecule Spectroscopy. *The Journal of Physical Chemistry B* **122**, 6712–6723 (2018).
4. Wohlrab, L. M. *Spektroskopie einzelner Lichtsammelkomplexe von grünen Schwefelbakterien* Master Thesis (Universität Bayreuth, Bayreuth, 2013).
5. Helmholtz, H. v. *Über die Erhaltung der Kraft* (Humboldt-Universität zu Berlin, 1847).
6. Huxley, T. H. & Huxley, A. *Scientific memoirs, selected from the transactions of foreign academies of science, and from foreign journals. Natural history. Ed. by Arthur Huxley and Thomas Henry Huxley* (Taylor and Francis, London, 1853).
7. IEA. *World Energy Outlook 2019* (ed IEA) Paris, 2019.
8. Quaschnig, V. *Erneuerbare Energien und Klimaschutz: Hintergründe, Technik und Planung, Ökonomie und Ökologie, Energiewende* 4., überarbeitete und erweiterte Auflage (Hanser, München, 2018).
9. Rothschild, L. J. & Mancinelli, R. L. Life in extreme environments. *Nature* **409**, 1092–1101 (2001).

10. Beatty, J. T., Overmann, J., Lince, M. T., Manske, A. K., Lang, A. S., Blankenship, R. E., van Dover, C. L., Martinson, T. A. & Plumley, F. G. An obligately photosynthetic bacterial anaerobe from a deep-sea hydrothermal vent. *Proceedings of the National Academy of Sciences of the United States of America* **102**, 9306–9310 (2005).
11. Moerner, W. E. in *Single Molecule Spectroscopy in Chemistry, Physics and Biology: Nobel Symposium* (eds Gräslund, A., Rigler, R. & Widengren, J.) 25–60 (Springer Berlin Heidelberg, Berlin, Heidelberg, 2010).
12. Otsuki, J. Supramolecular approach towards light-harvesting materials based on porphyrins and chlorophylls. *Journal of Materials Chemistry A* **6**, 6710–6753 (2018).
13. *Botanik: [fit für den Bachelor]* (ed Munk, K.) (Thieme, Stuttgart, 2009).
14. Cogdell, R. J., Isaacs, N. W., Howard, T. D., McLuskey, K., Fraser, N. J. & Prince, S. M. How photosynthetic bacteria harvest solar energy. *Journal of Bacteriology* **181**, 3869–3879 (1999).
15. Govindjee & Shevela, D. Adventures with cyanobacteria: a personal perspective. *Frontiers in plant science* **2**, 28 (2011).
16. Frigaard, N.-U. & Bryant, D. A. in *Complex Intracellular Structures in Prokaryotes* (ed Shively, J. M.) 79–114 (Springer Berlin Heidelberg, Berlin, Heidelberg, 2006).
17. Bryant, D. A. *et al.* Candidatus Chloracidobacterium thermophilum: an aerobic phototrophic Acidobacterium. *Science (New York, N.Y.)* **317**, 523–526 (2007).
18. Weiler, E. W. & Nover, L. *Allgemeine und molekulare Botanik* 1. Aufl. (Thieme, Stuttgart, 2008).
19. Brinkert, K. *Energy conversion in natural and artificial photosynthesis* (Springer).
20. Dersch, P., Eikmanns, B., Eikmanns, M., Fischer, R., Jahn, D., Jahn, M., Nethe-Jaenchen, R., Requena, N. & Schultze, B. *Mikrobiologie: 381 Abbildungen und 43 Tabellen* 2., unveränderte Auflage (Georg Thieme Verlag, Stuttgart and New York, 2018).
21. Pierson, B. K. & Castenholz, R. W. A phototrophic gliding filamentous bacterium of hot springs, *Chloroflexus aurantiacus*, gen. and sp. nov. *Archives of microbiology* **100**, 5–24 (1974).
22. Sprague, S. G., Staehelin, L. A., DiBartolomeis, M. J. & Fuller, R. C. Isolation and development of chlorosomes in the green bacterium *Chloroflexus aurantiacus*. *Journal of bacteriology* **147**, 1021–1031 (1981).
23. Oelze, J. & Fuller, R. C. Temperature dependence of growth and membrane-bound activities of *Chloroflexus aurantiacus* energy metabolism. *Journal of bacteriology* **155**, 90–96 (1983).

24. Wahlund, T. M., Woese, C. R., Castenholz, R. W. & Madigan, M. T. A thermophilic green sulfur bacterium from New Zealand hot springs, *Chlorobium tepidum* sp. nov. *Archives of Microbiology* **156**, 81–90 (1991).
25. Eisen, J. A. *et al.* The complete genome sequence of *Chlorobium tepidum* TLS, a photosynthetic, anaerobic, green-sulfur bacterium. *Proceedings of the National Academy of Sciences of the United States of America* **99**, 9509–9514 (2002).
26. Crowe, S. A. *et al.* Photoferrotrophs thrive in an Archean Ocean analogue. *Proceedings of the National Academy of Sciences of the United States of America* **105**, 15938–15943 (2008).
27. Smith, K. M., Kehres, L. A. & Fajer, J. Aggregation of the bacteriochlorophylls c, d, and e. Models for the antenna chlorophylls of green and brown photosynthetic bacteria. *Journal of the American Chemical Society* **105**, 1387–1389 (1983).
28. Bystrova, M. I., Mal'gosheva, I. N. & Krasnovskii, A. A. Molecular mechanism of self-assembly of aggregated bacteriochlorophyll c. *Molekuliarnaia biologii* **13**, 582–594 (1979).
29. Fenna, R. E. & Matthews, B. W. Chlorophyll arrangement in a bacteriochlorophyll protein from *Chlorobium limicola*. *Nature* **258**, 573–577 (1975).
30. Olson, J. M. & Romano, C. A. A new chlorophyll from green bacteria. *Biochimica et Biophysica Acta* **59**, 726–728 (1962).
31. Oelze, J. & Golecki, J. R. in *Anoxygenic Photosynthetic Bacteria* (eds Blankenship, R. E., Madigan, M. T. & Bauer, C. E.) (Kluwer Academic Publishers, Dordrecht, 1995).
32. Cohen-Bazire, G., Pfennig, N. & Kunisawa, R. The fine structure of green bacteria. *The Journal of cell biology* **22**, 207–225 (1964).
33. Olson, J. M. Chlorophyll Organization and Function in Green Photosynthetic Bacteria. *Photochemistry and Photobiology* **67**, 61–75 (1998).
34. Montaña, G. A., Bowen, B. P., LaBelle, J. T., Woodbury, N. W., Pizziconi, V. B. & Blankenship, R. E. Characterization of *Chlorobium tepidum* Chlorosomes: A Calculation of Bacteriochlorophyll c per Chlorosome and Oligomer Modeling. *Biophysical Journal* **85**, 2560–2565 (2003).
35. Blankenship, R. E., Olson, J. M. & Miller, M. in *Anoxygenic Photosynthetic Bacteria* (eds Blankenship, R. E., Madigan, M. T. & Bauer, C. E.) 399–435 (Kluwer Academic Publishers, Dordrecht, 1995).
36. Frigaard, N.-U., Larsen, K. L. & Cox, R. P. Spectrochromatography of photosynthetic pigments as a fingerprinting technique for microbial phototrophs. *FEMS Microbiology Ecology* **20**, 69–77 (1996).

37. Frigaard, N.-U., Chew, A. G. M., Li, H., Maresca, J. A. & Bryant, D. A. Chlorobium tepidum: insights into the structure, physiology, and metabolism of a green sulfur bacterium derived from the complete genome sequence. *Photosynthesis Research* **78**, 93–117 (2003).
38. Blankenship, R. E. *Molecular mechanisms of photosynthesis* 2. ed. (Wiley Blackwell, Chichester, 2014).
39. Overmann, J., Cypionka, H. & Pfennig, N. An extremely low-light adapted phototrophic sulfur bacterium from the Black Sea. *Limnology and Oceanography* **37**, 150–155 (1992).
40. Cruden, D. L. & Stanier, R. Y. The characterization of chlorobium vesicles and membranes isolated from green bacteria. *Archives of Microbiology* **72**, 115–134 (1970).
41. Staehelin, L. A., Golecki, J. R., Fuller, R. C. & Drews, G. Visualization of the supramolecular architecture of chlorosomes (chlorobium type vesicles) in freeze-fractured cells of Chloroflexus aurantiacus. *Archives of Microbiology* **119**, 269–277 (1978).
42. van Dorssen, R. J., Vasmel, H. & Amesz, J. Pigment organization and energy transfer in the green photosynthetic bacterium Chloroflexus aurantiacus: II. The chlorosome. *Photosynthesis Research* **9**, 33–45 (1986).
43. Prokhorenko, V. I., Steensgaard, D. B. & Holzwarth, A. R. Exciton Dynamics in the Chlorosomal Antennae of the Green Bacteria Chloroflexus aurantiacus and Chlorobium tepidum. *Biophysical Journal* **79**, 2105–2120 (2000).
44. van Rossum, B.-J., Steensgaard, D. B., Mulder, F. M., Boender, G. J., Schaffner, K., Holzwarth, A. R. & de Groot, H. J. M. A Refined Model of the Chlorosomal Antennae of the Green Bacterium Chlorobium tepidum from Proton Chemical Shift Constraints Obtained with High-Field 2-D and 3-D MAS NMR Dipolar Correlation Spectroscopy. *Biochemistry* **40**, 1587–1595 (2001).
45. Pšenčík, J., Ikonen, T. P., Laurinmaki, P., Merckel, M. C., Butcher, S. J., Serimaa, R. E. & Tuma, R. Lamellar organization of pigments in chlorosomes, the light harvesting complexes of green photosynthetic bacteria. *Biophysical Journal* **87**, 1165–1172 (2004).
46. Pšenčík, J., Butcher, S. J. & Tuma, R. in *The Structural Basis of Biological Energy Generation* (ed Hohmann-Marriott, M. F.) 77–109 (Springer Netherlands, Dordrecht, 2014).
47. Shibata, Y., Saga, Y., Tamiaki, H. & Itoh, S. Low-Temperature Fluorescence from Single Chlorosomes, Photosynthetic Antenna Complexes of Green Filamentous and Sulfur Bacteria. *Biophysical Journal* **91**, 3787–3796 (2006).

-
48. Jendryny, M., Aartsma, T. J. & Köhler, J. Fluorescence Excitation Spectra from Individual Chlorosomes of the Green Sulfur Bacterium *Chlorobaculum tepidum*. *The Journal of Physical Chemistry Letters* **3**, 3745–3750 (2012).
 49. Jendryny, M., Aartsma, T. J. & Köhler, J. Insights into the excitonic states of individual chlorosomes from *Chlorobaculum tepidum*. *Biophysical Journal* **106**, 1921–1927 (2014).
 50. Ganapathy, S., Oostergetel, G. T., Reus, M., Tsukatani, Y., Gomez Maqueo Chew, A., Buda, F., Bryant, D. A., Holzwarth, A. R. & de Groot, H. J. M. Structural Variability in Wild-Type and bchQ bchR Mutant Chlorosomes of the Green Sulfur Bacterium *Chlorobaculum tepidum*. *Biochemistry* **51**, 4488–4498 (2012).
 51. Martiskainen, J., Linnanto, J., Aumanen, V., Myllyperkio, P. & Korppi-Tommola, J. E. I. Excitation energy transfer in isolated chlorosomes from *Chlorobaculum tepidum* and *Prosthecochloris aestuarii*. *Photochemistry and Photobiology* **88**, 675–683 (2012).
 52. Linnanto, J. M. & Korppi-Tommola, J. E. I. Exciton Description of Chlorosome to Baseplate Excitation Energy Transfer in Filamentous Anoxygenic Phototrophs and Green Sulfur Bacteria. *The Journal of Physical Chemistry B* **117**, 11144–11161 (2013).
 53. Staehelin, L. A., Golecki, J. R. & Drews, G. Supramolecular organization of chlorosomes (chlorobium vesicles) and of their membrane attachment sites in *Chlorobium limicola*. *Biochimica et Biophysica Acta* **589**, 30–45 (1980).
 54. Holzwarth, A. R., Griebenow, K. & Schaffner, K. Chlorosomes, photosynthetic antennae with novel self-organized pigment structures. *Journal of Photochemistry and Photobiology A: Chemistry* **65**, 61–71 (1992).
 55. Holzwarth, A. R. & Schaffner, K. On the structure of bacteriochlorophyll molecular aggregates in the chlorosomes of green bacteria. A molecular modelling study. *Photosynthesis Research* **41**, 225–233 (1994).
 56. Oostergetel, G. T., Reus, M., Gomez Maqueo Chew, A., Bryant, D. A., Boekema, E. J. & Holzwarth, A. R. Long-range organization of bacteriochlorophyll in chlorosomes of *Chlorobium tepidum* investigated by cryo-electron microscopy. *FEBS Letters* **581**, 5435–5439 (2007).
 57. Alster, J., Kabeláč, M., Tuma, R., Pšenčík, J. & Burda, J. V. Computational study of short-range interactions in bacteriochlorophyll aggregates. *Computational and Theoretical Chemistry* **998**, 87–97 (2012).

58. Furumaki, S., Vacha, F., Habuchi, S., Tsukatani, Y., Bryant, D. A. & Vacha, M. Absorption linear dichroism measured directly on a single light-harvesting system: the role of disorder in chlorosomes of green photosynthetic bacteria. *Journal of the American Chemical Society* **133**, 6703–6710 (2011).
59. Tian, Y., Camacho, R., Thomsson, D., Reus, M., Holzwarth, A. R. & Scheblykin, I. G. Organization of Bacteriochlorophylls in Individual Chlorosomes from *Chlorobaculum tepidum* Studied by 2-Dimensional Polarization Fluorescence Microscopy. *Journal of the American Chemical Society* **133**, 17192–17199 (2011).
60. Saga, Y., Wazawa, T., Ishii, Y., Yanagida, T. & Tamiaki, H. Single Supramolecule Spectroscopy of Natural and Alkaline-Treated Chlorosomes from Green Sulfur Photosynthetic Bacteria. *Journal of Nanoscience and Nanotechnology* **6**, 1750–1757 (2006).
61. Egawa, A., Fujiwara, T., Mizoguchi, T., Kakitani, Y., Koyama, Y. & Akutsu, H. Structure of the light-harvesting bacteriochlorophyll c assembly in chlorosomes from *Chlorobium limicola* determined by solid-state NMR. *Proceedings of the National Academy of Sciences of the United States of America* **104**, 790–795 (2007).
62. Knoester, J. & Agranovich, V. M. in *Electronic excitations in organic based nanostructures* (eds Bassani, F. G. & Agranovich, V. M.) 1–96 (Elsevier, Amsterdam, 2003).
63. Förster, T. Zwischenmolekulare Energiewanderung und Fluoreszenz. *Annalen der Physik* **437**, 55–75 (2006).
64. Frenkel, J. On the Transformation of light into Heat in Solids. I. *Physical Review* **37**, 17–44 (1931).
65. Frenkel, J. On the Transformation of Light into Heat in Solids. II. *Physical Review* **37**, 1276–1294 (1931).
66. Davydov, A. S. *Theory of Molecular Excitons* (Plenum Press, New York, 1971).
67. Hesse, M., Meier, H. & Zeeh, B. *Spektroskopische Methoden in der organischen Chemie: 102 Tabellen* 7., überarb. Aufl. (Thieme, Stuttgart, 2005).
68. Jelley, E. E. Spectral Absorption and Fluorescence of Dyes in the Molecular State. *Nature* **138**, 1009–1010 (1936).
69. Scheibe, G., Kandler, L. & Ecker, H. Polymerisation und polymere Adsorption als Ursache neuartiger Absorptionsbanden von organischen Farbstoffen. *Die Naturwissenschaften* **25**, 75 (1937).
70. Scheibe, G. Über die Veränderlichkeit der Absorptionsspektren in Lösungen und die Nebenvalenzen als ihre Ursache. *Angewandte Chemie* **50**, 212–219 (1937).

-
71. Brixner, T., Hildner, R., Köhler, J., Lambert, C. & Würthner, F. Exciton Transport in Molecular Aggregates - From Natural Antennas to Synthetic Chromophore Systems. *Advanced Energy Materials* **5**, 1700236 (2017).
 72. Knoester, J. in *Organic nanostructures* (eds Agranovich, V. M. & La Rocca, G. C.) (IOS Press, Amsterdam and Washington, D.C., 2002).
 73. Knapp, E. W. Lineshapes of molecular aggregates, exchange narrowing and intersite correlation. *Chemical Physics* **85**, 73–82 (1984).
 74. Didraga, C. & Knoester, J. Exchange narrowing in circular and cylindrical molecular aggregates: Degenerate versus nondegenerate states. *Chemical Physics* **275**, 307–318 (2002).
 75. Didraga, C., Klugkist, J. A. & Knoester, J. Optical Properties of Helical Cylindrical Molecular Aggregates: The Homogeneous Limit. *The Journal of Physical Chemistry B* **106**, 11474–11486 (2002).
 76. Didraga, C. & Knoester, J. Absorption and dichroism spectra of cylindrical J aggregates and chlorosomes of green bacteria. *Journal of Luminescence* **102-103**, 60–66 (2003).
 77. Didraga, C., Pugžlys, A., Hania, P. R., von Berlepsch, H., Duppen, K. & Knoester, J. Structure, Spectroscopy, and Microscopic Model of Tubular Carbocyanine Dye Aggregates. *The Journal of Physical Chemistry B* **108**, 14976–14985 (2004).
 78. Didraga, C. & Knoester, J. Optical spectra and localization of excitons in inhomogeneous helical cylindrical aggregates. *The Journal of chemical physics* **121**, 10687–10698 (2004).
 79. Didraga, C. & Knoester, J. Chiral exciton wave functions in cylindrical J aggregates. *The Journal of chemical physics* **121**, 946–959 (2004).
 80. Vassilieva, E. V., Stirewalt, V. L., Jakobs, C. U., Frigaard, N.-U., Inoue-Sakamoto, K., Baker, M. A., Sotak, A. & Bryant, D. A. Subcellular Localization of Chlorosome Proteins in *Chlorobium tepidum* and Characterization of Three New Chlorosome Proteins: CsmF, CsmH, and CsmX. *Biochemistry* **41**, 4358–4370 (2002).
 81. Frigaard, N.-U., Voigt, G. D. & Bryant, D. A. *Chlorobium tepidum* mutant lacking bacteriochlorophyll c made by inactivation of the bchK gene, encoding bacteriochlorophyll c synthase. *Journal of bacteriology* **184**, 3368–3376 (2002).
 82. Shibata, Y., Saga, Y., Tamiaki, H. & Itoh, S. Anisotropic distribution of emitting transition dipoles in chlorosome from *Chlorobium tepidum*: fluorescence polarization anisotropy study of single chlorosomes. *Photosynthesis Research* **100**, 67–78 (2009).

83. Balaban, T. S. Tailoring Porphyrins and Chlorins for Self-Assembly in Biomimetic Artificial Antenna Systems. *Accounts of Chemical Research* **38**, 612–623 (2005).
84. Sengupta, S. *et al.* Biosupramolecular nanowires from chlorophyll dyes with exceptional charge-transport properties. *Angewandte Chemie International Edition in English* **51**, 6378–6382 (2012).
85. Eisele, D. M. *et al.* Robust excitons inhabit soft supramolecular nanotubes. *Proceedings of the National Academy of Sciences of the United States of America* **111**, E3367–75 (2014).
86. Tamiaki, H. Supramolecular structure in extramembraneous antennae of green photosynthetic bacteria. *Coordination Chemistry Reviews* **148**, 183–197 (1996).
87. Chew, A. G. M., Frigaard, N.-U. & Bryant, D. A. Bacteriochlorophyllide c C-8² and C-12¹ Methyltransferases Are Essential for Adaptation to Low Light in *Chlorobaculum tepidum*. *Journal of Bacteriology* **189**, 6176–6184 (2007).
88. Eisele, D. M., Cone, C. W., Bloemsma, E. A., Vlaming, S. M., van der Kwaak, C. G. F., Silbey, R. J., Bawendi, M. G., Knoester, J., Rabe, J. P. & Vanden Bout, D. A. Utilizing redox-chemistry to elucidate the nature of exciton transitions in supramolecular dye nanotubes. *Nature Chemistry* **4**, 655–662 (2012).
89. Linnanto, J. M. & Korppi-Tommola, J. E. I. Investigation on chlorosomal antenna geometries: tube, lamella and spiral-type self-aggregates. *Photosynthesis Research* **96**, 227–245 (2008).
90. Lampoura, S. S., Spitz, C., Dähne, S., Knoester, J. & Duppen, K. The Optical Dynamics of Excitons in Cylindrical J-Aggregates. *The Journal of Physical Chemistry B* **106**, 3103–3111 (2002).
91. Oostergetel, G. T., van Amerongen, H. & Boekema, E. J. The chlorosome: a prototype for efficient light harvesting in photosynthesis. *Photosynthesis Research* **104**, 245–255 (2010).
92. Furumaki, S., Habuchi, S. & Vacha, M. Fluorescence-detected three-dimensional linear dichroism: A method to determine absorption anisotropy in single sub-wavelength size nanoparticles. *Chemical Physics Letters* **487**, 312–314 (2010).
93. van Amerongen, H., Vasmel, H. & van Grondelle, R. Linear Dichroism of Chlorosomes from *Chloroflexus Aurantiacus* in Compressed Gels and Electric Fields. *Biophysical Journal* **54**, 65–76 (1988).

-
94. Griebenow, K., Holzwarth, A. R., van Mourik, F. & van Grondelle, R. Pigment organization and energy transfer in green bacteria. 2. Circular and linear dichroism spectra of protein-containing and protein-free chlorosomes isolated from *Chloroflexus aurantiacus* strain Ok-70-fl. *Biochimica et Biophysica Acta - Bioenergetics* **1058**, 194–202 (1991).
 95. Frese, R., Oberheide, U., van Stokkum, I., van Grondelle, R., Foidl, M., Oelze, J. & van Amerongen, H. The organization of bacteriochlorophyll c in chlorosomes from *Chloroflexus aurantiacus* and the structural role of carotenoids and protein. *Photosynthesis Research* **54**, 115–126 (1997).
 96. Bloemsmma, E. A., Vlaming, S. M., Malyshev, V. A. & Knoester, J. Signature of Anomalous Exciton Localization in the Optical Response of Self-Assembled Organic Nanotubes. *Physical Review Letters* **114** (2015).
 97. Löhner, A., Kunsel, T., Röhr, M. I. S., Jansen, T. L. C., Sengupta, S., Würthner, F., Knoester, J. & Köhler, J. Spectral and Structural Variations of Biomimetic Light-Harvesting Nanotubes. *The Journal of Physical Chemistry Letters* **10**, 2715–2724.
 98. Li, X., Buda, F., de Groot, H. J. M. & Sevink, G. J. A. Molecular Insight in the Optical Response of Tubular Chlorosomal Assemblies. *The Journal of Physical Chemistry C*, 16462–16478 (2019).

Danksagung

“ *There’s a lot of things you need to get across this universe. Warp drive... wormhole refractors... You know the thing you need most of all? You need a hand to hold.* THE DOCTOR ”

Danke für eure Hände.

An erster Stelle gilt mein Dank dir, Jürgen. Während meiner Masterarbeit hast du mir das Vertrauen gegeben eine Doktorarbeit an mein Studium anzuhängen. Du hast mir wissenschaftliche Verantwortung übertragen an der ich wachsen konnte und mich dabei unterstützt vielfältige Erfahrungen in der Wissenschaft zu sammeln. Mit dir im Hintergrund konnte ich meine wissenschaftliche Arbeit und meine Familie vereinbaren. Natürlich gilt der Dank auch meiner gesamten Arbeitsgruppe. Durch die gute Zusammenarbeit und Hilfsbereitschaft war die Zeit der Promotion mehr als nur Arbeit. Danke an Richard, Lothar und Uwe, dass ihr stets für Fragen zu experimentellen Problemen zur Verfügung standet und auch an Alex für die Zusammenarbeit am zweiten Chlorosom-Paper.

Nicht zu vergessen ist natürlich auch die Technik. Werner und Stefan, ihr ward immer da wenn es brennt. Danke für eure Unterstützung. Ebenso gilt mein Dank Peter für die IT-Unterstützung, dem Mechanikwerkstatt-Team um Frank und natürlich der Helium-Mannschaft Harald und Michael. Danke für die gute Zusammenarbeit bei tiefen Temperaturen.

Evelyn, Micha und Franzi ohne eure Organisation läuft nichts am Lehrstuhl und euer Anteil am Erfolg der wissenschaftlichen Arbeit ist viel größer als ihr denkt.

Durch den Zusammenhalt am Lehrstuhl wurden aus vielen Kollegen Freunde. Ich möchte allen danken, dass ich diese tolle Erfahrung machen konnte und hoffe, dass die Kontakte noch lange bestehen bleiben.

Special thanks to Jasper Knoester’s group in Groningen. Jasper, Erik, Thomas and Tenzin, thank you for your input on the chlorosome projects, the fruitful collaboration and the amazing time I had in Groningen.

Wunderbare Freundschaften haben mich begleitet und meine Zeit in Bayreuth, das Studium und die Promotion haben mich weitere schließen lassen, die sich jetzt in die verschiedensten Winkel der Welt erstrecken. Danke für die schöne Zeit und danke für

eure Freundschaft in der Nähe oder Ferne. Oder frei nach Friedrich W. Nietzsche: Vielleicht sitzen wir alle irgendwann einmal in Bayreuth zusammen und begreifen gar nicht mehr, wie man es anderswo aushalten konnte.

Das Beste kommt natürlich am Schluss: meine Familie. Es lässt sich schwer in Worte fassen, welchen Wert ihr in meinem Leben habt.

Danke Mama, Julian und Oma für all eure Unterstützung in meinem Leben und eure Liebe.

Danke allen Günthers, dass ich auch Teil eurer Familie sein darf und ihr immer hinter mir steht.

Robert und Anton, ihr seid einfach wunderbar. Danke, dass ihr euer Leben mit mir teilt.

“ *Nobody important? Blimey, that’s amazing. Do you know, in nine hundred years of time and space I’ve never met anyone who wasn’t important before.* ”

THE DOCTOR

Eidesstattliche Versicherung

Hiermit versichere ich an Eides statt, dass ich die vorliegende Arbeit selbstständig verfasst und keine anderen als die von mir angegebenen Quellen und Hilfsmittel verwendet habe.

Weiterhin erkläre ich, dass ich die Hilfe von gewerblichen Promotionsberatern bzw. -vermittlern oder ähnlichen Dienstleistern weder bisher in Anspruch genommen habe, noch künftig in Anspruch nehmen werde.

Zusätzlich erkläre ich hiermit, dass ich keinerlei frühere Promotionsversuche unternommen habe.

Bayreuth, den 25. März 2020